ADVANCED MATERIALS
www.advmat.de

High-Energy-Density Aqueous Zinc-Ion Batteries: Recent Progress, Design Strategies, Challenges, and Perspectives

Mingcong Tang, Qun Liu, Xiaohong Zou, Biao Zhang, and Liang An**

Aqueous zinc-ion batteries (AZIBs) are emerging as a promising energy storage technique supplementary to Li-ion batteries, attracting much research attention owing to their intrinsic safety, cost economy, and environmental friendliness. However, energy densities for AZIBs still do not fulfill practical requirements because of the low specific and areal capacity, limited working potential, and excessive negative-to-positive electrode capacity (N/P) ratio. In this review, a comprehensive overview of basic requirements and major challenges for achieving high-energy-density AZIBs is provided. Following that, recent progress in the optimization of each component and the overall configuration is summarized, and crucial design principles are discussed. Apart from conventional emphasis on each part, especially cathode materials, separately, the comprehensive discussion about the synergistic interactions among all components is conducted. Finally, the outlook and research direction are given to provide valuable guidance for the further holistic development of high-energy-density aqueous zinc-ion batteries.

1. Introduction

Renewable energy conversion and storage technologies have garnered significant attention to address escalating environmental concerns. Among these techniques, aqueous zinc-ion batteries (AZIBs) stand out due to their environmental friendliness, inherent safety, high theoretical capacity (820 mAh g^{-1}) of zinc, suitable redox potential (−0.763 V vs standard hydrogen electrode (SHE)), and abundant zinc reserves.[1] However, the practical application of AZIBs is hindered by challenges, such as anode instability, cathode dissolution, and low energy density. Theoretically, the energy density for a selected anode and cathode pair should be fixed by calculating it from the Nernst equation after obtaining the Gibbs formation energy and density of reactants and products.[2] However, considering energy loss during the practical operation, this value is commonly overestimated, with an optimal ratio between practical and theoretical energy density of 42%–58% for conventional Li-ion batteries.[3] Instead, practical energy densities are more reference-worthy. Fundamentally, the practical energy density represents the energy released from per unit of active materials during the discharge process, and it can be calculated by multiplying the capacity and the voltage of operation for a settled full cell.[4] For active materials-based evaluation, the gravimetric and volumetric energy density are expressed with the unit of Wh kg^{-1} and Wh L^{-1}, respectively, and mass/volume applied here are formula mole weight/volume of involved reactants.[3] Even though this routine functions well for laboratory evaluation of batteries, calculation based on mass/volume of all components in a cell is more ideal for a commercialized system. According to the formula for energy density evaluation, compared to organic rechargeable batteries, aqueous systems demand more stringent requirement on energy density improvement because they typically deliver limited voltage outputs, primarily attributed to the narrow electrochemical stability window (ESW) (**Figure 1a**), which further constrains discharge capacity and operating voltage of various cathodes (Figure 1b).[5] Additionally, with limited surface area, poor reversibility, and substantial weight, the conventional zinc foil anode further restricts energy output (Figure 1c).[6] These factors collectively contribute to the persistent issue of low energy density in AZIBs. Despite these challenges, aqueous systems offer the potential for higher yields once high energy density is achieved because, unlike

M. Tang, X. Zou, L. An
Department of Mechanical Engineering
The Hong Kong Polytechnic University
Hung Hom, Hong Kong SAR 999077, China
E-mail: liang.an@polyu.edu.hk
Q. Liu, B. Zhang
Department of Applied Physics
The Hong Kong Polytechnic University
Hung Hom, Hong Kong SAR 999077, China
E-mail: biao.ap.zhang@polyu.edu.hk
Q. Liu
College of Energy Materials and Chemistry
College of Chemistry and Chemical Engineering
Inner Mongolia University
Hohhot 010021, China
L. An
Research Institute for Advanced Manufacturing
The Hong Kong Polytechnic University, Hung Hong
Kowloon, Hong Kong SAR 999077, China
L. An
Research Centre for Carbon-Strategic Catalysis
The Hong Kong Polytechnic University, Hung Hom
Kowloon, Hong Kong SAR 999077, China

The ORCID identification number(s) for the author(s) of this article can be found under https://doi.org/10.1002/adma.202501361

DOI: 10.1002/adma.202501361

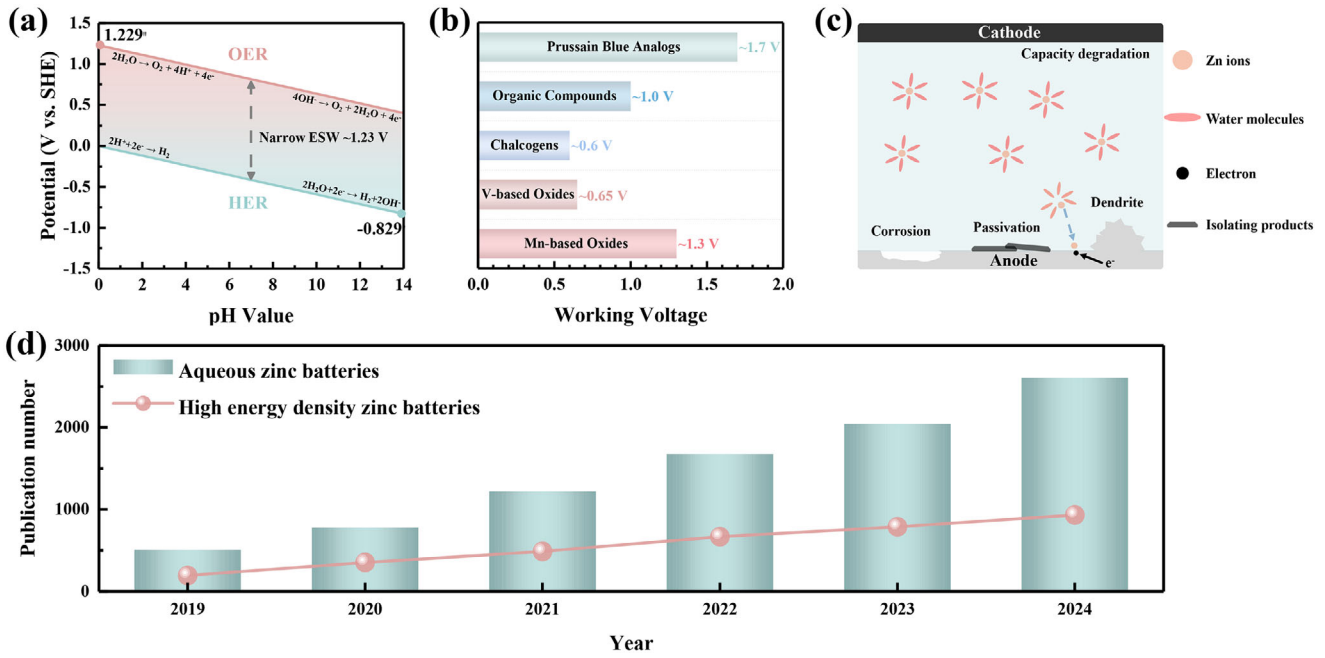

Figure 1. a) The redox potentials of oxygen evolution reactions and hydrogen evolution reactions in different pH environments. b) Working voltages of typical cathodes. c) Illustration of anode issues in aqueous zinc-ion batteries. d) The number of publications on AZIBs and high-energy-density ones.

organic rechargeable batteries, where increased energy density often correlates with heightened safety risks, AZIBs maintain their safety profile.[7]

Therefore, enhancing the energy density of AZIBs has become a critical focus in battery research, aiming to deliver a safe, commercially viable, and efficient energy storage solution (Figure 1d). Current research efforts to elevate energy densities can be categorized into two main strategies: increasing energy output and trimming the excessive mass or volume of the system. The former strategy involves the development of novel cathode materials with higher capacity or working potential, optimizing cathode reaction mechanisms, and modifying electrolytes to support high-voltage redox reactions.[8] The latter strategy focuses on minimizing system weight or volume by using anode-free or zinc-lean electrodes and lightweight functional separators.[1a,9]

While extensive research has been conducted to develop high-energy-density AZIBs, emphasis is still exerted on cathodes and anodes separately. A comprehensive summary that systematically addresses the individual components of a battery and their interactions has yet to be presented. This review starts from the introduction of high-voltage and high-capacity cathode materials, which directly influence the upper limit of energy densities. Following that, optimized electrolytes fulfilling increasing voltage demands of those advanced cathodes are summarized. Consequently, besides techniques elevating theoretical energy output, routines, which are beneficial for mass/volume reduction, focusing on the anode and separator are illustrated. After analyzing proposed strategies and remaining challenges in both independent and synergistic manner, a perspective for future high-energy-density AZIB design is offered (**Scheme 1**).

2. High-Energy-Density AZIBs via Optimized Cathodes

The energy density is determined by the specific capacity and operating voltage. Theoretically, the capacity of the battery is limited by the lower value between the cathode capacity and the anode capacity. Because of the high capacity of zinc and excessive anode active materials, the capacity of the cathode is the decisive factor. Meanwhile, the voltage is determined by the electrode potential difference between opposite cathodes. Once the electrolyte and the zinc anode are selected, the anodic reaction is restricted to zinc plating/stripping, so the anode potential is unchanging. Thus, the determinant factor for the battery voltage is also the cathode potential. As a result, to elevate specific capacities and increase the operating voltage to maximize energy output, the optimization of cathodes targeting either enhanced capacity and/or voltage becomes the top priority.

2.1. High-Capacity Cathode

Typical cathode materials for AZIBs include manganese-based oxides, vanadium-based oxides, Prussian blue analogs (PBAs), polymer compounds, etc. Among these, manganese-based oxides and vanadium-based oxides have been most comprehensively adopted for investigation. A series of manganese-based oxides including MnO_2, Mn_2O_3, Mn_3O_4, and MnO have been reported as effective cathode materials, and MnO_2 is the most extensively used. After continuous exploration of their energy storage mechanisms, currently, four mainstream ones are proposed in the chronological order: Zn^{2+} (de)intercalation ($Zn^{2+} + 2e^- + 2MnO_2 \leftrightarrow ZnMn_2O_4$), conversion reaction, Zn^{2+}/H^+ co-(de)intercalation ($MnO_2 + H^+ +$

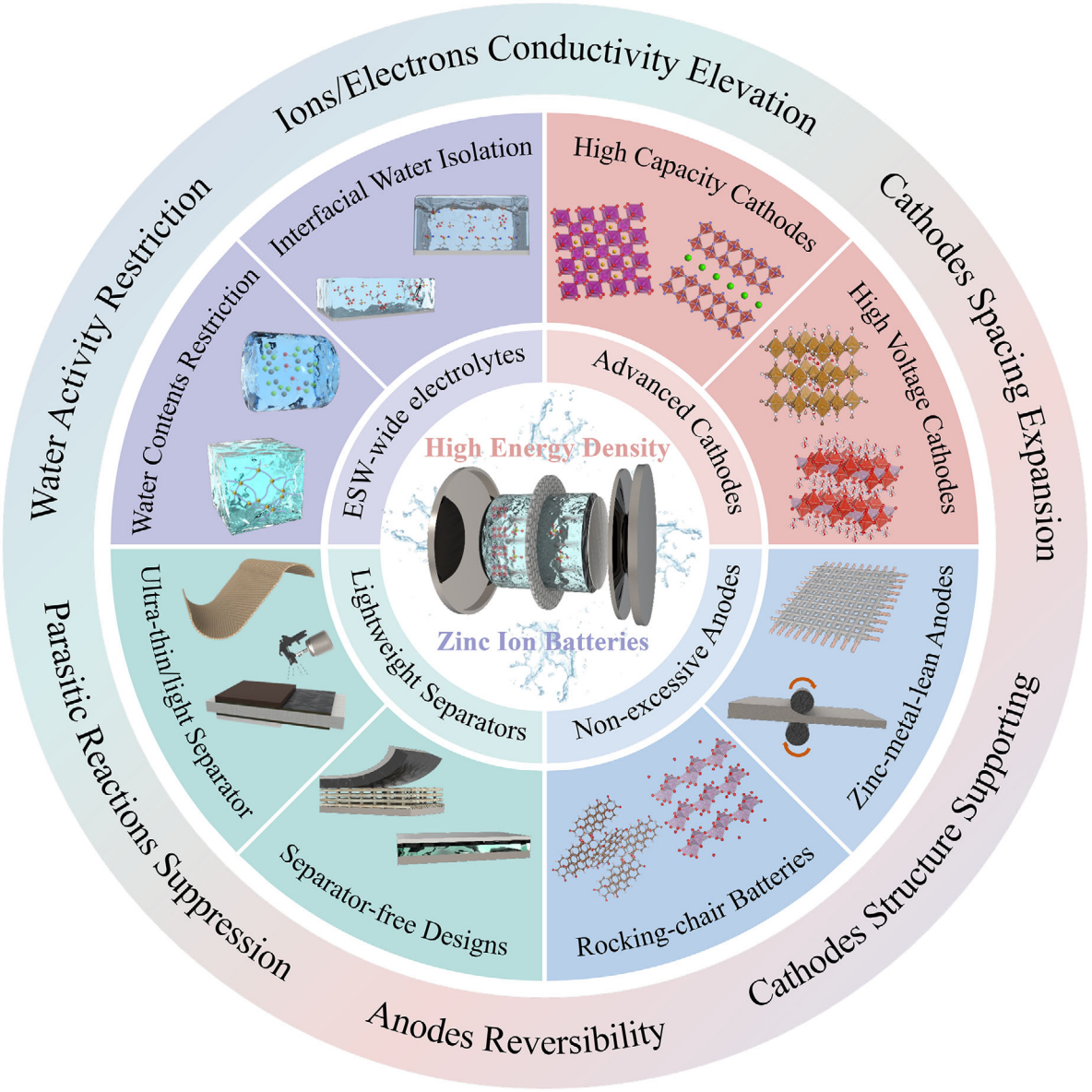

Scheme 1. Summary of design concepts, specific strategies, and desired properties for reaching the high-energy-density AZIBs.

$e^- \leftrightarrow MnOOH$, and $Zn^{2+} + 2MnO_2 + 2e^- \leftrightarrow ZnMn_2O_4$), and dissolution/deposition mechanism.[10] Based on one or two-electron transfer reactions, the theoretical capacities for MnO_2 can reach 308, and 617 mAh g^{-1}, respectively.[11] For vanadium-based oxides, V_2O_5 is adopted the most with the Zn^{2+} (de)intercalation ($Zn^{2+} + 2e^- + V_2O_5 \leftrightarrow ZnV_2O_5$) as the primary mechanism.[12] Moreover, others like Zn^{2+}/H^+ co-(de)intercalation, Zn^{2+}/H_2O co-(de)intercalation and chemical conversion reaction have also been discovered for modified vanadium-based oxides, and a theoretical capacity of 589 mAh g^{-1} can be achieved for a two-electron pathway.[13] Meanwhile, researches related to other cathodes like PBAs (primarily based on Zn^{2+} insertion), organic compounds (primarily based on the coordination), and conversion-types (e.g., chalcogens, halogens) are also flourishing for their different advantages like high voltage, ideal theoretical capacity, or favorable stability.

Unfortunately, despite their outstanding potentials, practical capacities reported in the literature are significantly lower compared to theoretical ones for all of these cathodes. Therefore, substantial efforts have been directed toward developing cathode materials with extensive theoretical capacities or enhancing the practical capacities of existing cathodes to improve energy densities (**Table 1**).

2.1.1. Cathodes with a High Theoretical Capacity

The discharge capacity depends on the number of transferred electrons in active materials, directly defined by the valence states

Table 1. Performance of high-capacity cathodes.

Cathode material	Electrolyte	Working voltage [V][a)]	Capacity [mAh g^{-1}]	Energy density [Wh kg^{-1}]	Mechanism	Refs.
$Mo_{0.03}Mn_{0.97}O_2$	2 M $ZnSO_4$+0.1 M $MnSO_4$	1.5	652	–	MnO_2/Mn^{2+} conversion and H^+/Zn^{2+} cointercalation	[15]
Cu-doped ϵ-MnO_2	3 M $ZnSO_4$+0.2 M $MnSO_4$	≈1.32	397.4	563.5	H^+/Zn^{2+} cointercalation	[14a]
Na-Cu codoped δ-MnO_2	2 M $ZnSO_4$+0.2 M $MnSO_4$	≈1.2	364	–	MnO_2/Mn^{2+} conversion and H^+/Zn^{2+} cointercalation	[16]
O_d-MnO_2	1 M $ZnSO_4$+0.2 M $MnSO_4$	1.36	470	470	Zn^{2+}intercalation	[26]
$Ca_2Mn_3O_8$	3 M $Zn(CF_3SO_3)_2$+0.3 M $Mn(CF_3SO_3)_2$	1.39	368	512	Zn^{2+}intercalation	[27]
$K_{0.41}MnO_2{\cdot}0.5H_2O$	2 M $ZnSO_4$+0.2 M $MnSO_4$	1.34	382	512	H^+/Zn^{2+} cointercalation	[28]
La-Ca codoped ϵ-MnO_2	1 M $ZnSO_4$+0.4 M $MnSO_4$	1.35	297	401	H^+/Zn^{2+} cointercalation	[29]
Co-Mn_3O_4/CNA	2 M $ZnSO_4$+0.2 M $MnSO_4$	1.28	362	463	H^+/Zn^{2+} cointercalation	[30]
CrNi-MnO_2	2 M $ZnSO_4$+0.1 M $MnSO_4$	≈1.33	590	–	MnO_2/Mn^{2+} conversion and H^+/Zn^{2+} cointercalation	[14b]
α-MnO_2/graphene scrolls	2 M $ZnSO_4$+0.2 M $MnSO_4$	1.3	382.2	406.6	H^+/Zn^{2+} cointercalation	[31]
V_2O_3	2 M $Zn(CF_3SO_3)_2$	0.65	625	406	Zn^{2+} intercalation	[17]
VO_2	2 M $Zn(CF_3SO_3)_2$	0.7	610	426	Zn^{2+} intercalation	[18]
a-V_2O_5@C	3 M $Zn(CF_3SO_3)_2$	0.77	620	475	Zn^{2+} intercalation	[32]
$Cu_{0.1}V_2O_5{\cdot}0.08H_2O$	2 M $ZnSO_4$	0.6	410	298	Zn^{2+} intercalation	[33]
$K_{0.5}V_2O_5$	3 M $Zn(CF_3SO_3)_2$	0.6	317	≈187	Zn^{2+}/H_2O intercalation	[34]
CaVOH/rGO	3 M $Zn(CF_3SO_3)_2$	≈0.65	299	381	Zn^{2+} intercalation	[35]
PANi-VOH	3 M $Zn(CF_3SO_3)_2$+6 M $LiC_2F_6NO_4S_2$	≈0.7	323	216	Zn^{2+} intercalation	[36]
PEDOT-$NH_4V_3O_8$	3 M $Zn(CF_3SO_3)_2$	≈0.6	356.8	353.1	Zn^{2+} intercalation	[37]
V_6O_{13}/CC	3 M $ZnSO_4$	0.98	520	511	Zn^{2+} intercalation	[38]
$V_2O_5{\cdot}4\,VO_2{\cdot}2.72\,H_2O$	3 M $Zn(CF_3SO_3)_2$	0.66	567	375	Zn^{2+} intercalation	[39]
HATN	2 M $ZnSO_4$	0.4	405	≈162	H^+/Zn^{2+} co-ordination	[19]
G-Aza-CMP	2 M $ZnSO_4$	≈0.6	456	≈270	H^+/Zn^{2+} co-ordination	[20]
TAPQ	2 M $ZnSO_4$	0.84	270	227	H^+/Zn^{2+} cointercalation	[21]
CTF-TTPQ	2 M $ZnSO_4$	1.07	404	432.28	H^+/Zn^{2+} cointercalation	[22]
HATNQ	3 M $ZnSO_4$	≈0.6	482.5	289	H^+/Zn^{2+} co-ordination	[23]
PONEA	3 M $Zn(CF_3SO_3)_2$	≈0.7	329	242	Zn^{2+} co-ordination	[24]
BT-PTO COF	3 M $Zn(CF_3SO_3)_2$	0.4	225	92	H^+/Zn^{2+} cointercalation	[25]
PANI-GO/CNT	2.5 M $Zn(CF_3SO_3)_2$	≈1.1	233	–	H^+/Zn^{2+} coordination	[40]

[a)] The working voltage is from values reported in publications. If they did not report, the medium of the discharge plateau is chosen as the working voltage.

of oxides above. Thus, dilated valence changes are beneficial for elevating the theoretical capacity. One strategy is incorporating other metals to evoke extra valence electron transport, which is common in manganese-based oxides. One electron reaction between Mn^{4+}/Mn^{3+} dominates conversion for the MnO_2 cathode, unveiling a low theoretical capacity of 308 mAh g^{-1}. Thus, activation of another electron transmission is critical to release the full potential of Mn species. Currently, Mo-, Cu-, NaCu-, and CrNi-doped MnO_2 have been prepared with capacities approaching 400 mAh g^{-1} by arousing the two-electron redox. Amid these, Cu and Cr provide one additional electron redox couple (Cu^{2+}/Cu^+, Cr^{3+}/Cr^{2+}), stimulating the further reduction from Mn^{4+} to Mn^{2+}.[14] Others, like Mo, also facilitate the Mn^{4+}/Mn^{2+} shift by utilizing its higher binding energy with oxygen to promote the Jahn–Teller distortion of octahedral [MnO_6].[15] Furthermore, the cointercalation of different ions can bring the superposition of advantages. For example, Gao et al. fabricated the Na-Cu cointercalated MnO_2, as shown in **Figure 2a**, through a simple precipitation method. During the cycling process, the reduction/oxidation of Cu activates the Mn^{4+}/Mn^{2+} redox pair by facilitating the charge transfer, and the introduction of Na amplifies this effect (Figure 2b). Consequently, the NaCu-MnO_2 exhibits an encouraging capacity of 200 mAh g^{-1} even at the high current density of 2 A g^{-1}, overwhelming its single Na-intercalated counterpart (Figure 2c). The capacity, shown in Figure 2d, can be further elevated to 364 mAh g^{-1} when the current density decreases, demonstrating effective capacity improvement among the whole current range compared to Na-intercalated MnO_2 (Figure 2e).[16]

Besides ex situ doping, the in situ oxidation, which introduces high valence oxides, is more common for vanadium-based oxides due to the rich valence states of V. By generating V_2O_{5-x} as

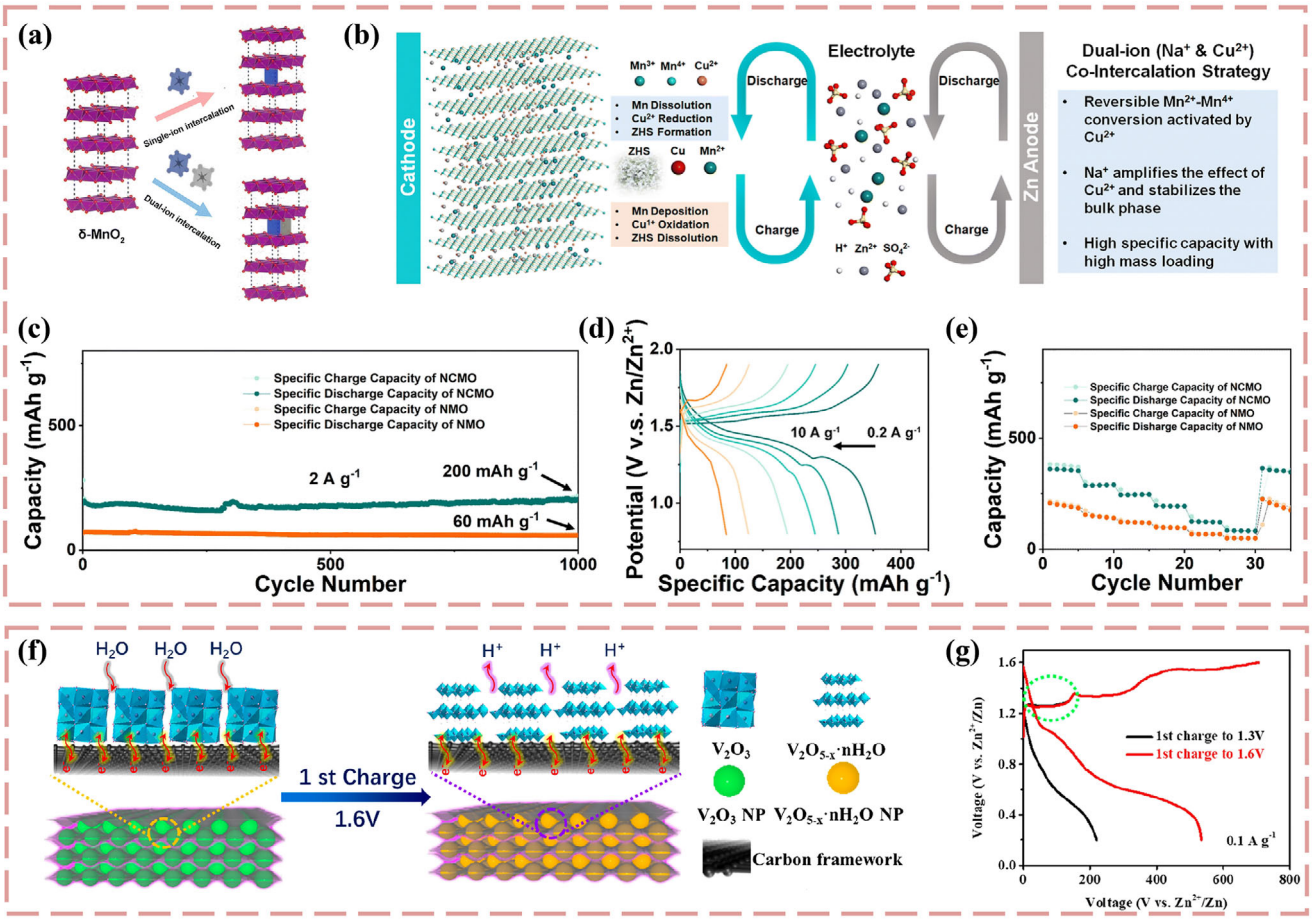

Figure 2. V-, and Mn-based cathodes with a high theoretical capacity. a) Schematic demonstration of single ion and double ions intercalation strategy for δ-MnO_2. b) Schemes of discharge and charge process of Zn||NCMO batteries. c) The cycling performance of Zn||NCMO and Zn||NMO batteries at 2 A g^{-1}. d) Voltage profiles and e) cycling performance for Zn||NCMO batteries at different current densities. a–e) Reproduced under the terms of the CC-BY Creative Commons Attribution 3.0 Unported License.[16] Copyright 2024, X. Gao et al., published by Royal Society of Chemistry. f) The oxidation process of V_2O_3 during the first charging step. g) Galvanostatic charge and discharge curves for Zn||V_2O_3 batteries at 0.1 A g^{-1}. f–g) Reproduced with permission.[17] Copyright 2020, American Chemical Society.

the cathode precursor for the primary cycle, the following excitative oxidation is equipped to release more capacity. As shown in Figure 2f, Luo et al. fabricated the V_2O_3 cathode. The in situ oxidation happens by charging to 1.6 V, turning the V_2O_3 into V_2O_{5-x}, followed by a bi-layer $V_2O_5{\cdot}nH_2O$. This in situ prepared V_2O_5 presents an enlarged layer space, contributing to a discharge capacity of 536 mAh g^{-1} for the first cycle (Figure 2g), and a superior energy density of 406 Wh kg^{-1} is also realized at 0.1 A g^{-1}.[17] A similar procedure can also be observed in VO_2 to deliver a higher energy density of 426 Wh kg^{-1}.[18]

Boosting theoretical capacities is more effortless for organic compounds than for oxide counterparts. Attributed to flourishing anchor points on their full-bottomed carbon chain, the grafting active coordination groups are beneficial for embracing elevated capacities. Clustered by redox-active groups, organic cathodes include n-type, p-type, and bipolar-type. Amidst them, n-type compounds exhibit the highest discharge capacity, followed by bipolar-type analogs. Currently, comprehensive n-type cathodes have been accounted for, delivering exceptional capacities. These organic compounds contain multiple in-plane hydrogen bonds through their rich C=O and C=N groups, presenting active out-of-plane π–π interactions. As a result, encouraging theoretical capacities are confirmed by exhibiting elevating actual capacities. For example, Tie et al. revealed the fast H^+ uptake/removal kinetics in diquinoxalino [2,3-a:2′,3′-c] phenazine (HATN). The calculation further confirms that up to six H^+ are coordinated to corresponding six N positions on HATN (**Figure 3a**), and the abundant transferred charges help reach a discharge capacity of 405 mAh g^{-1}.[19] Others like graphene/aza-fused π-conjugated microporous polymer composite (G-Aza-CMP),[20] 5,7,12,14-tetraaza-6,13-pentacenequinone (TAPQ) (Figure 3b),[21] quinoxalinophenazinedione covalent triazine framework (CTF-TTPQ),[22] and hexaazatrinaphthalene-quione (HATNQ)[23] also possess capabilities of chelating multiple Zn^{2+} and H^+ on their N- and O- positions, and practical capacities higher than 400 mAh g^{-1} are reached for these cathodes. Inferior to the n-type organic cathode, a lower capacity ranging from about 170 to 330 mAh g^{-1} is more ordinary for the bipolar cluster. One distinguished representative is the polyquinone-phenylenediamine (PONEA) cathode. By integrating

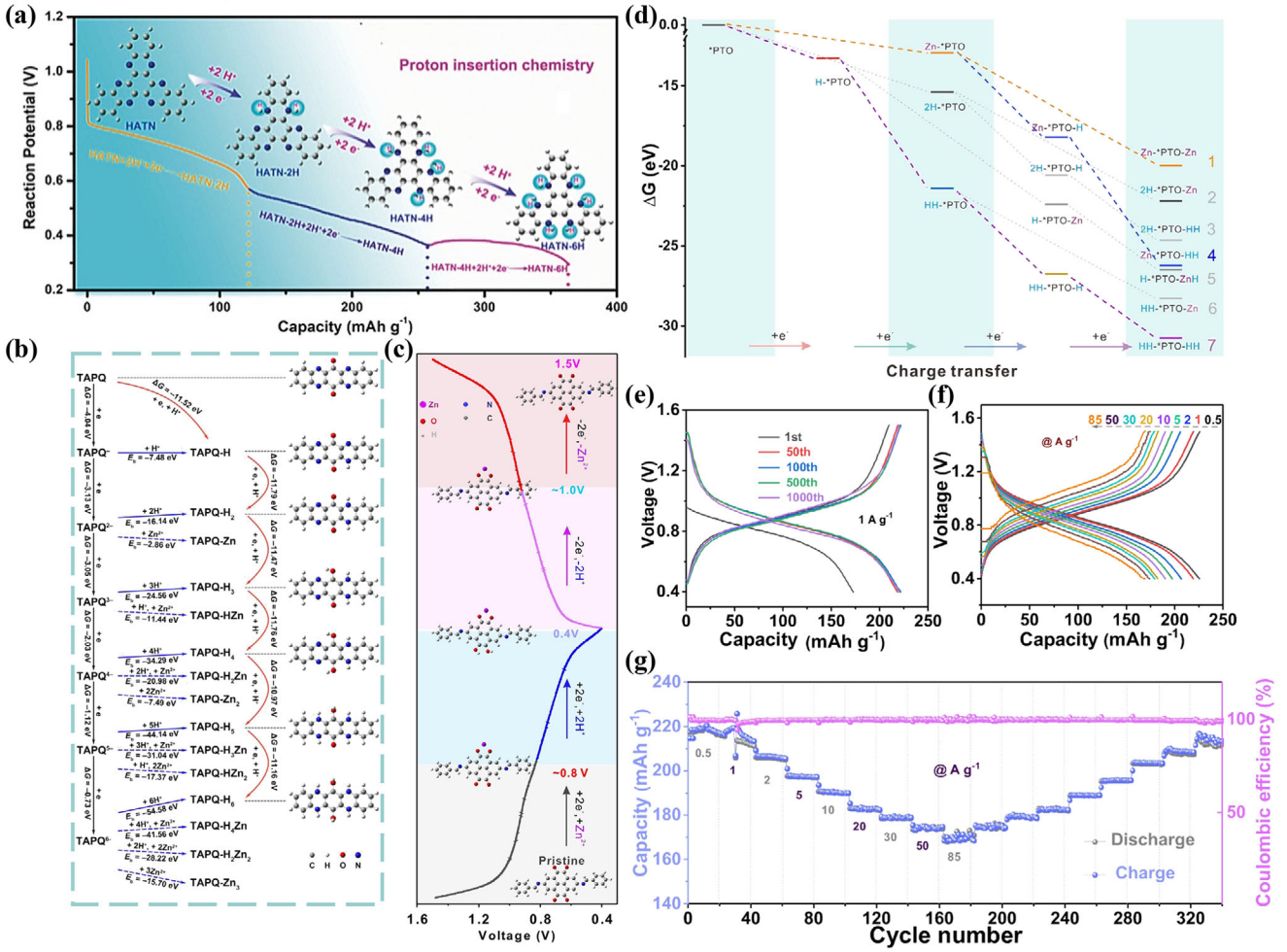

Figure 3. Organic compounds cathodes with a high theoretical capacity. a) Calculated protonation process of HATN at discharging. a) Reproduced with permission.[19] Copyright 2020, Wiley-VCH. b) The calculated binding energy (E_b) between TAPQ, H^+, and Zn^{2+}, inserted values showing the Gibbs free energy gaps. b) Reproduced with permission.[21] Copyright 2021, Elsevier. c) The H^+, Zn^{2+} coinsertion process of BT-PTO COF, and d) calculated Gibbs free energy gaps. e) Galvanostatic charge and discharge curves for Zn||BT-PTO COF battery at 1 A g^{-1}, and f) at different current densities. g) The rate performance of the Zn||BT-PTO COF battery. c–g) Reproduced with permission.[25] Copyright 2022, Wiley-VCH.

benzoquinone and p-phenylenediamine moieties, PONEA gains both C═O and —NH— groups, facilitating the transaction and coordination of Zn^{2+}. Combining the boosted electronic conductivity with reduced graphene oxide, the capacity of 319 mAh g^{-1}, equivalent to the energy density of 242 Wh kg^{-1}, is delivered.[24] Finally, the advancement of capacities of p-type compounds is the most limited. At present, the most celebrated achievement is discovered in the orthoquinone-based covalent organic framework (BT-PTO COF). This COF obtains a unique channel structure beneficial for ion transfer, and a redox pseudocapacitance mechanism is discovered. As shown in Figure 3c, an unprecedented ordered Zn^{2+}-2 H^+ coinsertion procedure is found during the cycling. The feasibility of coinsertion is also confirmed by its moderate Gibbs free energy gaps (ΔG), compared to the most difficult 4 H^+ path and the most comfortable 2 Zn^{2+} path (Figure 3d). Consequently, the Zn||BT-PTO COF battery reaches 221 mAh g^{-1} at 1 A g^{-1} with the 3.0 M $Zn(OTf)_2$ electrolyte (Figure 3e). More encouragingly, an excellent rate performance is demonstrated by minimal capacity gaps at varying current densities shown in Figure 3f,g, and finally, the capacity 225 mAh g^{-1}, matching the energy density of 92.4 Wh kg^{-1}, is exhibited at 0.1 A g^{-1}.[25]

The capacity benchmark for intercalation-type and coordination-type cathodes has been refreshed continuously, but a significant gap exists between them and conversion-type analogs. Currently, among conversion-type cathodes, the chalcogens (S, Se, Te) and the halogens (I_2, Br_2, etc.) stand out. The chalcogens are attractive for their superior capacities, and the halogens show potentials with their multiple favorable discharge platforms. Within the high-capacity chalcogens, the S cathode attracts the most due to its unparalleled theoretical specific capacity (1675 mAh g^{-1}) and the miniature particle size expediting the charge transport. However, the potential of the chalcogens cathode is concealed because of multiple challenges. First, the electronic conductivity is poor, especially for S (5×10^{-28} S m^{-1}), and inhomogeneous bi-products will be generated during the discharge. Both will cause the remarkable polarization. Second, the kinetics is sluggish because the conversion is between all

Table 2. Performance of the chalcogen cathodes.

Cathode material	Electrolyte	Working voltage [V][a)]	Capacity [mAh g^{-1}]	Energy density [Wh kg^{-1}]	Mechanism	Refs.
S@CMK-3	3 M $Zn(CF_3SO_3)_2$	0.24	788	–	S/ZnS conversion	[41]
S@CNTs-50	1 M $Zn(CH_3COO)_2$+0.05 wt% I_2	0.5	1105	502	S/ZnS conversion	[42]
S@NPC	2 M $Zn(CF_3SO_3)_2$+50 mM ZnI_2 (H_2O and EG cosolvent)	0.5	1435	730	S/ZnS conversion	[43]
LF-PLSD	1 M $Zn(C_2F_6NO_4S_2)_2$	–	1146	724.7	S_6/ZnS conversion	[44]
LF-PLSD	1 M $Zn(C_2F_6NO_4S_2)_2$+21 M $LiC_2F_6NO_4S_2$)	–	–	331	S_6/ZnS conversion	[44]
S@Fe-PANi	2 M $ZnSO_4$	0.58	1205	720	S/ZnS conversion and Zn^{2+} intercalation	[45]
ZnS@CF	3 M $ZnSO_4$+1 wt% TUI	≈0.6	1410	832	S/ZnS conversion	[46]
S@3D honeycomb-like carbon	0.5 M $ZnSO_4/CuSO_4$ Gelatin decoupling hydrogel	≈1.2	2063	2372	S/ZnS and S/Cu_2S conversion	[47]
Te nanosheet	1 M $ZnSO_4$ PAM hydrogel	0.61	386	74.1	Te/ZnTe conversion	[48]
Te nanorods-rGO	2 M $ZnSO_4$	0.6	621	394.4	Te/ZnTe conversion	[49]
TeO_2/C	2 M $ZnSO_4$	0.61	800	488	TeO_2/ZnTe conversion	[50]
Se@CMK-3	1 M $Zn(C_2F_6NO_4S_2)_2$	≈1.25	611	751	Se/ZnSe conversion	[51]

[a)] The working voltage is from values reported in publications. If they did not report, the medium of the discharge plateau is chosen as the working voltage.

solid forms.[52] Third, during the conversion process, the volume variation is notable, so the structure is easily destroyed.[53] Last but not least, the "shuttle effect" will cause the further loss of active materials. Specifically, the long-chain polysulfides form during the discharge and are dissolved in electrolytes. Once they migrated to the anode, they will react with the anode. This continuous process will cause severe active materials loss.

The former two drawbacks primarily lock their potentials of high capacities, and the latter two influence more on the cycling reversibility and stability. As for now, introducing activated carbon as the conductive support is becoming a standard strategy for improving the conductivity and boosting the kinetics, and as a result, the energy density can be elevated up to 547 Wh kg^{-1}.[54] At the same time, the strategy for stabilizing the structure has also been proposed. For example, the energy density can be further improved in the polysulfide cathode due to its more stable structure and multielectron reaction path as S_6 to S^{2-}. As reported, the energy density of 724.7 Wh kg^{-1} can be obtained with the poly(Li_2S_6-random-(1,3-di isopropenyl benzene)) (poly(Li_2S_6-r-DIB) copolymer (PLSD) cathode.[44] Inspired by the S cathode, the potentials of others (Se and Te) were also investigated (**Table 2**). Compared to S, Se exhibits a superior conductivity (1×10^{-3} S m^{-1}). Combining its safety, cost-effectiveness, and high theoretical specific capacity (675 mAh g^{-1}), Se is becoming increasingly attractive. However, intractable shortages like sluggish reactions due to the large size and accompanying shape variation during conversion still need to be solved. Therefore, although astonishing performance has been reported by supplementing carbon support, the step to large-scale commercial production of Zn-Se batteries is still blocked. The Te cathode, with even higher conductivity (2×10^2 S m^{-1}), was first reported to be coupled with the zinc anode by Chen et al. to reach the discharge capacity of 1155 mAh cm^{-3}.[48] Because Te shares properties similar to S and Se, the carbon modification strategies mentioned above have also been confirmed to optimize the Te cathode. Furthermore, a two-step solid–solid reaction that converts TeO_2 into ZnTe has also been proposed. This six-electron mechanism can maximize the capacity. For example, Yan et al. described the TeO_2/C cathode. The consecutive transmutation from TeO_2 to Te and then to ZnTe raised six electron transfers and reached an ultrahigh capacity of 800 mAh g^{-1}.[50]

Besides the electrode engineering, the electrolyte modification has also shown eye-catching effectiveness. Up to now, highly concentrated electrolytes, functional additives, cosolvent electrolytes and hydrogel electrolytes have all shown their promotion on both capacities and the cycling stability. For example, Li et al. used the concentrated 3 M $Zn(OTf)_2$ electrolyte to obtain a capacity retention up to 90% of the initial value (500 mAh g^{-1}) after 200 cycles.[41] Additives including I_2,[42] thiourea,[55] quaternary ammonium iodide,[56] etc., have been proposed, and they commonly function as a redox mediator to facilitate the kinetics, minimizing the energy loss. Besides, cosolvents like acetonitrile,[57] tetraglyme,[58] ethylene glycol (EG),[43] polyethylene glycol-400 (PEG-400),[59] etc., usually show the powerful potency on suppressing side reactions and the shuttle effect by restricting water. Similarly, the shuttle effect is also relieved with hydrogel electrolytes. Their quasisolid–solid interface successfully avoids the dissolution of polysulfides, endowing the zinc-chalcogens batteries with the overwhelming reversibility. Currently, multiple poly(vinyl alcohol)-based (PVA-based) and polyacrylamide-based (PAM-based) hydrogels have been employed.[44,45,60] With their advantageous capacity retentions, the chalcogen cathodes are taken one step forward to the practical application.

2.1.2. Cathodes with the Optimized Actual Capacity

Even though many researchers have dedicated themselves to amplifying theoretical capacities by designing plural-electron active cathode materials, practical capacities released through actual laboratory tests are much lower than theoretical values. The unfavorable capacity can be ascribed to poor selectivity to Zn^{2+}, distasteful conductivity, and passivated active areas. All of these disadvantages can be summarized as the insufficient contact between active ions and electrons. Therefore, strategies including electronic conductivity optimization through introducing extra conductive agents, modifying crystal structures with zincophilic properties, designing different morphologies for maximized surface areas, and synthesizing heterojunction cathodes with synergistic effect have been investigated.[61]

The optimization of the electronic behavior should involve high-conductivity materials, with carbon materials as the top priority. Carbons always show low density with an astonishing specific surface area, so contact areas between charge carriers and active cathode materials can be magnified. Combining these merits, carbon-supported cathodes always release actual capacities closer to theoretical values. Depending on the modality of the combination between active and carbon materials, carbon was categorized into conductive substrates and conductive matrixes. To employ carbon materials as conductive substrates, active materials will be uniformly distributed on carbon surfaces. The mixture of different 3D or 1D/2D/3D carbon materials is commonly chosen to ensure both immense surface areas and the auspicious stability of the structures. The amalgamation of 2D graphene and multiple 3D carbon or active materials, including nanotubes, nanowires, and nanorods, is trendy. To illustrate, the fabricated polyaniline-graphene/carbon nanotubes (PANi-GO/CNT),[40] V_2O_5/graphene,[62] and MnO_2 nanorods-graphene[63] cathodes can deliver capacities of 233, 391, and 301 mAh g^{-1}, respectively. In addition, capacity amelioration can also be achieved by utilizing carbon supports with a more expanding surface. For example, Khamsanga et al. anchored the MnO_2 nanoflowers on the graphite flakes to reach the specific capacity of 235 mAh g^{-1}.[64] The modification through carbon supports is also applied to chalcogen anodes to elevate the actual capacity further. The optimization of the S cathode with carbon has been comprehensively investigated. The pioneering work exhibits an energy density of 502 Wh kg^{-1} by anchoring 50 wt% S on carbon nanotubes.[42] Then, the following works recorded astonishingly high capacities of about 700, 1083.3, and even 2372 Wh kg^{-1} by employing nanoporous carbon,[43] Ketjen-black,[65] and honeycomb-like carbon[47] as the support. Besides S, the Se cathode has a capacity of 503 mAh g_{Se}^{-1} by employing the CMK-3 porous carbon support.[66] Similarly, the Te cathode exhibits a capacity of 476 mAh g^{-1} (corresponding to the energy density of 394.4 Wh kg^{-1}) by attaching the reduced graphene oxide (rGO) (**Figure 4a,b**). Moreover, attributed to the strong binding between the chalcogen and C, the structure cyclability is also advanced, and the shuttle effect is eliminated in these carbon-assisted chalcogen cathodes, ensuring favorable capacity retention (Figure 4c).[49]

Besides conductive substrates, carbon materials can also encapsulate active materials to avoid direct contact with the liquid electrolyte. The carbon matrix effectively shields active materials from dissolution and parasitic reactions. Different from carbon-supported structures, for which active materials are anchored on the carbon surfaces or mechanically mixed with carbons, carbon-encapsulated cathodes coat active materials with carbon. Graphene is the most preferred wrap because of its thin 2D structure. The graphene scroll coating MnO_2 can reach an energy density of 406.6 Wh kg^{-1}.[31] Notably, carbon materials are not entirely beneficial. Instead, the compromise between the ratio between carbon outfits and active materials needs to be considered deliberately. The ion pathways will be blocked for completely wrapped active materials, resulting in poor ionic conductivity and inferior capacity. Beyond carbon, other conductive materials like conductive polymers (poly(3,4-ethylenedioxythiophene) (PEDOT), etc.) or special metal–organic frameworks (MOFs) can also function as conductive agents, and remarkable energy densities of 484 and 310 Wh kg^{-1}, respectively, have been reported.[67] However, limited choices of materials and complicated preparation still make them less popular than carbons.

Optimization of the crystal structure also elevates the actual capacity of vast cathodes. A routine method is the preintercalation. Both involve external ions, but the preintercalation differs from the doping technique. For the aforementioned Cu- or CuNa-doped materials, the extra electron-conduction reaction is evoked, upgrading their theoretical capacities. Nonetheless, agents imported through preintercalation play the role of pillars in enlarging the interlayer spacing. Consequently, theoretical capacities by calculating electron transfer do not change, but the practical capacity and cycling stability can be enhanced. Metal ions, polymers, and water molecules have all been implemented as inserted pillars, with metal ions being the most extensive. Most transition metal ions can be preintercalated, especially for V_2O_5 cathodes. Yang et al. have systematically investigated the performance of a series, including Cu^{2+}, Fe^{2+}, Co^{2+}, Ni^{2+}, Zn^{2+}, etc. A convenient hydrothermal method can be utilized to prepare all these, and $Cu_xV_2O_5{\cdot}H_2O$ stands out to provide the most roomy and sturdy space for Zn^{2+} intercalation, as shown in Figure 4d. This enlarged space can also be observed from the slight shift of the (001) plane peak to 7.7°. During the charge/discharge process, the in situ XRD pattern detects a more reversible $Zn_{0.25}V_2O_5{\cdot}H_2O$ species besides the common irreversible $Zn_3(OH)_2V_2O_7{\cdot}2H_2O$ (Figure 4e). This unstable phase ensures the effortless extraction of Zn^{2+}, avoiding capacity fading. As a result, a cheering capacity of 395 mAh g^{-1} is achieved for the first discharge (Figure 4f), and an appealing energy density of 298 Wh kg^{-1} is also realized.[33] Meanwhile, alkali and alkali-earth metal ions can also be inserted into cathode materials. Alkali metal ions, including Li^+, Na^+, and K^+, and alkali earth ions, including Mg^{2+} and Ca^{2+}, have been used to refine layered V- and Mn-based cathodes. The composed $K_{0.5}V_2O_5$ and $K_{0.19}MnO_2$ cathodes obtain energy densities of 309 and 380 Wh kg^{-1}, respectively.[34,68] Meanwhile, the introduction of Ca^{2+} in $V_2O_5{\cdot}H_2O$ delivers an energy density of 381 Wh kg^{-1}, by stretching lattice spacing from 11.4 to 13.3 Å.[35]

Conductive polymers are also auspicious fillers. The elevated electrical repulsion between host cathode materials and Zn^{2+} reduces the energy barrier for Zn^{2+} (de)intercalation and boosts charger carrier' transportation. Specifically, Wang et al. reported that the PANi preintercalated $V_2O_5{\cdot}H_2O$ by in situ polymerization of Aniline in V_2O_5 precursor. The conductive

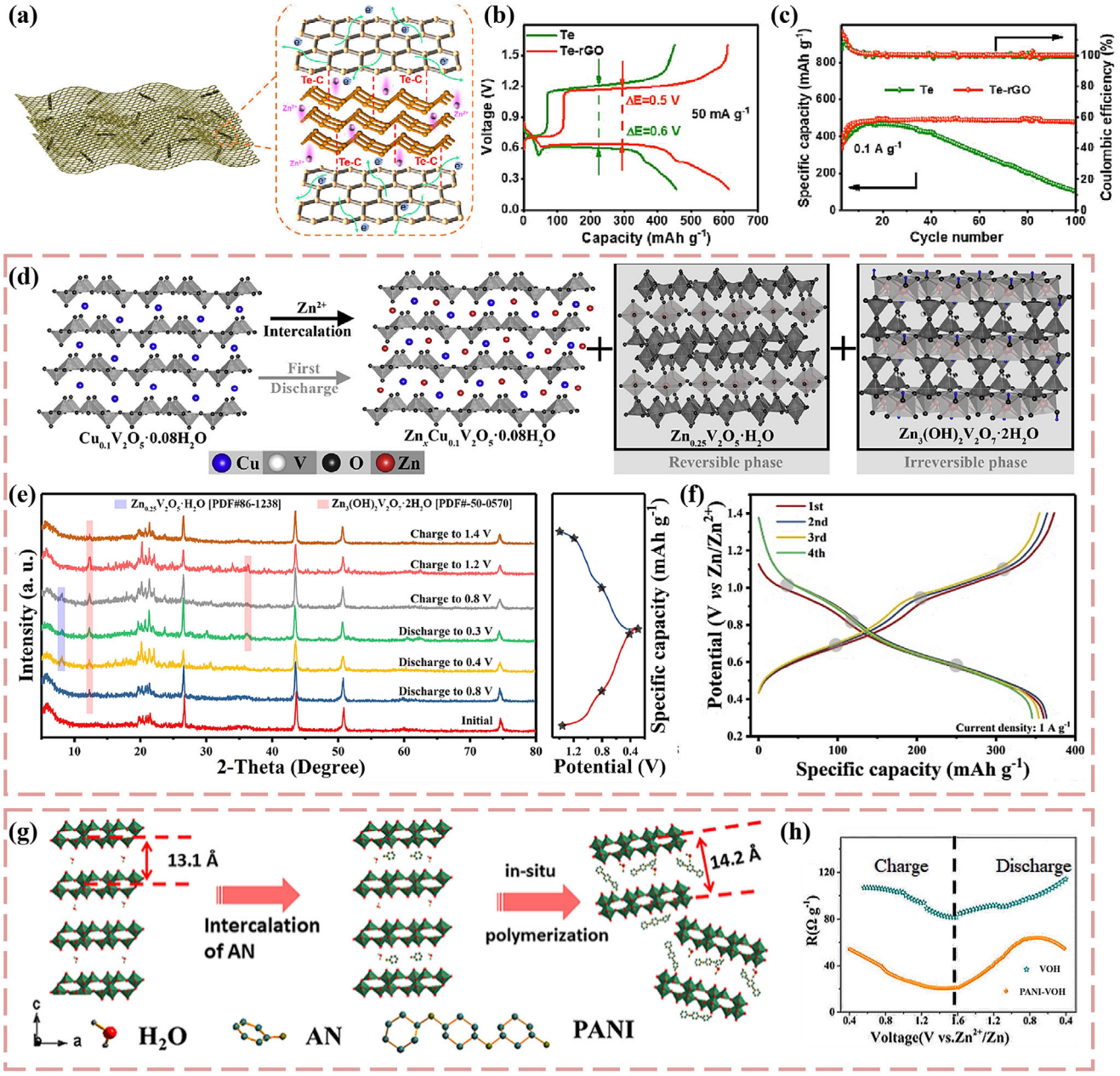

Figure 4. Cathodes with an optimized practical capacity. a) The structure of Te-rGO. b) Galvanostatic charge and discharge voltages of Zn||Te-rGO battery at 0.05 A g^{-1}, and c) cycling stability at 0.1 A g^{-1}. a–c) Reproduced with permission.[49] Copyright 2023, Elsevier. d) Scheme of structure variation of CuVO at the first cycle. e) Ex situ XRD curves at different stages in galvanostatic charge and discharge profiles. f) Galvanostatic charge and discharge voltages of Zn||CuVO battery at 1 A g^{-1}. d–f) Reproduced with permission.[33] Copyright 2019, Elsevier. g) Fabrication process of PANi-VOH. h) Internal reaction resistance curve in Zn||VOH and Zn||PANi-VOH batteries. g,h) Reproduced with permission.[36] Copyright 2020, American Chemical Society.

PANi bridge effectively ensures structural stability. It also lowers the summation of surface layer impedance (R_s) and charge transport impedance (R_{ct}) from 107.5 to 55.5 Ω compared to $V_2O_5{\cdot}H_2O$ (Figure 4h), promoting kinetics to realize an energy density of 216 Wh kg^{-1}.[36] The enlarged layer spacings and reduced impedance were also demonstrated with polypyrrole (PPy)-intercalated $VOPO_4{\cdot}2H_2O$ (PPy-$VOPO_4$), and PEDOT-intercalated $NH_4V_3O_8$ (PEDOT-NVO) cathodes, with favorable capacity improvement to 86 and 87 mAh g^{-1}, respectively.[37,69]

With the energetic development of nanoengineering, besides the crystal structures, multitudinous morphologies of cathodes and some amorphous materials have been designed. These novel morphologies enlarge the contact area between the electrolyte and active cathode materials, so the sites to store Zn^{2+} are increased. Furthermore, shorter distances within these nanostructures ensure the convenient diffusion pathway of ions, facilitating the kinetics. Also, volume variation is not that noticeable for these materials compared to their bulk counterparts, so

Table 3. Performance of high-voltage cathodes.

Cathode material	Testing voltage [V]	Output voltage [V][a,b]	Electrolyte	Capacity [mAh g^{-1}]/ Energy density [Wh kg^{-1}]	Mechanism	Refs.
ZnHCF@MnO_2	1.4–1.9	1.7	0.5 M $ZnSO_4$	118/149	Zn^{2+} intercalation	[95]
ZnHCF	0.8–1.9	1.7	1 M $ZnSO_4$	65.4/100	Zn^{2+} intercalation	[96]
$CoFe(CN)_6$	0.8–1.9	1.75	4 M $Zn(CF_3SO_3)_2$	173.4/-	Zn^{2+} intercalation	[75]
$Cu_2[Fe(CN)_6]$/CNT	0.9–2.2	2.1	NaCl/$ZnSO_4$/SA/H_2O (1:1:0.3:0.8)	260/440	Na^+/Zn^{2+} intercalation and $ZnCl_4^{2-}/Cl^-$ de-intercalation	[97]
$Na_2MnFe(CN)_6$	1.0–2.0	1.6	1 M Na_2SO_4+1 M $ZnSO_4$+8 mM SDS	137/170	Na^+ intercalation	[78]
$Na_3V_2(PO_4)_2F_3$	0.8–1.8	1.62	3 M $Zn(CF_3SO_3)_2$	61/-	H^+ intercalation	[98]
$Na_3V_2(PO_4)_2F_3$	0.8–1.9	1.62	2 M $Zn(CF_3SO_3)_2$	64.7/97.5	Zn^{2+} intercalation	[99]
$LiV_2(PO_4)_3$	0.2–1.9	1.7	4 M $Zn(CF_3SO_3)_2$	146/218	Zn^{2+} intercalation	[100]
$Na_3V_2(PO_4)_3$/C	0.8–1.7	1.52	0.5 M CH_3COONa+0.5 M $Zn(CH_3COO)_2$	92/112	Na^+ intercalation	[101]
$VOPO_4 \cdot xH_2O$	0.7–1.9	≈1.6	13 M $ZnCl_2$+0.8 M H_3PO_4	170/230	H^+/Zn^{2+} co-intercalation	[102]
Co^{3+}-rich Co_3O_4	0.8–2.2	2	2 M $ZnSO_4$+0.2 M $CoSO_4$	205/360.8	Co_3O_4/CoO conversion	[77]
$Co_{0.24}7V_2O_5 \cdot 0.944H_2O$	0.6–.2.2	1.7	1 M $Zn(CF_3SO_3)_2$+21 M $LiC_2F_6NO_4S_2$	432/432	Zn^{2+} intercalation	[103]
$MgMn_2O_4$	0.5–1.9	1.5	1 M $ZnSO_4$+1 M $MgSO_4$	96/370	Zn^{2+}/Mg^{2+} co-intercalation	[104]
$Ti_3C_2I_2$ MXenes	0.8–1.8	1.62, 1.30	2 M $ZnSO_4$+2 M $ZnCl_2$+2 M KCl	207/280	$I^-/I^0/I^+$ conversion	[90b]
Ni-Fe mixed I_2	0.3–1.65	1.51, 1.22	1 M $ZnSO_4$+0.2 M $ZnBr_2$ in PAM hydrogel	350/-	$I^-/I^0/I^+$ conversion	[105]
Fe_{SA}-NC/I_2	0.6–1.8	≈1.7, 1.2	10 M $ZnCl_2$+8 M MeCN	513.2/421.9	$I^-/I^0/I^+$ conversion	[91b]
CuPc@CNT-ZnI_2	0.6–1.8	≈1.6, 1.2	3 M $ZnSO_4$	229/233.8	$I^-/I^0/I^+$ conversion	[90a]
I_2@Co_9S_8@NC	0.6–1.7	≈1.6, 1.2	7.5 M $ZnCl_2$	458/554	$I^-/I^0/I^+$ conversion	[90c]

[a] The working voltage is from values reported in publications. If they did not report, the medium of the discharge plateau is chosen as the working voltage; [b] Working voltages for I composite anodes referred to mediums of two discharge plateaus for four-electron transfer.

the cycling stability can be guaranteed. Currently, comprehensive cathodes with optimized morphologies including nanorods, nanosheets, nanospheres, etc., have been presented. For example, Islam et al. synthesized the β-MnO_2 nanorods with exposed (101) planes. The combined mechanism of solid solution and (de)intercalation is confirmed, contributing to an elevated capacity. Moreover, the nanorods morphology shows minimal variation even after 200 cycles. As a result, a discharge capacity of 270 mAh g^{-1} can be obtained.[70] Morphology optimization is also effective for V-based oxides. Cao et al. used the hydrothermal method to fabricate the VO_2 nanoplates with a middle hole (ancient Chinese coin-like). This hollow structure further enlarges the electrolyte-accessible area, significantly enhancing the mass transfer in cathodes. Even after cycling, the ancient Chinese coin shape is still maintained even though the aggregation of different nanoplates happened. Combining these merits, a high initial capacity of 183.9 mAh g^{-1} at 3 A g^{-1}, and a shocking capacity retention of 81.2% after 1200 cycles are realized.[71] Following the similar design thinking, researchers proposed diverse amorphous cathodes. The structural disorder is extremely high for these amorphous materials, so active sites can be maximized. Meanwhile, electrostatic force is completely relaxed, facilitating the consistent stable operation. Up to now, both the amorphous MnO_2 and V_2O_5 have been reported using the simple solution method with the high initial capacity of 304.4 and 348 mAh g^{-1}, respectively.[72]

In addition to manipulating with the homogeneous cathode, the construction of heterostructures possesses the synergistic advantages of structures and shows effectiveness to facilitate the ion/charge transfer due to their boosted interface reaction kinetics.[73] Specifically, the contact of two materials with different energy bandgaps will cause the flow of electrons from the one with the low work function to the one with the high work function until the equilibrium between them is successfully established. Thus, the built-in electric field (BIEF) is realized at the interface. This intrinsic electric motivation facilitates the transfer of ions, boosting the kinetics. For example, Chen et al. fabricated the TiS_2-TiO_2 heterojunction cathode with the vapor phase anion-exchange method. The work functions for TiS_2 and TiO_2 are 5.74 and 6.86 eV, respectively, so electrons spontaneously transfer from TiS_2 to TiO_2 seeking the equilibrium in their Fermi levels. Attributed to the boosted kinetics, a fast charging process can be realized, and the final capacity reaches 187.7 mAh g^{-1} at 0.1 A g^{-1}.[74]

2.2. High Working Voltage Cathodes

Energy density relies on capacity and working voltage, but the operation voltage for current cathode materials is substandard. The decent discharge voltage for MnO_2 and V_2O_5 cathodes are 1.35 and 0.7 V, correspondingly. Even for PBAs, the renowned high-voltage cathode, the discharge voltage is only 1.7 V. Therefore, an elevated working voltage is crucial for high-energy-density AZIBs (**Table 3**).

Further optimization of PBAs is a focus on designing high working voltage cathodes, and one strategy is incorporating another one-electron redox reaction to increase the original redox active center to multiple. Couples like the transition of Co^{2+}/Co^{3+} and Mn^{3+}/Mn^{4+} were put into practice. For example, Ma et al. synthesized the $CoFe(CN)_6$ by fabricating the $KCoFe(CN)_6$ cubes

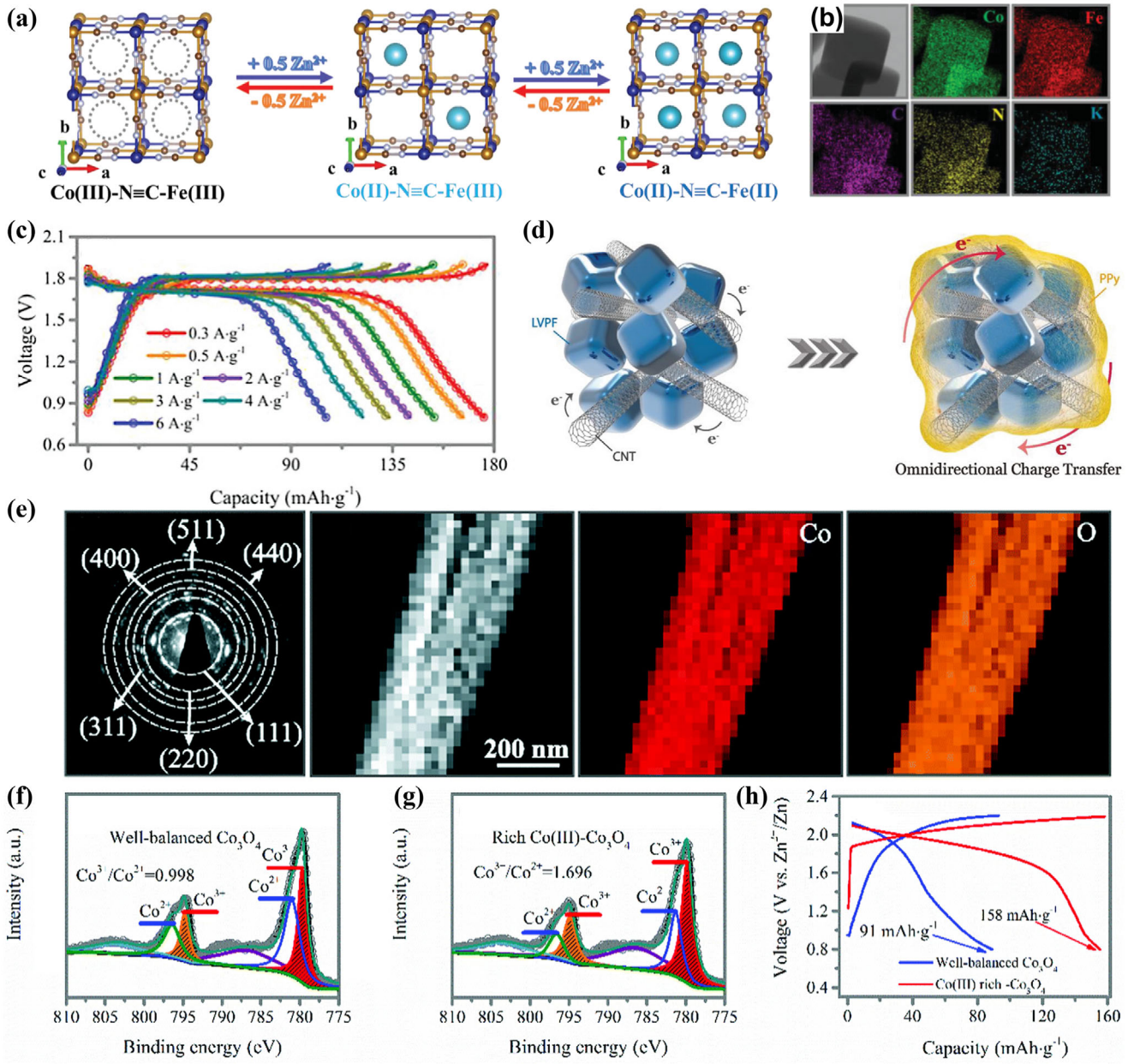

Figure 5. Cathodes with a high working voltage. a) Schematic illustration of Zn^{2+} (de)intercalation process in $CoFe(CN)_6$. b) TEM images of $KCoFe(CN)_6$ cubes. c) Galvanostatic charge and discharge voltages of Zn||$CoFe(CN)_6$ batteries at different current densities. a–c) Reproduced with permission.[75] Copyright 2019, Wiley-VCH. d) Schematic illustration of the fabrication of LVPF-CNTs-PPy composite. d) Reproduced with permission.[76] Copyright 2019, Wiley-VCH. e) Co(III) rich-Co_3O_4 crystal structure along the *b*-axis, STEM-HAADF image, and EDS mapping. XPS spectra of Co 2p for f) Co_3O_4, and g) Co(III) rich-Co_3O_4. h) Charge/Discharge curves of Zn||Co_3O_4, and Zn||Co(III) rich-Co_3O_4 batteries. e–h) Reproduced with permission.[77] Copyright 2018, Royal Society of Chemistry.

and then extracting K^+ with the electrochemical method. Vacancies left by K^+ show a preference for Zn^{2+} (de)intercalation, and this procedure happened in two steps for different activation energies of Co(III)/Co(II) and Fe(III)/Fe(II) redoxes (**Figure** 5a,b). Consequently, a stable discharge plateau of 1.75 V can be achieved, gathering a capacity of 173.4 mAh g^{-1} at 0.3 A g^{-1} (Figure 5c).[75] Others like $Na_2MnFe(CN)_6$ also reached a discharge voltage of 1.6 V with an energy density of 236 Wh kg^{-1}.[78] Inspired by vigorous valence state changes because of $Fe(CN)_6^{3-}$ in PBAs, other high-order anions like PO_4^{3-}, and PO_4F^{4-} are also paired with high-voltage redox couples.[79] The fabricated $VOPO_4$ and $LiVPO_4F$ (Figure 5d) show working voltages of 1.56 and 1.65 V separately, contributing to energy densities of 216 and 230 Wh kg^{-1}.[76,80] This strategy of anchoring high-voltage redox-active centers has been extended to high order anions-free cathodes like Co_3O_4. For example, Ma et al. synthesized the Co^{3+}-rich Co_3O_4 nanorods with Co and O homogeneously distributed (Figure 5e) by appending excessive $Co(NO_3)_2$

during the hydrothermal process. By conducting the quantitative analysis of XPS results, shown in Figure 5f,g, of Co_3O_4 and Co^{3+}-rich Co_3O_4, the Co^{3+}/Co^{2+} ratio shows an elevation from 0.998 to 1.696. The rich Co^{3+} balances the structure, enhancing the working voltage and capacity. Consequently, a working voltage of 1.8 V, a discharging capacity of 158 mAh g^{-1} at 1 A g^{-1} (Figure 5h), and an energy density of 360.8 Wh kg^{-1} at 0.5 A g^{-1} are exhibited.[77]

Luckily, in the past few years, halogen has emerged as conversion-type cathodes showing favorable discharge plateaus, with iodine as the representative. Much progress has been achieved on the $2e^-$ zinc-iodide battery with the I^-/I_2 conversion as the cathodic redox.[81] Typically, a stable discharge platform at around 1.25 V can be realized to attend a discharge capacity of about 200 mAh g^{-1}. However, challenges still remain for their practical application. The issues of Zn||I_2 batteries are similar to those of the chalcogens: poor electronic conductivity (10^{-6}–10^{-9} S m^{-1}), sluggish kinetics (especially for halogens reduction), and the shuttle effect.[82] The shuttle effect is also because of the dissolution of iodine traveling toward zinc anodes.[83] To grant the I_2 with conductivity, conductive carbon supports are also necessary. However, the binding force between common carbon materials and I_2 is not strong enough, causing easy sublimation of active materials. Thus, strategies to enforce binding in cathodes, suppress mitigation of I_3^- diffusion, and isolate zinc anodes from adsorbing iodine become necessary. As a result, most electrode engineering strategies focus on intensive polyiodide anchoring. Currently, heteroatoms including N, O, S, etc., and functional groups have been confirmed as effective doping for their flourishing defects and active sites, adsorbing polyiodides well.[84] Moreover, using binders like chitosan with polar chains binding more strongly with iodine or employing iodide compounds instead of I_2 is also impactful for consolidating the cathode.[85] For the perspective of electrolyte engineering, various additives like halide ammonium,[86] poly(2-vinylpyridine),[87] 1-ethyl-2-methyl-pyridinium bromide,[88] etc., have confirmed their efficacy. Their functions are more related to anode-induced parasitic reactions (HER, Zn to ZnO passivation, etc.), but the generation of polyiodide is still serious in these aqueous electrolytes. To inhibit the mitigation of I_3^-, quasisolid and ion-selective solid electrolytes are more compromising than their aqueous counterparts because of their solid–solid interfaces and repulsive nature to anions. For example, Jin et al. fabricated a crosslinked hydrogel (CPAM), and made it saturated with $ZnSO_4$ containing 1-methyl-3-*n*-propylimidazolium iodide as the electrolyte. The shuttle effect is minimized without the aqueous environment, and the capacity retention is 89.2% after an impressive 2600 cycles of operation.[89] Because the loss of active materials is caused by a sequential reaction of dissolution of the cathodes and reaction with the anodes. The suppression of I_3^- conduction can also be achieved by fabricating protective membranes on the zinc anode to avoid the iodide-derived zinc corrosion.

The working voltage of the I_2 cathode can be further improved if an extra $2e^-$ transfer can be evoked. After conversion between the I^- and I_2, the further oxidation to I^+ can be realized at about 1.75 V, elevating the theoretical capacity to 422 mAh g^{-1}. However, the reversibility of this $4e^-$ pathway is not satisfactory because of the hydrolysis of I^+. Thus, avoiding the loss of the I^+ species can make the I cathode a genuine high-voltage candidate. Typically, cathode optimization and electrolyte engineering are beneficial for promoting I_2/I^+ reactions. Conventional carbon hosts cannot catalyze the transition to I^+, so selecting hosts with a stronger affinity to I^+ is indispensable. Pioneering publications have reported MOFs, metal-phthalocyanine, single atoms, some sulfides, etc., as productive trimmings.[90] For example, Liu et al. adsorbed I_2 on the Fe single atom anchored on N-doped porous carbon (Fe_{SA}-NC) as the cathode. According to the orbital symmetry and electron occupation rules, the Fe d_{z2} orbital hybridizes well with the iodine p_z orbital to consolidate the interaction with I^+ and accelerate the electron transfer. As a result, two platforms at 1.7 and 1.2 V appear in discharge curves, respecting the two conversion steps, assisting a superior energy density of 421.9 Wh kg^{-1}.[91] The electrolyte engineering for $4e^-$ redox typically includes generating hetero-halogen compounds by introducing Br, Cl, and F. However, the hydrolysis of these compounds is also easy, and finally, the I^+ is converted back to I_2. Therefore, the concentration of alien halogens should be high to suppress the water activity. For example, Xie et al. used 7.5 M KI containing 3.75 M $ZnBr_2$ as the electrolyte for a zinc-iodine single-flow battery, exhibiting a high energy density of 205 Wh L^{-1}.[92] More encouragingly, the assistance of Br/Br^- conversion can even evoke the 12 electron conversion by generating IO_3^-. Ma et al. used the 0.1 M H_2SO_4 with 0.1 M KBr as the electrolyte for the iodine side. During the cycling process, besides the $4e^-$ pathway mentioned above, an extra conversion combining Br^- and IO_3^- to form Br_2 and IBr happened at the plateau higher than 1.7 V (**Figure 6**a,b). This luxuriant charge transfer helped exhibit a record-breaking initial capacity of 1200 mAh g^{-1} (an energy density of 1357 Wh kg^{-1}) (Figure 6c). However, the rapid capacity degradation can be observed, retaining only about 700 mAh g^{-1} of capacity after 70 cycles. Therefore, for practical conjugating with the Zn anode, extra zinc sources were necessary, and Ma et al. supplemented zinc in the form of the zinc salts to compensate Zn^{2+}. As shown in Figure 6d,e, with $ZnSO_4$ salts as additional zinc sources, a capacity of about 900 mAh g^{-1} can still be reached with superior retention. Thus, the synergistic improvement of both cathode mechanism and zinc anode stability is crucial for the long-term energy density performance.[93] In later research, Xie et al. further explored the decomposition of charge transfer in detail to provide more chances to couple with other promising metal anodes (Figure 6f).[94]

Even though cathodes with the unique high-capacity or high-voltage merit function well for elevating the energy output, the ultimate goal is still formulating cathodes with both high capacity and high voltage. This destination sets forth new demands on the electrolyte. The high-capacity cathode depends solely on the cathode active materials. In contrast, the high-voltage is further limited with the ESW of the electrolyte. If the voltage exceeds the ESW, the electrolysis of electrolyte will occur, causing the loss of electrolytes and more severe interfacial parasitic reactions. Those corresponding side reactions will exacerbate the degradation of both the cathode and anode. Therefore, electrolytes with an extended ESW are crucial for providing a pairing potential window to realize full values of those advanced cathodes and provide a higher degree of freedom for designing cathodes. As a result, the energy out can be further boosted.

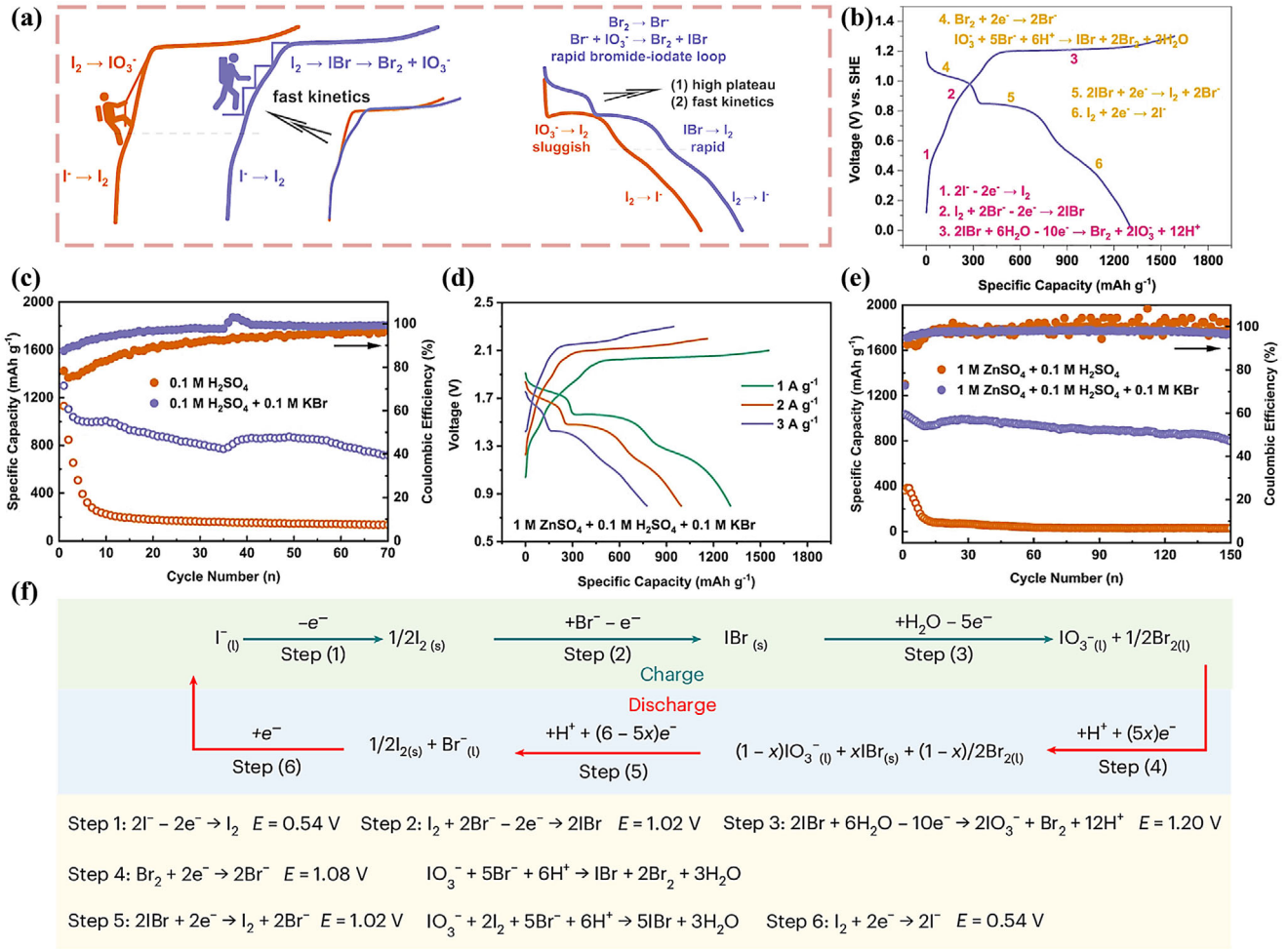

Figure 6. Halogen cathodes with multiple electron transfer. a) Schematic illustration of charge and discharge process of I_2/HAC electrode with and without KBr. b) The voltage profiles with notations of reactions. c) Cycling performance of the I_2/HAC electrode with different electrolytes. d) Galvanostatic charge and discharge curves and e) cycling performance of Zn||I_2 battery with different electrolytes containing $ZnSO_4$. a–e) Reproduced under the terms of the CC-BY Creative Commons Attribution 4.0 International license.[93] Copyright 2023, W. Ma et al., published by Springer Nature. f) Schematic illustration of the charge process with Br^- additives. f) Reproduced with permission.[94] Copyright 2024, Springer Nature.

3. High-Energy-Density AZIBs via ESW-Wide Electrolytes

For the high energy output, if advanced cathodes are its trunk, electrolytes with the wide ESW are leaves. If the support from leaves disappears, even the strongest trunk is on the verge of death, with no need to discuss the further growth. Thus, electrolytes with the ESW conjugated with those cathodes with high-voltage should be designed to ensure stable operation. Dissimilar to organic electrolytes, the water electrolysis potential (1.23 V vs SHE) constrains the ESW of a water-based system. Considering the hydrogen evolution inertness of zinc, 2.0 V is usually the roof of AZIBs operation. Therefore, the expansion of the ESW can be summarized as the process to hinder the filtration of H_2O on the electrode/electrolyte interface. This can be achieved by reducing H_2O molecules at the electrode/electrolyte interface or immobilizing free water. The water lean interface is realized through modification of the solvation structure or in situ hydrophobic layer fabrication through surface adsorption. Free water immobilization is common in concentrated electrolytes (water-in-salts electrolytes, i.e., WiSE) or quasisolid electrolytes. Besides, decoupled electrolytes combining acidic-alkaline redox with an expansive potential difference are emerging (**Figure 7** and **Table 4**).

3.1. Widen ESW by Reducing Interfacial Water Contents

The ESW of the aqueous batteries falls into the potential difference between the hydrogen evolution reaction (HER) and oxygen evolution reaction (OER), which are water-induced parasitic reactions. Thus, isolating electrodes from water through the construction of an in situ hydrophobic layer and water-lean solvation sheath will effectively broaden the ESW.

The hydrophobic layer can be formed via the surface adsorption of additives, and typical ones are surfactants.[106] The high polarity at the ends of surfactants enables them to be chemically adsorbed on the zinc surface. Their hydrophobic chains are exposed to the electrolyte to show the steric hindrance of solvated

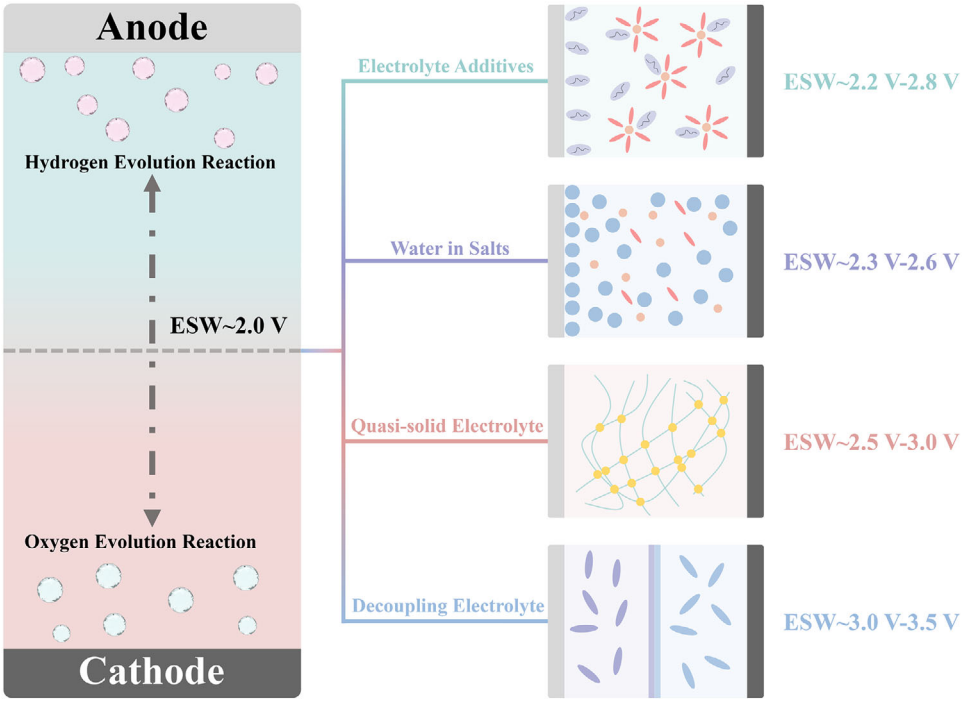

Figure 7. The summary of different electrolyte engineering strategies to expand the electrochemical stability windows in AZIBs.

zinc ions. Furthermore, the fabricated organic layer can physically isolate water contents from the zinc anode. Consequently, the ESW can be effectively widened due to the inactive water electrolysis. For example, adsorption of sodium dodecyl sulfate (SDS) results in an inert layer, expanding the ESW to 2.5 V by increasing the OER potential from 1.1 to 1.4 V (vs SHE), while decreasing the HER potential from −0.7 to −1.15 V (vs SHE).[78]

The reconstruction of the solvation structure of Zn^{2+} results from the competition between water and molecules that show a high binding energy with Zn^{2+}. Common solvation structure in mild acidic system is $[Zn(OH_2)_6]^{2+}$ (for $ZnSO_4$, $Zn(ClO_4)_2$, $Zn(TFSI)_2$, etc.). Six water molecules will surround each Zn^{2+}, reaching the active electrode/electrolyte interface to initiate the water electrolysis.[107] Thus, substituting water in the sheath with organic molecules will be beneficial. Multiple organic solids have confirmed the participation in the solvation sheath with a low concentration.[108] Attributed to strong adhesive forces with Zn^{2+} from three O═C—OH groups, the trisodium citrate (TSC) molecule can even elbow three water molecules out of the sheath at a concentration of 0.1 M (**Figure 8a**), beneficial for a broad capacity elevation in the whole current range (Figure 8b).[109] However, these trace amounts of additives only occupy a low proportion of electrolytes compared to zinc salts. Therefore, it is impossible for them to participate in solvation sheaths of all solvated zinc ions. As a result, the ESW cannot be overwhelmingly expanded. Contrarily, organic liquids freed from limitations of solubility can show more striking ESW expansion, reflected more intuitively from the experimental evaluation of the ESW. As an example, PEG-400 can be incorporated up to 80 wt% due to its outstanding adhesion with $Zn(OTf)_2$. As shown in Figure 8c, through favored hydrogen bonding interactions between O in PEG and H in H_2O, abundant PEG molecules and more OTf^- anions are brought into the Zn^{2+} solvation sheath. Then, luxuriant anions are carried to the anode surface, facilitating the ZnF_2 solid electrolyte interface (SEI) formation. Accordingly, a shocking ESW of 4.56 V (vs SHE) was realized by replacing two water molecules in the solvation sheath (Figure 8d). Consequently, the fabricated $Zn||V_2O_5$ batteries present high discharging capacities ranging from 345.7 to 196 mAh g^{-1} when current densities increase from 0.5 to 10 A g^{-1} (Figure 8e), and a high energy density of 324.3 Wh kg^{-1} is recorded, which overwhelms the additive-free counterpart (Figure 8f,g).[110] This strategy is also effective in the most routine $ZnSO_4$ electrolytes, and outstanding outcomes include the addition of glycerol and methanol (Figure 8h), both exhibiting an ESW larger than 3 V with 50 vol%.[111]

It is noteworthy that the broader charge/discharge range exerts more severe demands on the cathode materials. Substantial cathode materials will be decomposed at high electrode potential. Thus, voltage limits during full-cell tests are commonly unmodified, even when a broader ESW is detected. As a result, no obvious improvement in incipient energy densities is observed in these publications. Fortunately, within these conservative voltage ranges, the optimized electrolyte invariably renders advanced capacity retention by suppressing both cathodic and anodic parasitic reactions. Consequently, the energy density is kept at a high level after consistent cycling.

3.2. Widen ESW by Reducing Free Water in Electrolytes

Restricting free water is another effective strategy to suppress water electrolysis and expand the ESW. The freezing water network can be detected in concentrated electrolytes (e.g., WiSEs), and (quasi)solid electrolytes.

Table 4. Performance of electrolytes with wide ESW.

Type	Electrolyte composition	ESW [V]	Cathode	Capacity [mAh g^{-1}]/Energy density[Wh kg^{-1}]	Capacity in pouch cell [mAh g^{-1}][a)]	Refs.
Aqueous	1 м Na_2SO_4+1 м $ZnSO_4$+8 мм SDS in H_2O	2.55	$Na_2MnFe(CN)_6$	137/170	–	[78]
	2 м $ZnSO_4$+1 м ESA in H_2O	2.594	MnO_2	250.6/-	–	[106b]
	2 м $ZnSO_4$+0.05 мм TBA_2SO_4 in H_2O	≈2.4	α-MnO_2	220/-	–	[127]
	1 м $ZnSO_4$+75 мм Na_2EDTA in H_2O	≈2.6	VO_2	120/-	–	[128]
	2 м $ZnSO_4$+10 мм Aspartame in H_2O	2.75	$Cu_xV_2O_5$	255.36/-	–	[129]
	2 м $ZnSO_4$+25 мм NHM in H_2O	0.033 wider	$NH_4V_4O_{10}$	400/-	138.1 at 6.75 mA cm^{-2}	[130]
	2 м $ZnSO_4$+30 мм MBA in H_2O	2.53	$NH_4V_4O_{10}$	172/-	270 at 4 mA cm^{-2}	[131]
	2 м $ZnSO_4$+20 мм TN in H_2O	0.108 wider	VOX	270/-	≈33 mAh cm^{-2} at 50 mA g^{-1}	[132]
	$Zn(ClO_4)_2$+$NaClO_4$+$LiClO_4$ in H_2O (molar ratio = 0.2:0.4:0.4:7)	2.76	NaVO	200/-	180 at 0.5 mA cm^{-2}	[133]
	1 м $Zn(CF_3SO_3)_2$ in 30 wt% H_2O+70 wt% PEG-400	4.56	V_2O_5	345.7/324.3	–	[110]
	2 м $ZnSO_4$ in 50 vol% H_2O+50 vol% Glycerol	2.3	$CaV_6O_{16}{\cdot}3H_2O$	136/-	–	[111a]
	2 м $ZnSO_4$ in 50 vol% H_2O+50 vol% Methanol	≈2.45	PANi	213.3/-	100.8 at 5.56 mA cm^{-2}	[111b]
	1 м $ZnCl_2$ in H_2O/DMSO mixture (molar ratio = 17:1)	2.2	MnO_2	158/212	–	[134]
	2 м $ZnSO_4$ in 60 vol% H_2O+40 vol% EG	2.8	PANi-V_2O_5	180/121	–	[135]
	1 м $Zn(C_2F_6NO_4S_2)_2$ in H_2O/sulfolane (molar ratio = 1:1)	2.8	VOH	400/-	1320 at 0.1 A g^{-1}	[136]
	0.5 м $Zn(CF_3SO_3)_2$ in 30 wt% H_2O+70 wt% TEP	2.25	KCuHCF	73.3/-	–	[137]
Water in salt	30 м $ZnCl_2$ in H_2O	2.3	–	–	–	[113]
	30 м $ZnCl_2$ in H_2O	>2.54	V_2O_5	341/-	–	[114]
	0.5 м $ZnSO_4$+21 м $LiC_2F_6NO_4S_2$ in H_2O	>3.5	$LiMn_{0.8}Fe_{0.2}PO_4$	140/183	–	[116a]
	3 м $Zn(CF_3SO_3)_2$+21 м $LiC_2F_6NO_4S_2$ in H_2O	2.6	Graphite	27/-	–	[116b]
	30 м CH_3COOLi+3 м CH_3COOLi+3 м $Zn(CH_3COO)_2$ in H_2O	>2.2	$LiFePO_4$	155/-	–	[138]
	$Zn(BF_4)_2$ saturated in PAM gel	≈2.5	PANi/SWCNT	112.5/106.3	112.5 at 0.1 A g^{-1}	[121]
Quasisolid[b)]						
	3 м $Zn(ClO_4)_2$ in PAM/Glucose gel	≈2.6	$NH_4V_4O_{10}$	438.1/-	461 at 0.1 A g^{-1}	[122a]
	$ZnSO_4$ in PAM/MWCNTs gel	≈2.85	MnO_2	269/-	269 at 0.5 A g^{-1}	[122c]
	1 м $Zn(ClO_4)_2$ in PAM/SA gel	2.55	NaV_3O_8	364.8/-	216 at 1 A g^{-1}	[123]
	1 м $ZnSO_4$ in PAM/Agarose/Cellulose gel	≈2.4	α-MnO_2	304/-	304 at 0.5 A g^{-1}	[124]
	2 м $Zn(ClO_4)_2$ in PAM/Chitosan gel	≈3	$Cu_xV_2O_5$	330/-	330 at 0.5 A g^{-1}	[139]

[a)] The areal capacity is calculated from the specific capacity and the approximate mass loading; [b)] For capacities same for cells and pouch cells, the full batteries are evaluated in pouch cells directly without using coin cells. This is common for hydrogel batteries.

WiSEs are electrolytes with ample salts "dissolved" in minimum water, so their concentrations are always higher than 10 м. In WiSEs, excessive cations are hydrated easily due to their denser charge distribution, leaving anions with a larger size and more delocalized charge distribution undissolved. Then, the nanostructure of the WiSEs is identified as the hydrated cation domain and the dry anion domain. Considering the anions' inherent hydrophobic nature and cations' hydrophilic nature, the free water will be tightly locked between cations and the anions domain.[112] Currently, $ZnCl_2$, with ultrahigh solubility, is most commonly used to prepare WiSEs without any solubilizer. Zhang et al. proposed that the solubility of $ZnCl_2$ can reach 30 м, and the final WiSE electrolyte provides a stretching ESW of 2.3 V.[113] In a later study, Tang et al. used the 30 м $ZnCl_2$ electrolyte in Zn||V_2O_5 batteries (**Figure 9a**). Concentrated salts result in the insertion of dehydrated Zn^{2+}, which is much smaller than its hydrated counterparts. As a result, the layer spacing expansion is decreased from 13.9 to 4.4 Å (Figure 9b), avoiding the structure collapse caused by high internal stress. Finally, a high specific capacity of 341 mAh g^{-1} is obtained with negligible capacity decay in 300 cycles.[114] WiSEs can also be fabricated by introducing additives with superior solubility. The most successful implementation is the LiTFSI additive (solubility ≈21 м). The $TFSI^-$ anions are attractive in multitudinous battery systems because of rich F-sources for fluorine-contained SEI, but the zinc anode shows deficient reversibility with the $Zn(TFSI)_2$ electrolyte due to rampant side reactions. Thus, WiSEs using the $Zn(TFSI)_2$ as a zinc conductor and concentrated LiTFSI as the additive is attractive by suppressing side reactions and taking full advantage of F elements simultaneously.[115] Furthermore, the 21 м LiTFSI additive performs well in other common salt systems like $ZnSO_4$ and $Zn(OTf)_2$. The ESWs for these as-prepared electrolytes are usually larger than 2.6 V.[116]

Water networks can also be locked by hydrophilic polar function groups (amidogens, carboxyls, and carbonyls) on the organics. Once these organics are used as additives with a trace

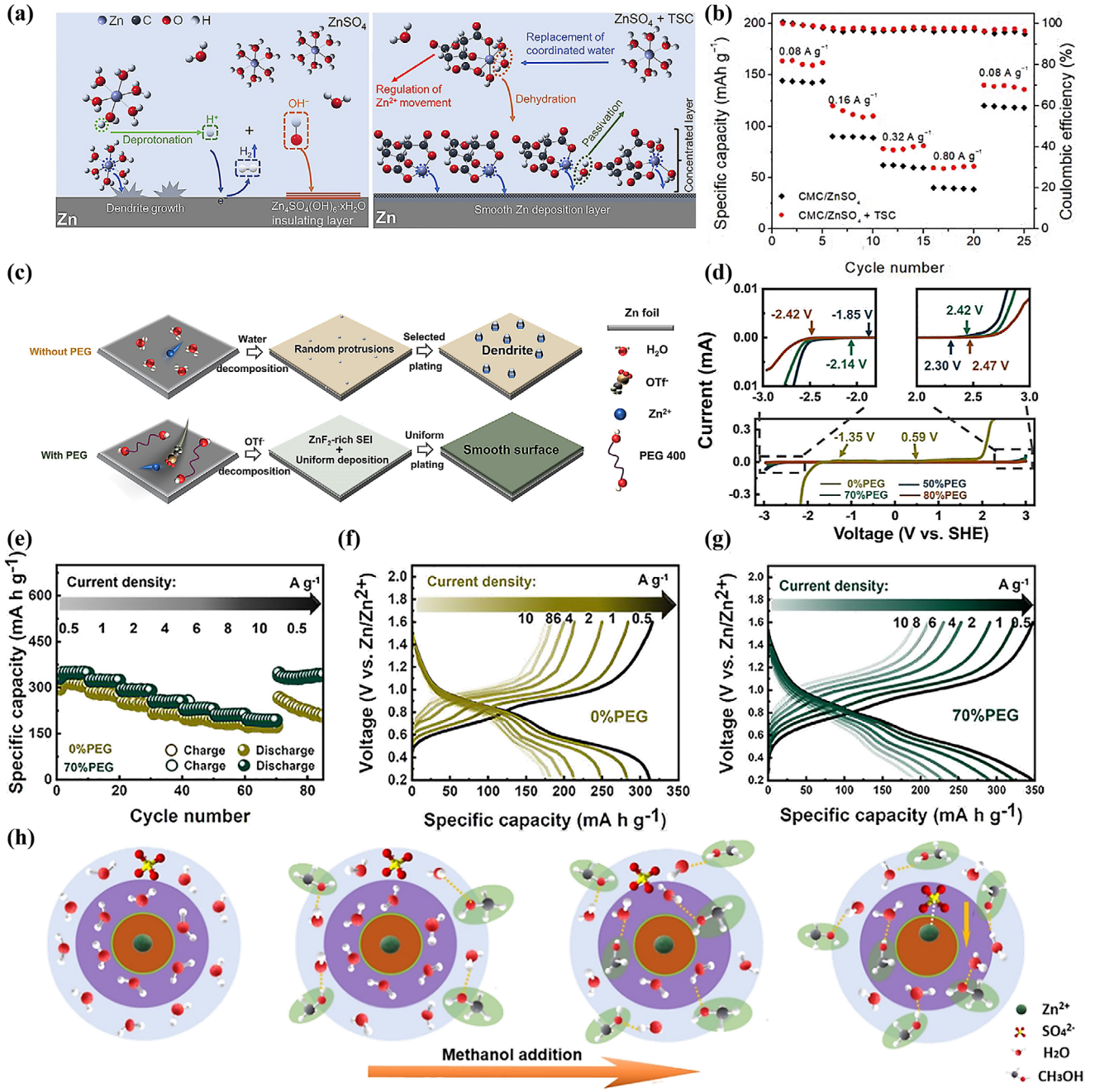

Figure 8. Electrolyte additives for reducing water contents on the electrode/electrolyte interface. a) Schematic illustration of deposition behavior in electrolytes without and with TSC additive. b) The rate performance of Zn||PPy/PEDOT: PSS battery. a,b) Reproduced with permission.[109] Copyright 2021, Elsevier. c) Schemes of solvation structure change and surface adsorption behavior caused by PEG additive. d) LSV curves with electrolytes containing different concentrations of PEG. e) Rate performance of Zn||V_2O_5 batteries. Discharge/charge voltage profiles of Zn||V_2O_5 batteries f) without, and g) with PEG additives. c–g) Reproduced with permission.[110] Copyright 2022, Elsevier. h) Schemes of solvation sheath change by the introduction of methanol. h) Reproduced with permission.[111b] Copyright 2021, Wiley-VCH.

amount, they are functional only at the interface, so the comprehensive existence of these polar groups is required to reconstruct the H-bonding structure across the whole electrolyte. Therefore, hydrogel electrolytes with polar groups-rich skeletons stand out. Currently, a wide range of polymers, PAM,[117] PVA,[67a] sodium alginate (SA),[118] carboxymethylcellulose (CMC),[119] xanthan gum[120], etc., demonstrate the efficacy to fabricate hydrogel electrolytes, with PAM and PVA the most comprehensively investigated for their excellent mechanical property and the facile fabrication process. These hydrogel electrolytes will show decent stability by being prepared with zinc salts dissolved in the precursor or by electrolytes adsorption after polymerization. For

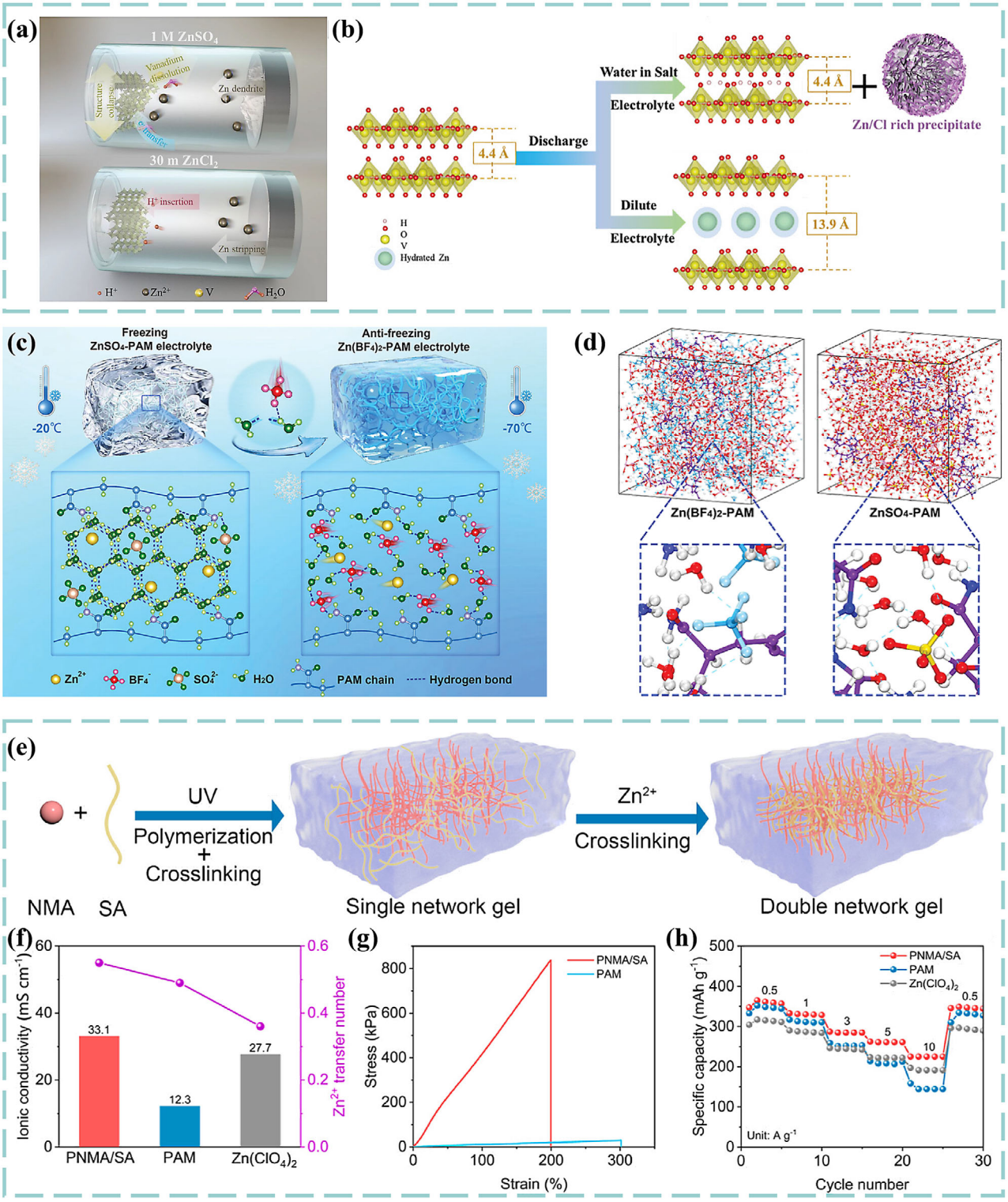

Figure 9. Strategies to reduce free waters in electrolytes. a) Scheme of AZMBs with 1.0 M $ZnSO_4$ and 30 M $ZnCl_2$ electrolytes. b) Structure variation of V_2O_5 cathode with different electrolytes. a,b) Reproduced under the terms of the CC-BY Creative Commons Attribution 4.0 International license.[114] Copyright 2021, X. Tang et al., published by Wiley-VCH. c) Scheme and d) MD simulations of $ZnSO_4$-PAM and antifreezing $Zn(BF_4)_2$-PAM hydrogel electrolytes. c,d) Reproduced with permission.[121] Copyright 2023, Wiley-VCH. e) Synthesis process of PNMA/SA hydrogel. f) Ionic conductivities of PNMA/SA, PAM, and liquid $Zn(ClO_4)_2$ electrolytes. g) Stress–strain curves of PNMA/SA and PAM hydrogels. h) Rate performance of Zn||NVO batteries with PNMA/SA, PAM, and liquid $Zn(ClO_4)_2$ electrolytes. e–h) Reproduced with permission.[123] Copyright 2024, American Chemical Society.

example, $Zn(BF_4)_2$ salts can be added in the precursor containing acrylamide (AM) monomer, initiator, and crosslinker. After thermos-crosslinking, the final $Zn(BF_4)_2$-PAM hydrogel (Figure 9c) is fabricated. The ESW is stretched to 2.6 V in prepared hydrogels, attributed to the reinforced ternary hydrogen bonding networks among H_2O, PAM, and BF_4^- (Figure 9d).[121] Moreover, hydrogels are also flexible for comprehensive paddings like organic molecules, polymer quantum dots, active carbons, etc., to gain the further optimization.[122]

Despite the satisfactory ESW, homopolymers show mediocre mechanical strength, and ionic conductivity is reduced due to restricted water content. Thus, multiple-network hydrogels are designed by copolymerizing polymers with superior mechanical strength and others with strong affinity with Zn^{2+} to achieve a balance. For example, poly-*N*-hydroxymethyl acrylamide (PNMA), the variant of PAM with additional hydroxymethyl groups, can be self-crosslinked, resulting in a higher degree of crosslink. Thereupon, the trimmed water retention benefits the strength but impairs the conductivity. Encouragingly, SA, which can accelerate ion transportation by altering the solvation of Zn^{2+}, remedies this disadvantage. As a result, Zeng et al. prepared the PNMA/SA hydrogel by adding SA during the polymerization of *N*-hydroxymethyl acrylamide (NMA) (Figure 9e), and this copolymer delivers a tensile strength of 838 kPa (30 kPa for PAM), an ionic conductivity of 33.1 mS cm^{-1} (Figure 9f,g), and an ESW of 2.55 V. The fabricated Zn||NVO batteries also display a high specific capacity of 364.8 mAh g^{-1} at 0.5 A g^{-1} (Figure 9h).[123] The extraordinary performance of other copolymers like PAM/CMC,[124] PAM/gelatin,[125] PAM/chitosan,[126] etc., confirm this design philosophy.

3.3. Widen ESW by Decoupling Electrolyte

Homogeneous electrolytes mentioned above depend on the same charge carriers for both electrodes, confining the redox couple and limiting the theoretical ESW. This restriction has been relaxed recently for the blossoming of ion exchange membranes. By segregating the anode and cathode, asymmetric electrolytes adopting redox couples with extended potential differences become feasible.

For example, as shown in **Figure 10a**, Xu et al. utilized the KOH solution and H_2SO_4 as electrolytes for the zinc anode and PbO_2 cathode separately in the Zn||PbO_2 hybrid battery. The anolyte and catholyte are distinguished by a middle chamber sandwiched with a cation exchange membrane (CEM) and an anion exchange membrane (AEM). K^+ and SO_4^{2-} released from conversion between Zn and $Zn(OH)_4^{2-}$, and between PbO_2 and $PbSO_4$ merge to K_2SO_4 as the pH buffer. Concentrated OH^- and H^+ in the anolyte and catholyte suppress the HER and OER. This conjugate effectively elevates the operation voltage to 2.95 V (with an open circuit voltage of 3.09 V, as shown in Figure 10b), gathering a high energy density of 252.39 Wh kg^{-1}.[140] By consciously choosing redox couples, the decoupled design can be simplified by using a single ion exchange membrane. As shown in Figure 10c, Yang et al. used the metal hydride (MH) and MnO_2 as the anode and cathode (hydride|CEM|MnO_2), respectively. The $MnCl_2$ solution and KOH solution serve as the catholyte and anolyte, correspondingly, to supply sources of Mn^{2+}/MnO_2 and M/MH conversions. According to the cyclic voltammetry (CV) measurement (Figure 10d), the potential difference of this redox couple is 2.01 V, reflecting the first discharge plateau at around 2.0 V. Because of the proton transportation delay, another plateau happens at 1.4 V, much lower than the first one. Consequently, a discharge capacity of 259.6 mAh g^{-1} at 40 mA g^{-1} with negligible capacity fading in 130 cycles is achieved. Furthermore, a capacity of 164.7 mAh g^{-1} is still maintained when the current density was increased to 1280 mA g^{-1}, confirming a superior rate performance of this decoupled system.[141] Besides membranes with single ion selectivity, the bipolar membrane (Zn|BPM|MnO_2) can also separate the acid/alkaline redox (Figure 10e) to provide an ESW wider than 2.35 V (Figure 10f).[142]

The adoption of asymmetric electrolytes and redox couples with a high potential difference makes the capacity unprecedented if the calculation is based on the mass/volume of active materials. However, the introduction of additional electrolytes brings challenges to the traditional compact design. For asymmetric electrolytes, the pollution between them cannot be avoided, resulting in fast degradation. Thus, in these publications, H-type cells instead of coin or pouch cells were utilized for a stable operation. The relatively commodious distance retard the mixing of electrolytes and the large chamber delay the loss of efficacy of electrolytes. Consequently, the extra electrolyte and container significantly increase the volume and the mass of the whole system. Especially for those double membrane designs, the third chamber makes the battery furtherly redundant. Therefore, besides improved active materials-based energy density, the evaluation of decoupling designs should be careful about the overestimation once they are viewed in the systematic level.

These ESW-extended strategies contribute to gratifying energy density, but the elevation is still capped because of the lack of compatible high-voltage and high-capacity cathodes. At the same time, once the high voltage of a cathode is confirmed, a conservative testing voltage range is still chosen because they still employ unmodified electrolytes for cycling. Therefore, during the development of high-voltage cathodes, attempts with reported ESW-wide electrolyte should be utilized collaboratively to explore the full potential. Thus, the conjugated advancement of high voltage electrode–electrolyte couples is imperative for converting the superfluous ESW into practical energy density.

4. High-Energy-Density AZIBs via Optimized Anodes

Energy density evaluation is typically based on the mass of cathode materials for the current stage. Nevertheless, the mass/volume of anodes, separators, and electrolytes are usually neglected, causing the disregardful assessment of the systematic energy density. Therefore, the elevation of practical energy density should come from the synergetic contribution from the boosting energy output and reduction of excessive mass/volume. In Sections 2 and 3, the evolution of energy output can be achieved through elevating the capacity and voltage through optimizing the cathode and ESW of electrolytes. The following step should focus on reducing system downsizing by trimming overabundant components.

Especially for the zinc anode, it is usually mass-intensive. During the cycling, the reversibility of zinc plating/stripping is not

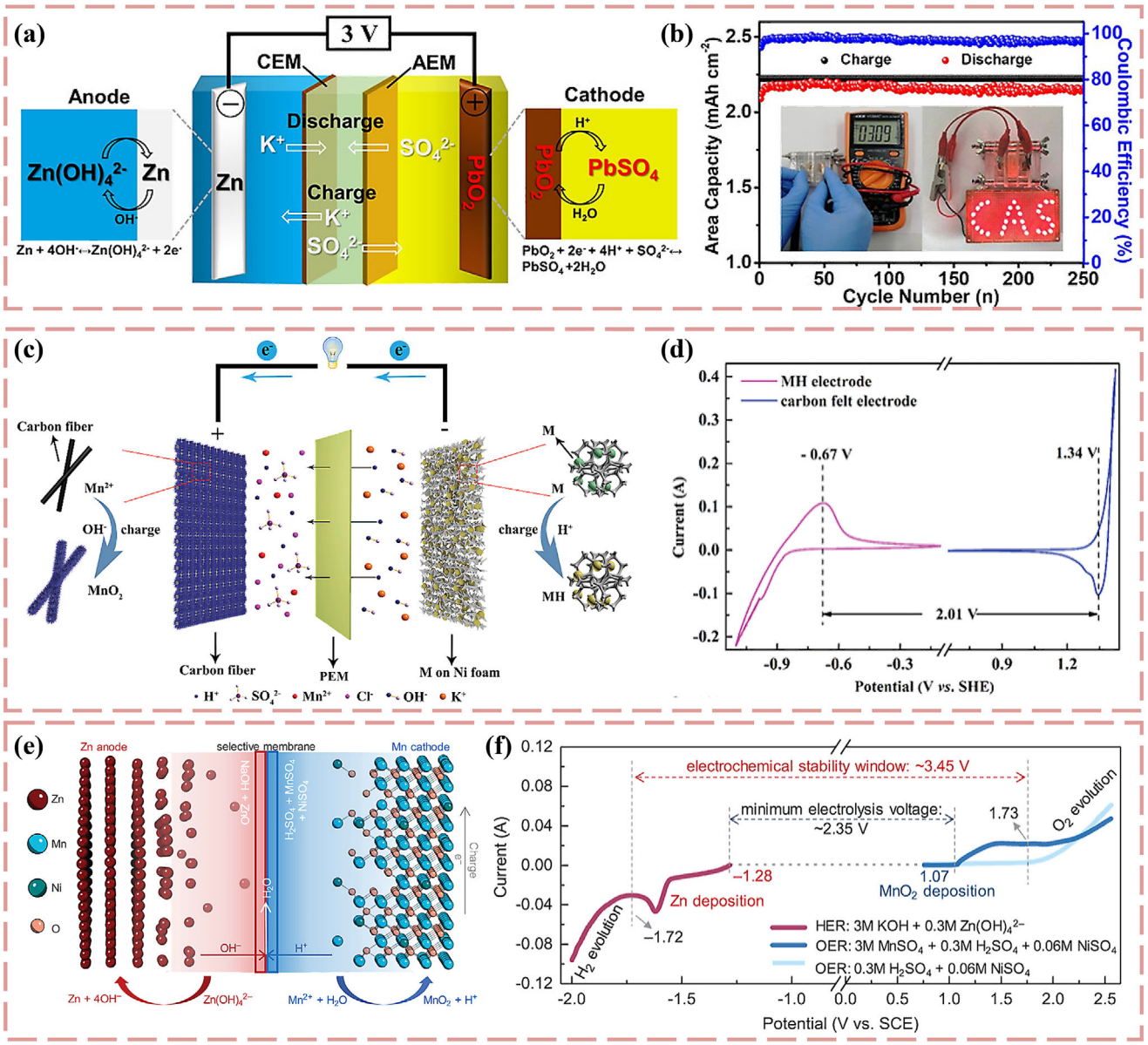

Figure 10. Decoupling configurations exhibiting high working voltages. a) The working mechanism of Zn-PbO_2 battery. b) Cycling stability of Zn-PbO_2 battery at 20 mA cm^{-2}, insets shown open-circuit voltage. a,b) Reproduced with permission.[140] Copyright 2020, Wiley-VCH. c) The working mechanism of Mn-MH battery. d) CV curves of the anodic and cathodic reactions. c,d) Reproduced with permission.[141] Copyright 2020, Wiley-VCH. e) The working mechanism of Zn-Mn hybrid battery. f) LSV curve of the Zn-Mn hybrid battery. e,f) Reproduced with permission.[142] Copyright 2020, Wiley-VCH.

ideal, deteriorating the utilization efficiency of zinc. Issues related to the zinc anode can be divided into two clusters: dendrite formation and parasitic reactions.[143] Specifically, the employment of mild acidic electrolyte causes unstoppable chemical hydrogen evolution, continuously corrodes the zinc surface. Meanwhile, because the voltage of operation unavoidably exceeds the electrochemical stability window of water electrolysis for some time, once extra electric loads are applied, the electrochemical hydrogen evolution reaction happens. Both processes consume protons, leaving locally concentrated OH^-, which reacts with zinc to form an insulating passivation layer. Original defects during zinc plate manufacturing, uneven surface after corrosion, and insulating layer caused by passivation function together to make the local electric field uneven, causing the interfacial aggregation of Zn^{2+}. As a result, the rampant dendrite growth happens, and the protrusions will worsen the electric field uniformity because of "tip effects".[144] To compensate for the loss of active zinc, an extremely excessive supply of zinc becomes necessary. Currently, the zinc foil, regular in the lab, commonly obtains poor zinc utilization efficiency less than 5%, so the zinc anode is even the most deteriorating factor for the system energy density. Accordingly, techniques including zinc-lean, anode-free, and "rocking chair" cells are prospective for holistic energy density refinement in AZIBs (**Table 5**).

Table 5. Performance of zinc metal lean/free anodes.

Strategies	Anode	Zinc amount	Electrolyte	DoD lifespan [h]	Cathode	N/P ratio	Capacity [mAh g^{-1}]	Refs.
Ultrathin Zn foil	ZIF-8@GO@Zn	24 µm	2 M $ZnSO_4$	560 at 42.7%	MnO_2	–	≈210	[181]
	NOC@Zn	≈10 µm	2 M $ZnSO_4$	136 at 52.3%	$KV_{12}O_{30-y}$	4.5	≈180	[182]
	Zn@Cd	≈11.5/21.5 µm	2 M $ZnSO_4$	130 at 85%	MnO_2	1.7	292	[149]
	Zn(002)@ZPO	≈20/30 µm	2 M $ZnSO_4$	500 at 68%	MnO_2	2.4	4.66 mAh cm^{-2}	[154]
	Electro-deposited zinc foil	17.1–21.6 µm	3 M $ZnSO_4$	100 at 46.2%	$V_{10}O_{24}$	–	512.4	[153]
	Accumulative roll bonding-treated Zn foil	Down to 10 µm	2 M $ZnSO_4$	–	NaV_3O_8	5	≈1.5 mAh cm^{-2}	[146]
	Fast-melting solidification-treated Zn foil	30 µm	2 M $ZnSO_4$	180 at 75%	MnO_2	–	≈200	[147]
Electrolyte optimization	Commercial Zn foil	10 µm	1 M $Zn(CF_3SO_3)_2$+50 mg mL^{-1} dextran	150 at 51%	V_2O_5	2.18	≈260	[145]
	Commercial Zn foil	6/22 µm	2 M $Zn(ClO_4)_2$ in PMCNA	420 at 90%	PANi	2.6	≈1.67 mAh cm^{-2}	[150]
	Commercial Zn foil	10/20 µm	2 M $ZnSO_4$+0.1 wt% N, S-CDs	250 at 67%	NaV_3O_8	1.05	3.38 mAh cm^{-2}	[151]
	Commercial Zn foil	10/100 µm	2 M $ZnSO_4$+1 g L^{-1} sulfanilamide	180 at 64%	V_2O_5	5.3	195.3	[152]
Zn metal-free current collector	CF-Cu	5 mAh cm^{-2}	2 M $ZnSO_4$	800 at 50%	MnO_2	–	≈200	[156a]
	$(C_2F_4)_n$-C@Cu	24 µm	2 M $ZnSO_4$	800 at 40%	CNT/MnO_2	–	≈150	[157]
	Cu@AOF	14 µm	3 M $Zn(CF_3SO_3)_2$	–	$Zn_{0.5}VO_2$	AF	203	[156b]
	CuNWs	20 mAh cm^{-2}	2 M $ZnSO_4$	180 at 24%	$Mn_{0.25}V_2O_5$	–	308.3	[158]
	Cu_5Zn_8@NC	6 mAh cm^{-2}	2 M $ZnSO_4$	7000 at 16.7%	V_2O_5	–	288.2	[159a]
	PAN-derived CNFs	5 mAh cm^{-2}	2 M $ZnSO_4$	60 at 60%	V_2O_5	2.4	133.4	[160]
	Cu NBs@NCFs	8 mAh cm^{-2}	2 M $ZnSO_4$	250 at 25%	Mn_2O_3-$ZnMn_2O_4$	–	247.8	[161]
	Cu/Zn-N/P-CMFs	12 mAh cm^{-2}	2 M $ZnSO_4$	400 at 41.7%	MnO_2	4.18	117.3	[162]
	Sn@NHCF	12 mAh cm^{-2}	2 M $ZnSO_4$	100 at 50%	V_2O_5	–	236.4	[163b]
	PCFs	10 mAh cm^{-2}	1 M $ZnSO_4$	250 at 50%	MnO_2	–	288.7	[164]
	3DGs	10 mAh cm^{-2}	2 M $ZnSO_4$	1100 at 10%	V_2O_5	1.74	2.26 mAh cm^{-2}	[165]
Zn powder anodes	Zn-P@Sn-Cu	8 mg cm^{-2}	2 M $ZnSO_4$	–	MnO_2	1.43	72	[166]
	Zn-NC	1.3 mg cm^{-2}	2 M $Zn(CF_3SO_3)_2$ in PVA gel	–	MnO_2	–	≈150	[167a]
	Zn_G	2–3 mg cm^{-2}	2 M $ZnSO_4$	180 at 15%	MnO_2	3	131	[167b]
	Zn-P@In on Sn foil	≈1.75 mg cm^{-2}	2 M $ZnSO_4$	–	MnO_2	–	128.5	[168]
	SLA	20 mg cm^{-2}	2 M $Zn(ClO_4)_2$	450 at 31.3%	$Cu_xV_2O_5$	5	~320	[169]

Techniques to reach these designs can be categorized into the modification of anodic materials and the optimization of electrolytes. Requirement is analogous to anodic materials for electrolytes. For anodic materials, corrosion resistance and the uniform deposition morphology are achieved by adopting suitable structures and materials, and for electrolytes, functional matrixes containing additives, cosolvents, or gel skeleton, etc., are used.

4.1. Zinc-Lean Anodes

Zinc-lean anodes refer to ultrathin zinc foils, anodes with the deposited zinc layer, and quantity-limited zinc powder anodes. They all reduce the system's mass by abandoning excessive zinc, encouraging systematic energy density elevation.

4.1.1. Ultrathin Zinc Anodes

Zinc foils are still the most universally applied, but commercial zinc plates are too thick (0.1 mm), leaving underlying zinc inactive. For a common anode with a 12 mm diameter, the anode weight reached 75 mg with an areal capacity of 58.55 mAh cm^{-2}, meaning a depth of discharge (DoD) less than 8.5% at 5 mA cm^{-2}. Thus, notices have been put on tapering zinc foils to avoid this grievous zinc waste.

Compared to thick zinc foils, the zinc depletion issue becomes more severe once the thickness is reduced, illustrating more challenging working conditions. Therefore, assistance with superior reversibility and parasitic reaction suppression from protective coatings, optimized electrolytes, or deposition direction-selective zinc becomes more crucial. Metals, oxides, nitrides, carbons, MOFs, and polymers have all been widely employed as ex

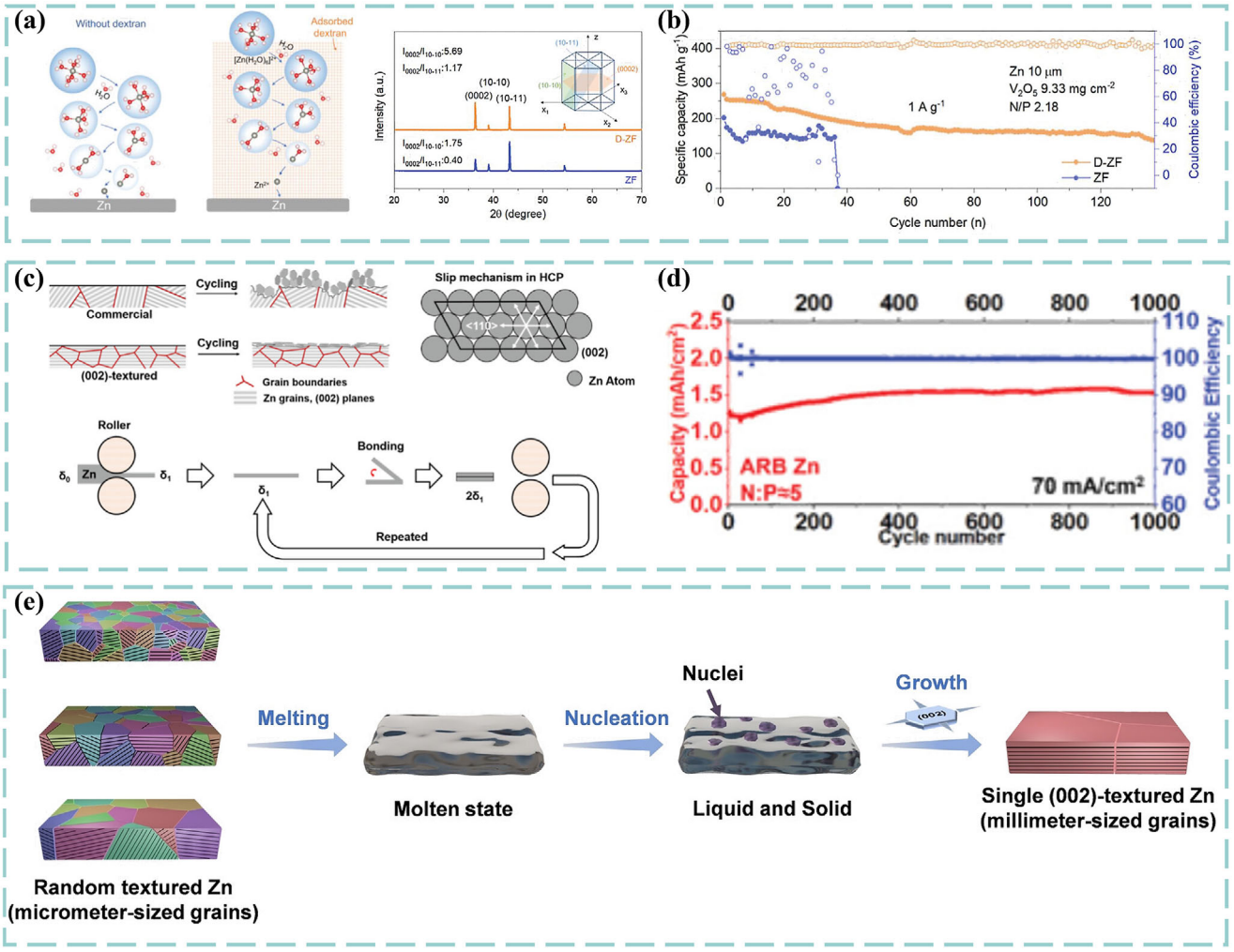

Figure 11. Strategies to achieve stable zinc anode with ultrathin zinc foils. a) Schematic illustration of desolvation process in $Zn(OTf)_2$ electrolyte without and with dextran additive, and XRD profiles of Zn anodes after cycling with different electrolytes. b) Cycling stability of Zn||V_2O_5 battery at 1 A g^{-1} with different electrolytes. a,b) Reproduced with permission.[145] Copyright 2023, Wiley-VCH. c) Grains in commercial and treated Zn foils, slip mechanism for HCP metals, and the mechanism of the accumulative roll bonding process. d) Cycling stability of Zn||NVO battery at the N/P ratio of 5. c,d) Reproduced with permission.[146] Copyright 2021, Wiley-VCH. e) Schematic illustration of the fabrication process of (002)-textured Zn through melting-solidification. e) Reproduced with permission.[147] Copyright 2024, Wiley-VCH.

situ protective layers.[148] These layers isolate the electrode from the electrolyte, homogenize the electric field, or derive the uniform Zn^{2+} flux. As an example, Gan et al. cast the zeolitic imidazolate framework-8 (ZIF-8) in situ grown on GO (ZIF-8@GO) on the ultrathin zinc foil (20 μm) with polyvinylidene fluoride (PVDF) as the binder, fabricating the slim anode with an overall thickness of 24 μm. The inertness of this layer successfully prevents corrosion, and the strong adhesion between ZIF-8 and Zn^{2+} facilitates the Zn^{2+} transportation, guaranteeing superb reversibility. Some other layers are not exerted on ultrathin foils directly, but the decent stability at a low N/P ratio confirms their effectiveness under zinc-lean conditions. For example, Lv et al. cast Cd metal on the zinc foil through the displacement reaction, and a 10 μm Cd@Zn plate was used in Cd@Zn||MnO_2 battery, corresponding to an extremely low N/P ratio of 1.7, to deliver a high areal capacity of 3.5 mAh cm^{-2} (292 mAh g^{-1}).[149]

Electrolyte optimization also benefits the stability at the low N/P ratio, encouraging ultrathin zinc application. Currently, additives like 2-methacryloyloxyethyl phosphorylcholine and *N*-acryloyl glycinamide,[150] carbon quantum dots,[151] binaphthyl sulfonamide,[152] etc., have been confirmed effective with limited zinc supply primarily due to SEI formation. For example, dextran is reported as a multifunctional additive with a limited concentration. As illustrated in **Figure 11a**, dextran molecules can reshape the solvation sheath by replacing water, and the preferred adsorption of dextran on the Zn(002) plane facilitates the protective layer formation and fastens the nucleation and growth of Zn(002). The dextran-added electrolyte exhibits a capacity above 270 mAh g^{-1} at the low N/P ratio of 2.18 using a 10 μm zinc foil anode and a V_2O_5 cathode (Figure 11b).[145] Of particular note, electrolyte tuning brings holistic advancement, so refined electrolytes mentioned in the above sections may also be beneficial with ultrathin zinc.

Zinc foils with pronounced Zn(002) textures also promote reversibility due to chosen lateral depositions, confirming the potential to reduce the thickness. Li et al. reported the intimate correlation between the plane's preference and the amount of deposited zinc by showing universal Zn(002) planes with 10 mAh cm^{-2} zinc sedimentation and a decreasing trend with the increased amount. The as-prepared 17.1 µm (10 mAh cm^{-2}) zinc anode demonstrates a discharge capacity of 512.5 mAh g^{-1} in the Zn||$V_{10}O_{24}$ battery with decent stability.[153] However, the scalable production of ultrathin zinc still relies on mechanical manufacturing for the complexity of electro-deposition. For example, Zheng et al. employed the cold rolling method to introduce the repeated plastic deformation on zinc foils to fabricate zinc foils with a thickness of less than 10 µm and an extensive Zn(002) (Figure 11c). By coupling with the NaV_3O_8, an areal capacity of 1.5 mAh cm^{-2} at the low N/P ratio of 5 is realized (Figure 11d).[146] Up to now, other treatments like the melting-solidification approach (Figure 11e) and the annealing treatment have also been offered to elevate the utilization efficiency of zinc.[147,154]

4.1.2. Substrates for Zinc Deposition

Proper substrates for the zinc anode obtain electronic conductivity, suitable chemical stability, and reasonable mechanical stability, so metals and carbons are primarily applied. Similar to zinc foils, those commercialized metal foils face the issue of uneven electric field distribution caused by the microscopic defects on the surface. Thus, surface optimization through functional materials pavement or nanostructure fabrication is inevitable before the actual application. Among them, the commercial Cu foil excels for its favorable adhesion with Zn^{2+} and cost-effectiveness.[155] Currently, functional carbons, zincophilic composites, and zincophilic metal particles have been cast to encourage uniform deposition on the Cu foil with the controllable zinc utilization efficiency.[156] For example, by direct pyrolysis of polytetrafluoroethylene (PTFE) powders under vacuum conditions, Li et al. successfully deposited the hydrophobic fluorinated carbon on the copper foil ($(C_2F_4)_n$-C@Cu) as the anode current collector (**Figure 12a**). After predepositing 5 mAh zinc (≈8.5 µm), the thickness of the prepared anode is about 24 µm (Figure 12b), which delivers both reduced volume and mass compared with commercial 100 µm zinc foils. With the facilitated Zn^{2+} transportation and lower nucleation barrier, this composite anode presents a capacity of about 150 mAh g^{-1} with the V_2O_5 cathode at 0.2 A g^{-1} (Figure 12c). More importantly, a favorable areal capacity of about 0.15 mAh cm^{-2} can still be kept when the N/P ratio is further reduced to 3.33 (Figure 12d).[157] Other than surface decoration, morphology adjustment also benefits anode reversibility for larger electrochemically active areas and exposure of more zincophilic planes. The copper nanowire substrate (CuNWs) with Cu(111) facets at the ridges has been proved to facilitate the epitaxial deposition because of moderate interfacial energy between Cu(111) and Zn(002). As a consequence, the 20 mAh cm^{-2} composite zinc anode delivers the capacity of 308.3 mAh g^{-1} with the $Mn_{0.25}V_2O_5$ cathode.[158]

Enlargement from microscopic morphologies is still finite, so many 3D formulas were proposed to pursue massive specific active areas. The overpotential can be effectively reduced with saturated ion pathways and flourishing nucleation positions, and the coulombic efficiency (CE) is boosted. Commercial metal foams like Ni-foams and Cu-foams have been implemented, but chaotic deposition still happened on these pristine substrates, demonstrating the significance of decoration. As its planar counterparts, the copper foams can also be enveloped by functional materials like CF@C@Ti$(OH)_4$, or morphologies with better zinc adhesion like Cu_5Zn_8 nanorods. With their porous structures, specific discharge capacities can reach 297.7 and 288.2 mAh g^{-1}, respectively.[159]

The carbon matrix is also engaging, and its superior low density makes it a better candidate for high-energy-density applications. The 3D carbon framework can be fabricated by direct pyrolysis of porous polymers, and polyacrylonitrile (PAN) is frequently used for the convenient construction of 3D structures by electrospinning. The primal PAN-based carbon nanofiber only takes part about 17.5–19.7 wt% of the anode when 5 mAh cm^{-2} zinc was imposed, and even under harsh conditions (N/P = 2.4), the Zn@CNF||V_2O_5 battery allows discharge capacity of 133.4 mAh g^{-1}.[160] The PAN carbon can be further empowered by spinning functional materials in precursors before carbonization. Zeng et al. reported the CuS NBs@NCFs substrate by calcining CuS nanoboxes (CuS NBs) embedded PAN fibers. The porous structure homogenizes local current densities, and the zincophilic Cu and Cu-Zn alloy provide more adhesive nucleation sites. Combining these two merits, the initial capacity of full cells coupled with the MnO_2 cathode reached 192.8 mAh g^{-1}.[161] In Zeng's subsequent work, the capacity even exceeds 200 mAh g^{-1} through additional tannic acid-treated CuZn nanocubes trimming. With a high DoD of 41.7% and a low N/P ratio of 2.9, both substrates are unburdened from excessive zinc metal.[162] Besides, fillers or surface crafters for PAN carbon fiber can also be chosen from metal oxides, MOFs, or other carbonized polymers.[125,163] Meanwhile, 3D carbon frames derived from other polymer fibers like PVA have also been investigated.[164]

More inspiringly, the refinement of the 3D-print technique liberates the construction of the 3D carbon framework from carbonization. As the pioneer, Wu et al. created the graphene array tube and pillar structures (3DGT and 3DGP, respectively) via digital light processing (DLP) (Figure 12e). Both designs present the columnar array structure (Figure 12f), allowing zinc deposition on the inner surfaces of cylinders to avoid separator penetration. Attributed to the precise control of zinc amount, a capacity of about 220 mAh g^{-1} with the N/P ratio of 9.8 is exhibited in 3DGT@Zn||V_2O_5 coin cells (Figure 12g). More encouragingly, the ultralow N/P ratio of 1.74 with a capacity of 431.5 mAh g^{-1} is realized in the 3DGT@Zn||V_2O_5 pouch cells (Figure 12h), confirming the acceptable scalability of 3D printing technique.[165]

4.1.3. Zinc Powder Composite Anodes

Powder-based electrodes are also preferred for the high energy density demand due to the precisely controlled zinc supply and the large specific surface area. However, zinc powders cannot be used as electrodes directly because of the lack of continuity. Currently, four regular techniques for molding zinc powder

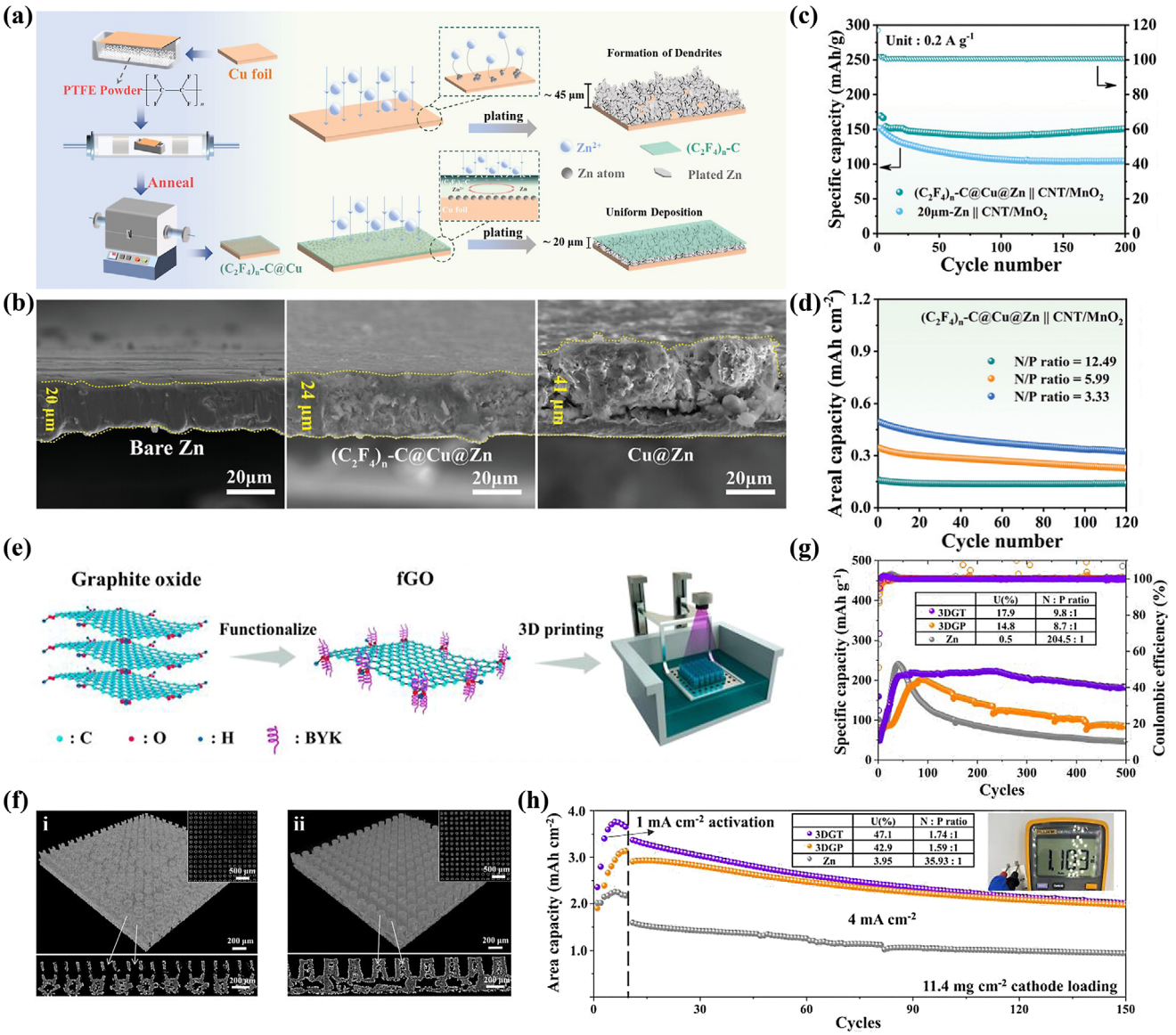

Figure 12. Current collectors for zinc-lean anodes. a) The schematic illustration of the fabrication process of $(C_2F_4)_n$-C@Cu. b) SEM images of cross-sections of commercial Zn foil, 5 mAh cm^{-2} Zn deposited on $(C_2F_4)_n$-C@Cu and Cu foil. Cycling stability of $(C_2F_4)_n$-C@Cu@Zn||CNT/MnO_2 battery c) at 0.2 A g^{-1}, and d) with different N/P ratios. a–d) Reproduced with permission.[157] Copyright 2023, Wiley-VCH. e) Schematic illustration of DLP process for fabricating 3D graphene arrays. f) Micro-CT images of i. 3DGT and ii. 3DGP. Cycling stability of Zn||V_2O_5 batteries in g) coin cells and h) pouch cells with different 3D anodes. e–h) Reproduced with permission.[165] Copyright 2023, Elsevier.

composites are slurry casting, mechanical grinding and rolling, casting and demolding, and 3D printing. Before molding, zinc powder should be mixed with conductive agents and binders (some binders-free designs have been proposed) to form the ink. However, simple aggregation of zinc particles causes loose contact, leading to poor electronic conductivity and dead zinc issues. Furthermore, expanded contact areas intensify corrosion and passivation. Therefore, supplementing electron/ions consistency and stabilizing the zinc are top priorities for powder-based anodes.

Chemically inert, zincophilic, and conductive substrates can achieve these two goals. For example, Li et al. cast zinc powder on the Sn-doped Cu foil denoted as Zn-P@Cu to reach a capacity of 200 mAh g^{-1} with a low N/P ratio equal to 10:7.[166] Compared to this mechanical contact with the sharp border, direct grafting or mixing zinc powders with corrosion-resistive and conductive materials like functional carbon graphene, and MXenes can further improve the stability and continuity.[167] As an example, Li et al. wrapped zinc powder with a uniform In layer through the replacement reaction (**Figure 13a**). Chemically inert In metal suppresses parasitic reactions while reserving outstanding electronic conductivity. As a result, the fabricated full battery exhibits a specific discharge capacity of 271.3 mAh g^{-1} at 0.2 A^{-1} with the MnO_2 cathode (Figure 13b).[168]

As long as uninterrupted conductivity is established through zinc powders and conductive agents, the zinc powder

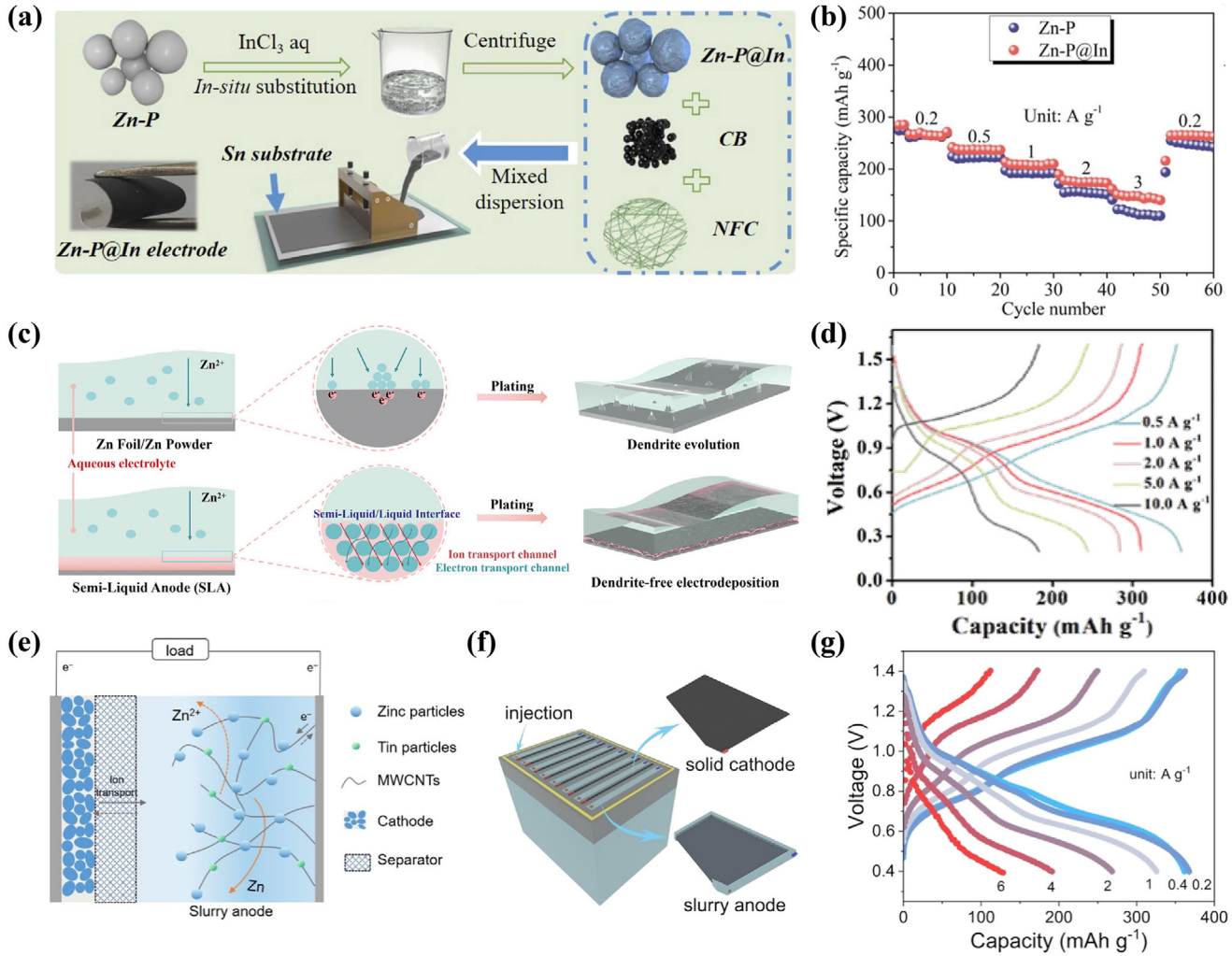

Figure 13. Zinc powder composite anodes. a) Schematic illustration of the preparation of Zn-P @ In anodes. b) Rate performance of Zn||MnO_2 battery with Zn-P anodes and Zn-P@In anodes. a,b) Reproduced with permission.[168] Copyright 2023, Elsevier. c) Schematic illustration of deposition behavior of commercial Zn foil/powder anodes and SLA anodes. d) Voltage profiles of SLA||$Cu_xV_2O_5$ battery showing the rate performance. c,d) Reproduced with permission.[169] Copyright 2022, Wiley-VCH. Schemes of e) working principle and f) stack of full batteries using semisolid slurry anode. g) Voltage profiles of Zn-Sn-S||$NH_4V_4O_{10}$ battery showing the rate performance. e–g) Reproduced with permission.[170] Copyright 2022, Wiley-VCH.

composite is not restricted to the solid form, and substrates can even be abandoned. Based on this philosophy, all-in-one electrodes are derived from hydrogels. Zinc powders and conductive carbons are homogeneously dispersed in precursors, ensuring ionic and electronic conductivities after the polymerization. Trailblazing works were reported by Liu et al. and Yang et al. in the same year. Liu et al. fabricated the PEG-400-based semiliquid anode (SLA) through polymerization of PEG hydrogel containing carbon and zinc powders. The local stress is appropriately released due to the outstanding rheological property in this quasisolid (Figure 13c), contributing to a high discharge capacity of 378 mAh g^{-1} in the SLA||$Cu_xV_2O_5$ cell (Figure 13d).[169] Yang et al. even abandoned the thorough polymerization and directly used the semisolid slurry (Zn-S) as the anode (Figure 13e,f). After finely tuning the zincophilicity with Sn powders, the Zn-Sn-S||NVO batteries reach a remarkably high capacity of 361 mAh g^{-1} at 0.2 A g^{-1} (Figure 13g).[170]

4.2. Anode-Free Zinc-Ion Batteries

The anode-free zinc-ion battery (AF ZIBs) is a more radical design by exhaustively abandoning zinc metal. Instead, a bare current collector is used at the anode side. After being fully discharged, all Zn^{2+} is extracted from the cathode and deposited on the anode current collector during the charging, obtaining a DoD of 100%. The zinc reservoir is even lower than those zinc-lean designs, so the demand for improving the reversibility of stripping/plating is more severe. Like anode protection strategies in common AZIBs, the AF ZIBS can reach stable operation through the electrode (current collector) and electrolyte engineering.

4.2.1. Current Collector Engineering

Substrates for deposited zinc anodes also inspire the design of an anode-free current collector, so functional coating, the alloy

composition, and the 3D framework become typical for substrate design.

Even though protective layers have been comprehensively explored on the zinc metal anode, the special operation mode in AF ZIBs places extra demands on the layer. First, a much lower concentration of Zn^{2+} requests more superlative electronic and ionic conductivities, thus excluding multiple inert materials. Second, the layer should present an acceptable elasticity. Spaces left during the stripping of zinc foil cannot be applied to the AF current collector, so the stress will be exerted on the layer directly; as a result, the unfavorable ductility and mechanical strength cause the membrane to break. Third, adhesive forces between the layer, Zn, and current collectors should all be robust to avoid layer detachment. To our knowledge, Zhu et al. reported the first anode-free Zn||MnO_2 battery by casting commercial carbon nanodiscs on Cu foils as the anode. Owing to the more homogeneous deposition derived from the uniform electric field, the stability is comparable to zinc foils, and the Zn||MnO_2 battery can reach an energy density of 135 Wh kg^{-1}.[171] Influenced by Zhu's work, subsequent composite carbon materials with elaborate zinc adhesion designs became popular. In their midst, MXenes stand out for their hydrophilicity, extraordinary electronic conductivity, and superior ion adsorption eligibility. For example, Yang et al. coated the $Ti_3C_2T_x$ MXenes/nanocellulose slurry on stainless steel to exhibit a discharge capacity of 212 mAh g^{-1} with the NVO cathode.[172]

Alloys-covered current collectors also provide sufficient reversibility by involving metals binding well with Zn^{2+} (Sb, Sn, Cu, etc.).[173] These alloy layers are intensely attached to the substrate, avoiding detachment. For example, Zheng et al. constructed the Sb/Sb_2Zn_3 alloy on the Cu foil by depositing Sb first and generating the in situ Sb_2Zn_3 in the following cycles (**Figure 14a**). The zincophilic Sb brings stronger adsorption of Zn^{2+} and the homogenized electric field. With the improved zinc reversibility, the stable operation of the fabricated anode-free Zn-Br_2 battery becomes feasible (Figure 14b). As shown in Figure 14c, when discharged at 1 C, the superior areal capacity of 10 mAh cm^{-2} is exhibited. Moreover, the capacity does not degrade within 800 cycles (Figure 14d), and a final energy density of 274 Wh kg^{-1} is recorded.[174]

Attempts to fabricate a 3D current collector have also been executed to remove constraints of 2D structures. Like the advantages mentioned in the above sections, grown nucleation sites, saturated Zn^{2+} flux, and homogeneous electric fields in 3D frameworks promote uniform deposition and reversibility. As the current collector, rich voids also tolerate more drastic volume variation. For example, Xu et al. fabricated an anode-free Zn-Br_2 by using 3D nanoCu substrates for zinc plating/stripping (Figure 14e). They used the carbon thermal shock method to cast Sn on 3D Cu nanowire frames prepared by calcination treatment with the NaOH solution (denoted as ZA@3D-nanoCu) (Figure 14f). As a result, an areal capacity of 10 mAh cm^{-2} can be realized in the ZA@3D-nanoCu-Br_2 battery with an excellent rate performance attributed to pleasant reversibility of Zn/Zn^{2+} and $TPABr_3/Br^-$ redoxes (Figure 14g,h).[175] Other techniques like in-situ 3D construction through oxidation/reduction, synthesis of conductive aerogel, and dispersing 3D frameworks on an acceptor have also provided favorable 3D current collectors for AF ZIBs.[176]

4.2.2. Electrolyte Engineering

The reconstruction of the electrode/electrolyte interface in AF ZIBs can also be achieved through electrolyte engineering, majorly derived from solvation structure adjustment and surface adsorption. Among vast perfected electrolytes, only those presenting both high first-cycle and average CEs are promising in AF ZIBs for their maximum zinc utilization efficiency.

Comparing these two routines, electrolytes allowing SEI formation through surface adsorption show a more encouraging performance, and the F-containing SEI takes the lead in anode-free designs. Up to now, multiple F-rich zinc salts like $Zn(OTf)_2$, and additives like trimethylethyl ammonium trifluoromethanesulfonate (Me_3EtNOTF), hexafluoroisopropanol, ZnF_2, etc., have demonstrated potentials building SEI facilitating the anode-free operation.[177] Among them, the C, S, and F elements-rich Me_3EtNOTF can even construct a remarkably robust and component-rich SEI containing ZnF_2, $ZnCO_3$, and $ZnSO_3$ and ensure the operation of the Ti||Zn_xVOPO_4 anode-free pouch cells for more than 100 cycles with an initial discharge capacity reaching 130 mAh g^{-1}.[178] Certainly, some F-free SEIs like $Zn_5(OH)_8Cl_2{\cdot}H_2O$ layer assembled from tetramethylammonium chloride additive have also validated anode-free stability.[179] However, F-rich electrolytes are still the most comprehensive and efficient. Cases of AF ZIBs deduced from water-lean solvation sheath electrolytes are infrequent but not absent. This is because an incomplete substitution of water molecules still results in mitigatory water-induced side reactions, amplified with a limited zinc reservoir. Thus, only those additives raising radical solvation structure reformation like (1-ethyl-3-methylimidazolium chloride) ($EMIm^+$) can support the AF cycling. This cation receptor drastically transforms solvated Zn^{2+} from $Zn(H_2O)_6^{2+}$ into water-free $ZnCl_4^{2-}$, discarding interfacial parasitic reactions. With this unique solvation structure, the fabricated Cu||zincificated PANi (Z-PANi) battery exhibits a stable discharge capacity of 154.4 mAh g^{-1} for over 50 cycles without zinc on the anode.[180]

4.3. "Rocking Chair" Zinc-Ion Batteries

Zinc metal-free anode design can also be achieved through straight utilization of the ionic form of Zn^{2+}. Zinc-ion batteries that intercalate or coordinate Zn^{2+} on both electrodes without Zn metals are named "rocking chair" batteries. Abandoning current collectors accepting the deposition of Zn metal, "rocking chair" batteries use Zn^{2+} host materials as the anode. Zn sources supplied in these cells typically come from Zn^{2+}-insertion anodes or Zn-rich cathodes. Because the capacitances of both electrodes, instead of only the cathode, are limited, the theoretical capacity is lower than that of zinc metal batteries. Still, the specific systematic energy density is promoted without heavy zinc. Other advantages, including prompt charge transport dynamics and dendrite preclusion, make this cluster more charming. Currently, metal oxides, metal sulfides, and organic compounds are three major clusters of anodes applied in "rocking chair" zinc-ion batteries (**Table 6**).

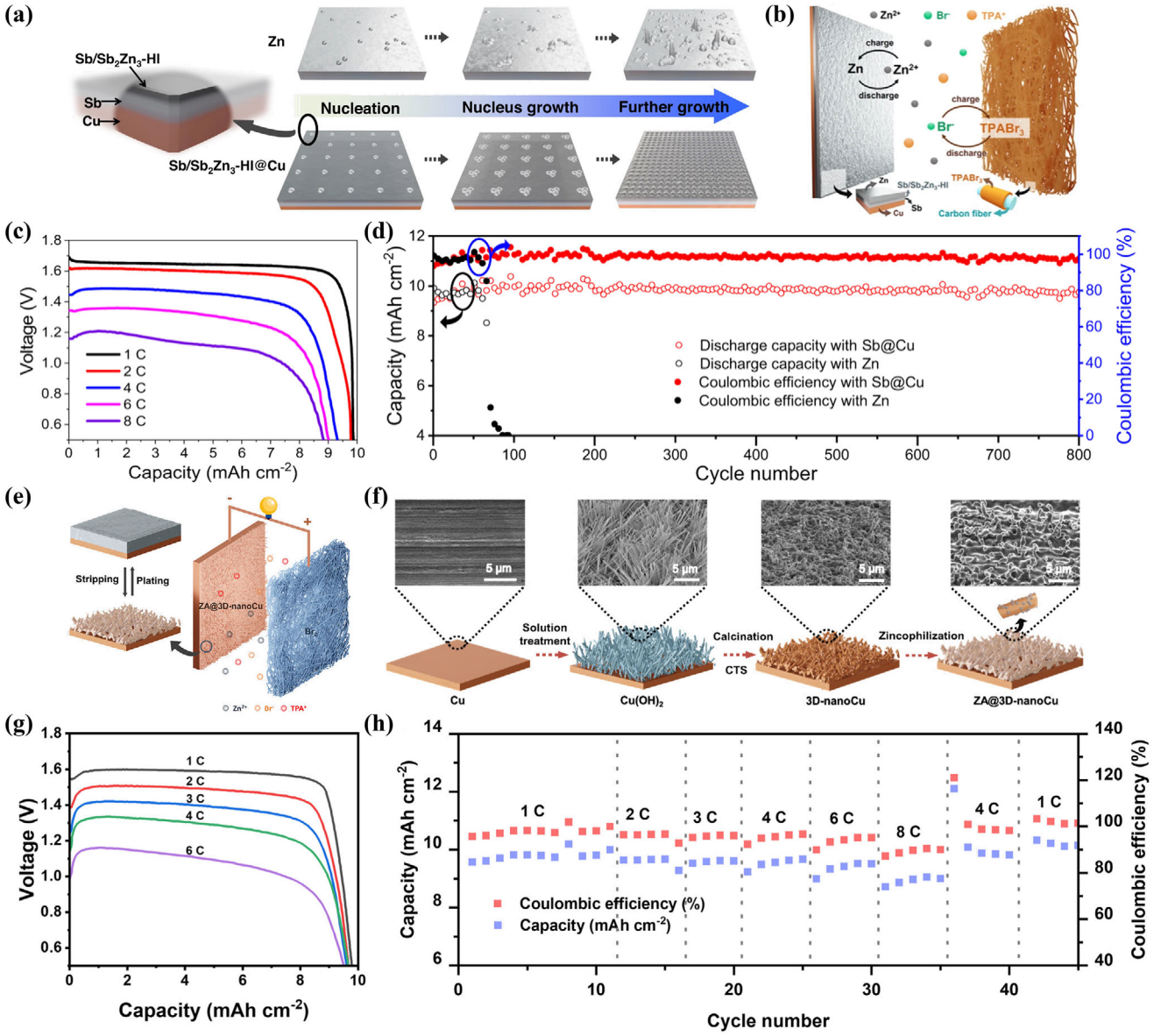

Figure 14. Current collectors for anode-free AZIBs. a) Scheme of Zn deposition behavior on Zn and Sb/Sb_2Zn_3-HI@Cu substrates. b) Schematic illustration of the working mechanism of the anode-free Zn-Br_2 battery. c) Discharge curves of the anode-free Zn||Br_2 battery showing the rate performance. d) Cycling stability at 10 mA cm^{-2}. a–d) Reproduced under the terms of the CC-BY Creative Commons Attribution 4.0 International license.[174] Copyright 2023, X. Zheng et al., published by Springer Nature. e) Schematic illustration of the working mechanism of the ZA@3D-nanoCu||Br_2 battery. f) The preparation procedures of the ZA@3D-nanoCu. g) Discharge curves of the ZA@3D-nanoCu||Br_2 battery and h) the rate performance. e–h) Reproduced with permission.[175] Copyright 2023, Elsevier.

4.3.1. Transition Metal Oxides

Layered oxides have demonstrated effectiveness as Zn^{2+} hosts for cathodes, so they are automatically believed to function well as anodes. Among universal oxides, molybdenum-based ones caught the attention for their inherent multivalent states. Particularly for the MoO_2, its high theoretical capacity (838 mAh g^{-1}), narrow bandgap (≈0.9 eV), and low resistivity (8.8×10^{-5} Ω cm)[202] make it a proper nominee. Furthermore, the unique 1D tunnel, based on its rutile structure, guarantees fast Zn^{2+} transmission.[203] However, the structural benefit cannot be fully showcased because of the non-negligible structure collapse during (de)intercalation. Thus, structure consolidation is the common prerequisite for the practical application of the MoO_2 anode. For example, Wang et al. inserted the nitrogen-doped carbon (MoO_2@NC) to build the laminated structure. As illustrated in **Figure 15a**, they first intercalated aniline into commercial MoO_3, then the calcination was conducted for carbonizing aniline and reducing MoO_3 into MoO_2 simultaneously. Through a series of optical characterizations, the prepared MoO_2@NC samples present a *d*-spacing of 0.342 nm with carbon homogeneously inserted (Figure 15b). The carbon fillers effectively improve the

Table 6. The performance of "rocking chair" zinc-ion batteries.

Types of materials	Anode	Cathode	Electrolyte	Capacity [mAh g^{-1}]	Energy density [Wh kg^{-1}]	Refs.
Transition metal oxides	MoO_2@NC	Zn-$Na_3V_2(PO_4)_2O_2F$	3 M $Zn(CF_3SO_3)_2$+6 M $LiCF_3SO_3$	158	45.1	[183]
	h-MoO_3	$Zn_{0.2}MnO_2$	1 M $ZnSO_4$	56.7	61	[184]
	MoO_3	Ni-PBA	20 M $ZnCl_2$+1 M HCl	68.7		[185]
	MoO_x	$Zn_\delta^-MoO_x$	2 M $Zn(CF_3SO_3)_2$	114.6		[186]
	h-WO_3/3DG	$ZnMn_2O_4$/CB	3 M $Zn(CF_3SO_3)_2$	66.8	73.5	[187]
	WO_3/WC	MnO_2/graphite	2 M $ZnSO_4$	69	85	[188]
	BiOI	Mn_3O_4	2 M $Zn(CF_3SO_3)_2$	149		[186]
Transition metal sulfides	$Na_{0.14}TiS_2$	$ZnMn_2O_4$	2 M $Zn(CF_3SO_3)_2$	105	51	[189]
	MXenes-TiS_2	MWCNTs-VO_2	2 M $ZnSO_4$ PAM hydrogel	129.6		[190]
	CuS@CTMAB	Zn_xMnO_2	2 M $ZnSO_4$	243.3	66	[191]
	CuS-CTAB	$Zn_xFeCo(CN)_6$	3 M $Zn(CF_3SO_3)_2$	225.3		[192]
	$Cu_{2-x}Se$	Zn_xMnO_2	2 M $ZnSO_4$+0.1 M $MnSO_4$	200.5		[193]
	$TiSe_2$	VO_2	2.0 M $ZnSO_4$	44.3	38.1	[194]
	$MoTe_{1.7}$	Zn_xMnO_2	3 M $Zn(CF_3SO_3)_2$+0.2 M $MnSO_4$	338	137	[195]
	$Cu_{2-x}Te$	$Na_3V_2(PO_4)_3$	3 M $Zn(CF_3SO_3)_2$	59	58	[196]
	$TiTe_2$	$Zn_xCo_3O_4$	3.0 M $ZnSO_4$	225	149	[197]
Organic compounds	9,10-Anthraquinone	$ZnMn_2O_4$	1 M $ZnSO_4$+0.05 M $MnSO_4$	190.4	81	[198]
	Naphthalene diimide	KZnHCF	2 M $ZnSO_4$	113.9	50.2	[199]
	perylene-3,4,9,10-tetracarboxylic diimide/RGo	Prussian Blue	3 M $ZnSO_4$	48	44	[200]
	polyimides/CNT	Zn_xMnO_2	1.5 M $Zn(CF_3SO_3)_2$	110	50.5	[201]

conductivity while providing solid support for the structure, ensuring both fast kinetics and favorable stability, reflected by exceptional cycling stability (78 mAh g^{-1}, 93% retention after 200 cycles) and rate performance in MoO_2@NC||Zn-NVPOF batteries (Figure 15c,d).[183] Besides, hexagonal MoO_3 (h-MoO_3), a structurally more stable Mo-based oxide, has also attracted attention. Benefiting from the hexagonal structure, resulting in fast Zn^{2+} migration and diffusion kinetics within these hexagonal channels, cavities, and crystallite boundaries, the outstanding stability and reaction kinetics are realized. Consequently, the specific discharge capacity of 56.7 mAh g^{-1} (corresponding to the energy density of 61 Wh kg^{-1}) is recognized without any degradation for 1000 cycles.[184] Also, Yang et al. maximized benefits from the hexagonal structure by fabricating a novel MoO_3, assembled with double sheets of MoO_6 octahedra, to exhibit a specific capacity of 224.5 mAh g^{-1} in MoO_3||PBA batteries. Noticeably, even though they used zinc-free anodes, excessive Zn^{2+} is still applied in the WiSE. The concentrated 20 M $ZnCl_2$ with 1 M HCl electrolyte indisputably forms another cornerstone for the stable operation.[185] The following researchers continue dedicating themselves to finding the equivalence of Zn^{2+}, and thus, the preintercalated anodes were proposed. Kaveevivitchai et al. first reported $Zn_xMo_{2.5+y}VO_{9+z}$ by microwave-aided preinsertion of Zn^{2+} in the open-tunnel to obtain a reliable capacity of 120 mAh g^{-1}.[204] Additionally, oxides with larger layer space (tungsten-based oxides) or sturdy adhesion with Zn^{2+} (bismuth-based oxides) have also indicated potential in "rocking chair" zinc-ion batteries.[186,187,188]

4.3.2. Transition Metal Sulfides

The layered structure can also be found in transition metal sulfides, making them promising as anodes. At present, the group of $M_xMo_6T_8$ (M: transition metals, T: oxygen excluded stable chalcogens) has received the most comprehensive investigation. Pioneeringly, Chae et al. applied $Zn_2Mo_6S_8$ in AZIBs and identified the two-step intercalation procedure. These double Zn^{2+} occupations provide a total capacity of 134 mAh g^{-1}, and favorable reversibility.[205] Similar to oxides, the expanded layer spacing is also expected for sulfides for the elevated capacity and facilitative Zn^{2+} transition, so Ti-based and Cu-based sulfides, obtaining large layer spaces, were explored. The original layer space of TiS_2 is 5.7874 Å, and it can be further enlarged to 5.8526 Å through presodiation. The pillar-like Na^+ can also improve structural stability while advancing reversibility and electronic conductivity, exhibiting an energy density of 51 Wh kg^{-1} in $Na_{0.14}TiS_2$||$ZnMn_2O_4$ batteries.[189] Potentials of sulfides can be mapped to other chalcogen compounds like $Cu_{2-x}Se$,[193] $TiSe_2$,[194] $Cu_{2-x}Te$,[196] and $TiTe_2$,[197] which have all demonstrated their effectiveness as anode materials, and have been benefited from the layer spacing expansion strategy.

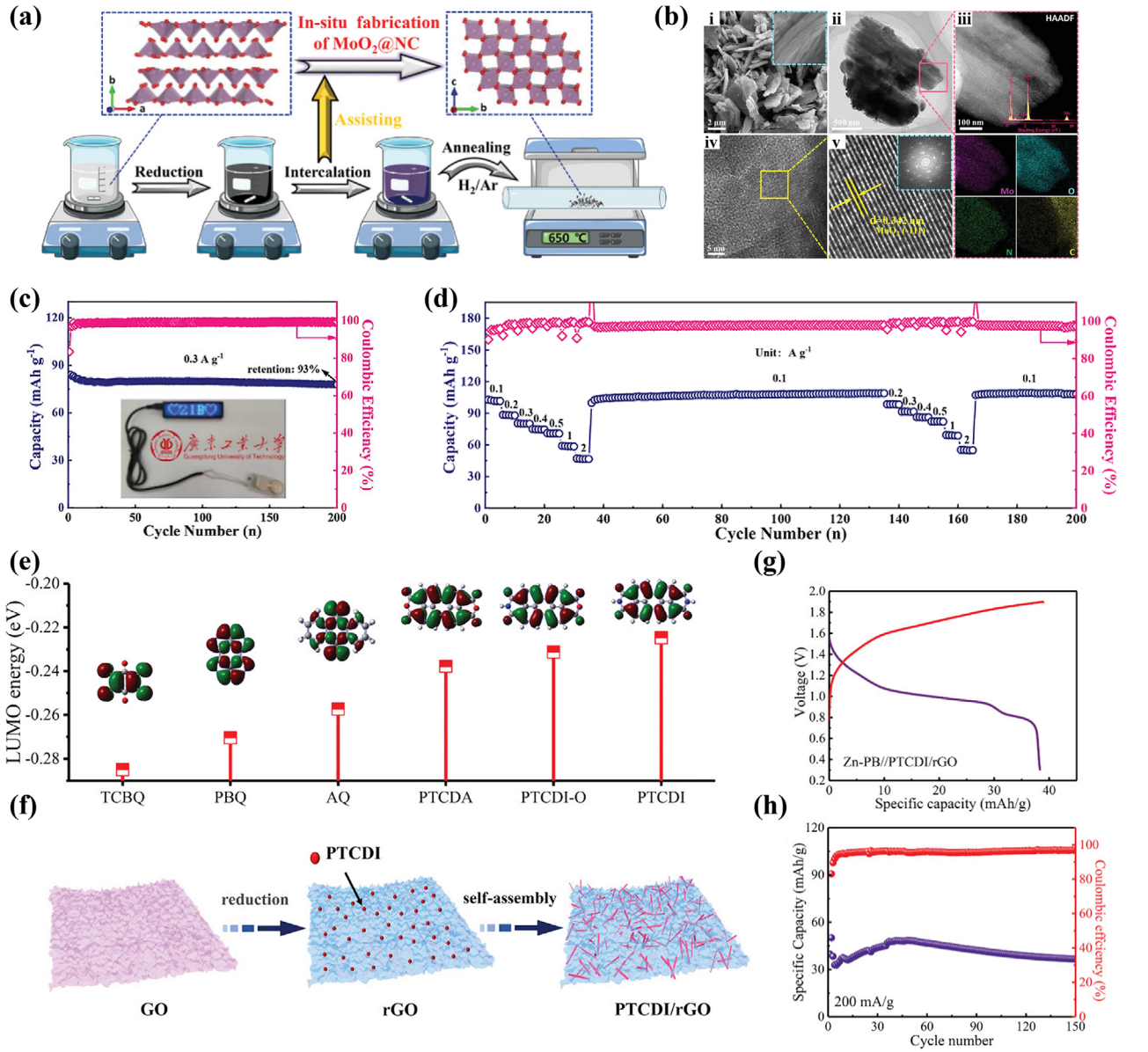

Figure 15. Anodes for "rocking chair" AZIBs. a) Schematic illustration of the in-situ fabrication process of MoO_2@NC. b) (i) SEM image, (ii) TEM image, (iii, iv) HRTEM images, and (v) HAADF-STEM image (with EDX mappings) of MoO_2@NC. c) Cycling stability and d) rate performance of MoO_2@NC||Zn-NVPOF battery. a–d) Reproduced with permission.[183] Copyright 2021, Wiley-VCH. e) LUMO energy levels for different organic compounds. f) Schematic illustration of the fabrication process of PTCDI/rGO. g) Galvanostatic charge and discharge curves and h) cycling stability for Zn-Pb||PTCDI/rGO battery. e–h) Reproduced under the terms of the CC-BY Creative Commons Attribution 4.0 International license.[200] Copyright 2020, N. Liu et al., published by Wiley-VCH.

4.3.3. Organic Compounds

Different from rigid lattices in oxides and sulfides, the lattice in organic compounds is ductile, increasing their adaptability to divalent cations. A wide range of layered organic compounds, including 9,10-anthraquinone (AQ),[198] 2,3,5,6-tetrachloro-1,4-benzoquinone,[206] poly-(tetraminobenzoquinone-alt-2,5-dihydroxy-1,4-benzoquinone,[207] perylene-3,4,9,10-tetracarboxylic dianhydride,[208] perylene-3,4,9,10-tetracarboxylic diimide (PTCDI), etc., have been confirmed in rocking chair AZIBs with PTCDI stands out for its low discharge potential attributed to high lowest unoccupied molecular orbital (LUMO) (Figure 15e). Liu et al. in situ polymerized the PTCDI on the rGO (PTCDI/rGO) (Figure 15f), evoking coparticipant phase transformation of protons and Zn^{2+}, to reach a capacity of about 40 mAh g^{-1} of total anode mass (corresponding to 193 mAh g_{active}^{-1}) (Figure 15g), along with a capacity retention of 75% after 150 cycles (Figure 15h).[200]

In summary, high energy density cannot solely depend on the elevation of the cathodes' capacity. Collaboration from weight reduction is also crucial for holistic advancement. The commercialization will put demand on the precise amount control of the

anode, and the ultimate N/P ratio goal should approach 1. Thus, attempts to reduce the amount of zinc by replacing commercial zinc foils with zinc-lean, anode-free, or Zn^{2+}-containing anode designs have been attempted, and diverse anode stabilization strategies have been proposed to confront the severity of the limited zinc reservoir. At the same time, for those advanced cathode materials, they should be coupled with reliable anode stabilization strategies to reduce the N/P ratio. This more practical setup can exhibit the accurate evaluation of those cathodes, which is more instructive for future cathode screening and design. Thus, only the reciprocal commitment from both electrodes can pave the way leading the AZIBs to obtain energy density fulfilling the industrial requirement.

5. High-Energy-Density AZIBs via Optimized Separators

Electrodes and electrolytes, as core components participating in electrochemical reactions, have attracted much attention. However, besides the electrolyte, the separator, as another part that is interactive with both electrodes, has not been emphasized enough. Fundamentals for a separator include electronic isolation, favorable chemical stability and mechanical strength, and suitable electrolyte uptake capability. All these factors considered, braided glass fibers (GF) are commonly adopted, with the GF series from Whatman being the most frequent. The thicknesses of separators in this series vary from 260 to 680 μm, and the GF/D (680 μm) is the most standard. This non-negligible thickness help retard dendrites penetration but significantly damages the overall energy density. Therefore, separators with reduced thickness/mass have been devised to attain the higher energy density. In addition to the direct influence on the calculation of the energy density, separators can also be functionalized to reduce the amount of electrolyte and improve the reversibility of both electrodes. With the more stable electrode/electrolyte interface, the issue of dendrite can be relieved, so the thickness of the separator can be further reduced. Furthermore, as one step forward, a separator-free battery constructing an ion conductive layer on the electrode was fabricated to maximize the systematic energy density.

5.1. Ultrathin Separator

Advanced separators can be prepared by optimizing conventional glass fiber separators or fabricating with other isolating materials. The former choice requires the superposition of effective materials, further increasing the thickness. Thus, nonglass fiber separators are more typical for energy-dense requirements. Based on materials, ultrathin separators are majorly derived from cellulose, PAN, and Nafion, with other polymers like PVA, polyethylene (PE), aramid, etc., emerging recently.[209]

5.1.1. Cellulose-Based Separator

Cellulose is a widely distributed polymer that can be conveniently extracted from plants like cotton or bamboo.[210] Moreover, glucose in cellulose possesses rich polar functional groups, binding well with Zn^{2+} to prove the uniform deposition. Considering its suitable flexibility; cellulose fiber exhibits the qualification as the separator material. In current literature, multiple uncomplicated methods like filtration, thermal compression, solution casting, and magnetron sputtering are used to fabricate cellulose-based membranes.

Filtration of cellulose fiber dispersion is the most frequently used for its simplified process.[211] However, this technique makes pore sizes and porosity difficult to control. Therefore, Fu et al. introduced one additional step to adjust porosity with pore-generation agents. They mixed sodium dihydrogen citrate with freeze-dried cellulose aerogel and removed it with water after filtration to leave the expected pores. Consequently, a superior lifespan of more than 5000 h was achieved in Zn||Zn cells at 0.5 mA cm^{-2}, 0.25 mAh cm^{-2} with this 10 μm separator.[210b] Furthermore, other decorating materials can be exerted through extra filtration. For example, Li et al. coated carbonized persimmon branches (PBC) on commercial cellulose membrane by filtration. Hierarchical pore structures and O, N-containing functional groups facilitate Zn^{2+} transportation and homogenize the Zn^{2+} fluxes, guiding the uniform deposition.[212] However, the thickness is not effectively reduced due to the limitation of commercial cellulose. Thus, Zheng et al. fabricated their own bacterial cellulose first, followed by decorating Ag nanowires on one side through two-step filtration (**Figure 16**a). This Ag-doping separator is only 29 μm with Ag nanowires uniformly covering one side to provide the Janus effect (Figure 16b). The Ag side presents higher zincophilicity, electronic conductivity, and thermal conductivity to motivate the directional movement of Zn^{2+}, helping the Zn||VOH battery retain a high specific capacity of 318.1 mAh g^{-1} even at 50 °C (Figure 16c).[213]

Slurry casting is also popular for fabricating cellulose membranes. Cao et al. screened a mixture of cellulose and diverse ceramics and finally designed a 50 μm cellulose-ZrO_2 composite membrane (ZC) through slurry casting. Among all candidates, this ZC exhibits the highest ionic conductivity and Zn^{2+} transfer number, along with an inherent directional electric field.[214] Otherwise, precursors immersion for chemical doping, magnetron sputtering, or functional composites dropping have all been proposed for commercial cellular membrane tuning.[215] For the next step, by replacing commercial ones with ultrathin designs, the potential as energy-dense separators can be realized through these strategies.

5.1.2. PAN-Based Separator

PAN, with abundant zincophilic -CN groups, is handy for 3D construction through electrospinning.[216] As a current collector, carbonization endowing electronic conductivity is accepted, but the calcination is abandoned for separators. Shao et al. proposed an "all in one" battery with the sandwiched PAN. They sprayed carbon nanotubes on both sides of electrospinning PAN, and then deposited Zn and MnO_2 particles to form a 97 μm battery (Figure 16d). This compact adhesion between electrodes and separator maximizes the ion transportation efficiency, resulting in a volume density of 116.4 mW cm^{-3}.[217] Like cellulose, PAN membranes can also be produced through

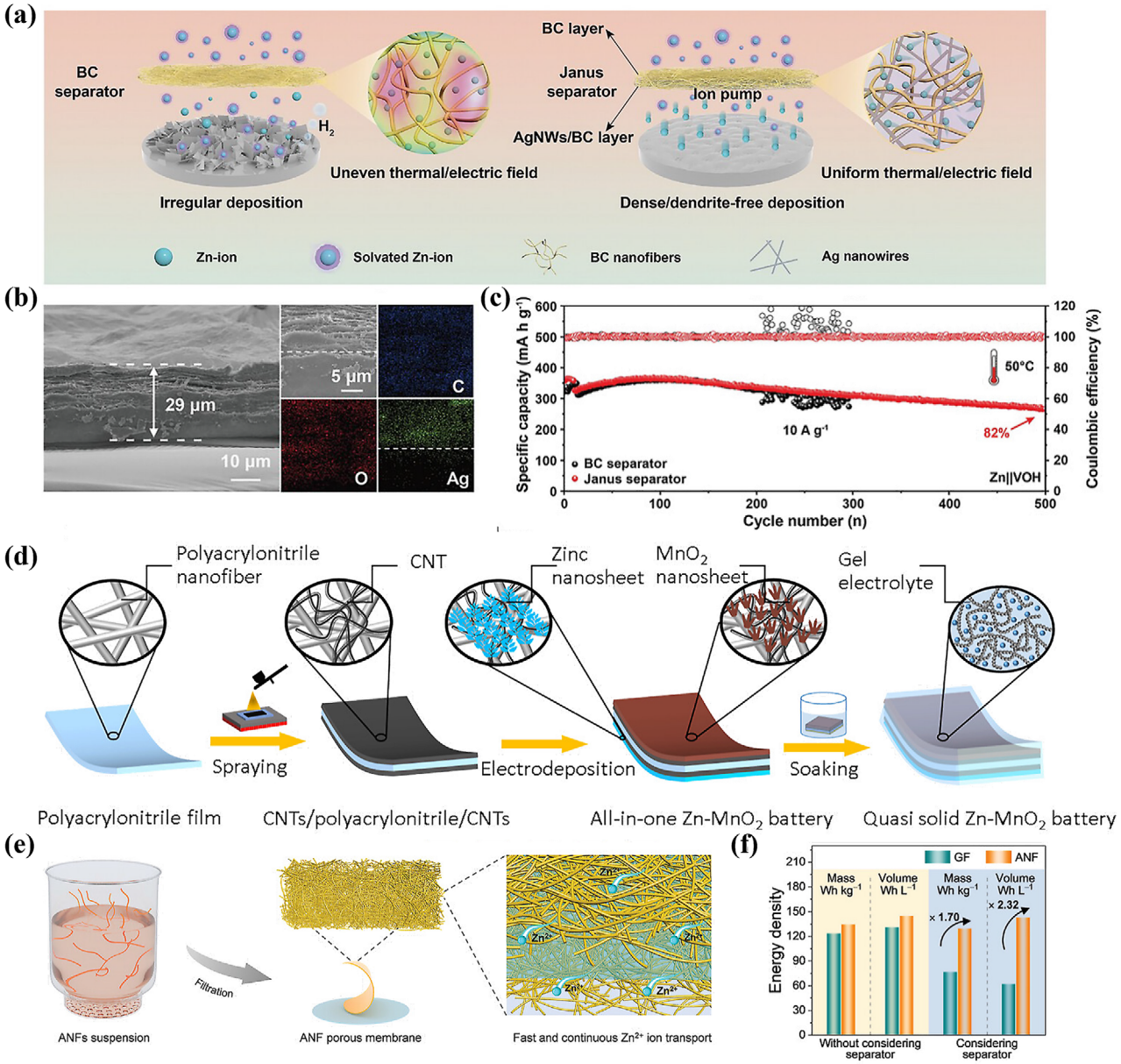

Figure 16. Ultrathin separators for AZIBs. a) Schematic illustration of ion transportation mechanism in the cellular separator and the Janus separator. b) SEM images of the cross-section of the Janus separator. c) The cycling stability of the Zn||VOH battery is 50 °C with the cellular and Janus separator. a–c) Reproduced with permission.[213] Copyright 2023, Wiley-VCH. d) Schematic illustration of the fabrication process of all-in-one Zn||MnO_2 battery. d) Reproduced with permission.[217] Copyright 2021, American Chemical Society. e) Schematic illustration of the fabrication process of the ANF separator. f) Gravimetric and volumetric energy densities of the Zn||MVOH battery with GF and ANF separators. e,f) Reproduced with permission.[210c] Copyright 2024, Wiley-VCH.

casting, but the structure is typically dense because the slurry is PAN solution instead of dispersion. Thus, groups with the cations swing function will be used as decoration, and the sulfonyl group is a perfect choice. For example, Lee et al. mixed lithium polysulfide (Li_2S_3) with PAN solution. Li_2S_3 will react with PAN, promoting crosslinking and forming sulfonyl functional groups. These groups endow this 30 μm PAN-S membrane with encouraging hygroscopic and selective transport characteristics revealing its potential for compact AZIBs.[218]

5.1.3. Nafion-Based Separator

The proton exchange membrane is the most mature ion-selectively conductive membrane, and Nafion series developed by Dupont company obtains the best market success. It contains PTFE backbones incorporated with the perfluorovinyl ether groups terminated with sulfonate groups, and shows reliable stability and superior proton conductivity in comprehensive acidic systems (polymer exchange membrane water electrolyzer/fuel cell, all-vanadium flow batteries, etc.).[219] However,

challenges remained for the practical employment of Nafion in AZIBs, and the critical one is the selectivity of divalent ions like Zn^{2+}. Thus, many efforts have been dedicated to building Zn^{2+} pathways, and the most convenient way is electrolyte immersion. Limited by the water-uptake capacity of Nafion, electrolyte absorption commonly lasts for multiple days. Even soaking Nafion 211 (25 µm) into 2 M $ZnSO_4$ electrolytes for 48 h, only 3.8 mg of electrolyte was absorbed, much lower than the 83 mg electrolyte for the GF membrane. The prepared Zn|Nafion|V_2O_5 battery exhibits an extraordinary specific capacity of 495.8 mAh g^{-1}, corresponding to an energy density of 374.4 Wh kg^{-1}.[220]

Nafion can also be fabricated in the laboratory by casting a solution of Nafion resins, and these membranes can be easily crafted. For example, Yuan et al. molded a lignin/Nafion mixed membrane with a thickness of 60 µm in their customized template. The interaction between $-SO_3^-$ and Zn^{2+} regulates the Zn^{2+} coordination to derive the lateral accumulation of zinc hydroxide sulfate, forming a robust and thin SEI layer and a capacity of 236 mAh g^{-1} is finally obtained in Zn||MnO_2 batteries.[221]

5.1.4. Other Ultrathin Separators

Even though cellulose, PAN, and Nafion have demonstrated much success, their poor mechanical strength limits further thickness reduction, demanding exploration of other isolating materials. The thinnest innovative membrane is now the 5-µm aramid separator fabricated through filtering aramid dispersion (Figure 16e). Those embedded nucleophilic carbonyl functional groups effectively modify the solvation structure and accelerate desolvation. The homogeneity of Zn^{2+} distribution is also promoted, which can be attributed to uniform nanopores. More promotionally, a tensile strength (117.8 MPa) 236 times that of the GF separator is also detected. Furthermore, the ultrathin membrane limits the electrolyte uptake, exhibiting, as shown in Figure 16f, a shocking gravimetric energy density of 129.2 Wh kg^{-1} (142.5 Wh L^{-1} for volumetric energy density) with a low electrolyte weight/capacity (E/C) ratio of 21.4 µL mAh^{-1}.[209c]

Ameliorating commercial thin polymer membranes such as PE (9 µm) separators is another feasible routine. Xue et al. sprayed biphthalic anhydride (BPDA) on the cathode side and 3,3′-diamino-4,4′-dihydroxydiphenyl sulfone (BisSF) on the anode side of a PE membrane. The BPDA shows the impactful inhibition of vanadium dissolution, and BisSF can repulse SO_4^{2-} while facilitating Zn^{2+} conduction. This coupled optimization stimulates the Zn||V_2O_5 pouch cell to realize a superior gravimetric energy density of 71.4 Wh kg^{-1} (133.3 Wh L^{-1}).[222] At the same time, the attractive thickness and hydrophilicity of this 9 µm commercial PE separator continue to motivate other optimization strategies like plasma treatment.[209b]

5.2. Separator-Free AZIBs

The ionic conductive and electronic isolating layer is not necessarily independent from electrodes. Therefore, inspired by SEIs, researchers have suggested using ex-situ ionic conductive layers exerted on electrodes to abandon the separator.

To the best of our knowledge, the first separator-free AZIB was proposed by Zhu et al. in 2022. They fixed ZSM-5 molecular sieves using the PVDF binder and then soaked in $ZnSO_4$ solution to form the solid-liquid mixed electrolyte (**Figure 17a**). The ZSM-5 presents a unique cage structure with two different vertical channels specific reaching a high surface area of 407.8 m^2 g^{-1} (Figure 17b). This two-phase electrolyte, weighing one-third of the GF separator, was directly sandwiched with a Zn anode and V_2O_5 cathode, suggesting outstanding gravimetric energy density with a specific capacity of 300 mAh g^{-1} at 1 A g^{-1} (Figure 17c).[223] Other researchers chose to construct the electrolyte membrane on the electrode surface. Xu et al. dissolved LaF_3 in n-methyl-2-pyrrolidone with 5 wt% PVDF, then coated the ink on zinc foils as the artificial SEI (LF@Zn). The LF@Zn was assembled with the VO_2 in direct contact after absorbing $ZnSO_4$, and this separator-free LF@Zn||VO_2 cell delivered a discharge capacity of 300 mAh g^{-1} at 0.6 A g^{-1}.[224]

In 2024, Sun et al. proposed a suspension buffer layer mixing cellulose nanofiber and tannin (Figure 17d), challenging the traditional solid form of the artificial SEI. The prepared viscous suspension is placed directly on the zinc foil and coupled with the VO_2 cathode. As illustrated in Figure 17e, rich O atoms on the tannin relieve negative charges in the coordination environment of Zn^{2+}, encouraging the bonding between Zn and O. As a result, the electron reception process becomes effortless, facilitating the Zn deposition. Then, the thickness of this separator-free cell is only 67 µm, which is only 1/15 of the traditional GF-based battery (1050 µm), and an exceedingly high energy density of 99.2 Wh L^{-1} can be obtained (Figure 17f).[225]

In conclusion, commercial separators are excessive in weight and thickness, restricting the energy density. Furthermore, the most common glass fiber separator lacks the ability to stabilize the electrode/electrolyte interface. As a result, the loss of active materials cannot be suppressed and the rigorous dendrite growth demands even a thicker separator. Thus, the role of separator in improving the overall energy density should be emphasized. Comprehensive self-made separators (mainly based on cellulose, PAN, and Nafion) have recently contributed to energy-dense batteries with their shrunk thickness. Also, plentiful functional groups on these materials are effective for binding water and derive the uniform deposition of zinc. Consequently, water-induced parasitic reactions can be suppressed for both the anode and cathode. A dendrite-free surface also mitigates the risk of separator penetration, so the sacrifice of the separator thickness to retard the short-circuit becomes unnecessary. Furthermore, other researchers even proposed separator-free designs exhibiting furtherly elevated energy densities.

6. Conclusion

One of the most imperative steps for projecting one energy conversion and storage technique into practical application is the cost/performance ratio. Therefore, attempts to elevate energy density have never stopped in energy storage systems. In the review, impacts of different components in AZIBs on the energy density performance are summarized. The major strategies for improving energy density are comprehensively analyzed. These strategies consistently elevate the energy density by maximizing the energy output and reducing the volume/mass of the system. Even though these techniques presented overwhelming performance in the laboratory, the future engineering of AZIBs

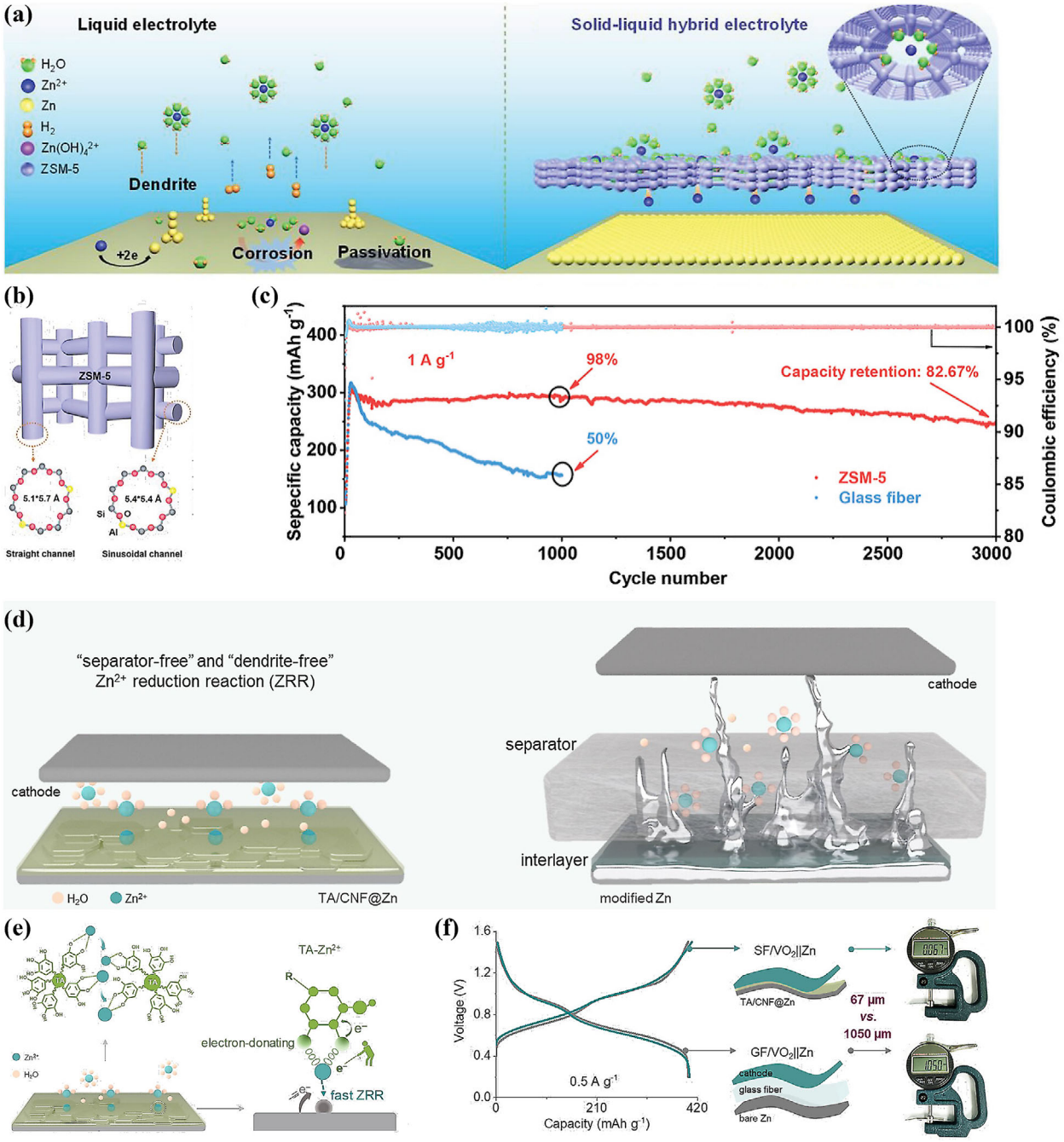

Figure 17. Separator-free configurations of AZIBs. a) Schematic illustration of the operation process in the liquid $ZnSO_4$ electrolyte and ZSM-5 hybrid electrolyte. b) Structure of ZSM-5. c) Cycling stability of Zn||V_2O_5 battery with liquid and hybrid electrolyte at 1 A g^{-1}. a–c) Reproduced with permission.[223] Copyright 2022, Wiley-VCH. d) Schematic illustration of Zn deposition in TA/CNF buffer layer and commercial separator. e) The coordination process during the Zn reduction process. f) Galvanostatic charge and discharge curves of Zn||VO_2 battery at 0.5 A g^{-1}, and thickness measurement of Zn||VO_2 battery with TA/CNF buffer layer and GF separator. d–f) Reproduced with permission.[225] Copyright 2024, Wiley-VCH.

requires the transfer of the horizon from the laboratory to the industrial level. Thus, the integration and coordination of optimization of all components instead of a single one is imperative for holistic improvement. Meanwhile, the gap between designed evaluation conditions and criteria of the scientific innovation and industrial implementation needs to be closed. Herein, we summarize several unsolved issues requiring further exploration and propose some perspectives to realize the high energy density AZIBs (**Figure 18**).

1) Cathode optimization strategies need to combine high-voltage and high-capacity. Many cathode materials usually

Figure 18. Perspectives of strategies to design high energy density aqueous zinc-ion batteries.

exhibit only the unique high-voltage or the high-capacity merit. For example, PBAs represent cathodes with high voltage and unfavorable capacities, and multiple vanadium oxides perform oppositely. Therefore, more specific strategies should be implemented for cathodes trapped in these two clusters to make up for their shortcomings. For those high voltage cathodes, the capacity can be improved by increasing the electron transfer number and active positions, and this can be achieved through the heterogeneous redox reactions and regulation of ion concentration and distribution on electrodes. On the contrary, alternating the crystal structure to make it suitable for more diverse charge carriers is beneficial for elevating the discharge platform for cathodes with high capacity and unfavorable discharge voltage. Furthermore, for those cathodes presenting a discharge voltage incoherent with the ideal potential difference calculated from the Gibbs free energy change, a more reliable mechanism requires a further exploration. As for a S cathode, the current low discharge platform makes the design of feasible high-voltage redox couples imperative. The employment of recent innovative configurations like the decoupling design with a better flexibility of electrolytes selection may make the initiation of new conversions with a broader potential difference more possible.

2) Systematic volume/mass reduction requires more attention by establishing repeatable, stable, and scalable criteria of anodes and nonelectrochemically active component, and upgrading the configuration. Although the fabrication of lightweight anodes and separators is demonstrated in the laboratory, the focus is still on their electrochemical performance. The scalability and complexity are rarely evaluated. Coin cells and pouch cells are most commonly utilized in the laboratory. The size of electrodes in both cells ranges from

1 to 20 cm^{-2}. However, for large-scale energy storage installments, they are commonly fabricated with a large number of stacks containing electrodes and separators up to meters. The requirement of mass production demands a high degree of uniformity and convenience to ensure the favorable industrial repeatability and economic efficiency. Thus, for future development of such components, those convenient and uniform one-step methods like the annealing or solution casting should obtain a higher priority. At the same time, the compact configuration should be kept especially for those novel decoupling designs. Currently, research work about decoupling designs introduces more on the feasibility of their redox couples, and demonstration is commonly conducted in the H-type cells. This left much space for the engineering refinement, and the ultimate structure must be terse. Considering the severe electrolyte crossover in a compact cell, before the cell upgrade, the further development of an asymmetric membrane with a pH buffer layer clamped in the middle may be supportive.

3) Performance evaluation of AZIBs under more practical conditions can accelerate their industrial applications. Even though there is still a long journey for AZIBs to realize the commercialization, industrialized evaluations should not be neglected to avoid any underestimation or overestimation. The widely adopted testing setups and objective environment show the obvious discrepancy to the actual operation. For instance, besides the non-negligible excessive amount of the anode and separator, the quantity of electrolyte has also not been precisely controlled. Moreover, the cycling in the laboratory is also set in a consecutive manner and with high current densities for the accelerating test. Thus, once a new technique is proposed, the cross-validation among low DoD, N/P ratio, E/C ratio, self-discharge tests, etc., is necessary. The supplementation of more realistic cycling, like one or two charge/discharge cycles in 1 day, is also crucial for accurately determining contributions of these innovative materials, mechanisms, and configurations to industrial level application. Furthermore, unlike the laboratory with a relatively standard temperature, humidity, and pressure, environmental challenges are numerous for a commercial battery. Therefore, tests with more complicated conditions become crucial. This also highlights the introduction of the battery management system (BMS) to AZIBs to maximize the energy output facing both internal and external variations.
4) The evaluation index of energy densities should be more rationalized. Most of the reported energy densities are still based on the volume/mass of active cathode materials, and only the value before degradation is calculated. This manner usually causes a serious overestimation of their potential for commercialization. Therefore, the assessment based on all components (cathode, anode, electrolyte, separator, battery case, etc.) is more rational. For example, some cathodes exhibit a superior capacity with the water-in-salts electrolyte. Considering the mass of highly concentrated electrolytes, a noteworthy gap must exist between the cathode-based and all-based energy density. Furthermore, accounting for the voltage decay, the energy density after long-term cycling should be supplemented as an additional criterion besides calculating the capacity retention only.

Overall, the vigorous development of aqueous zinc-ion batteries is an exciting signal, indicating the emergence of one promising technique supplementary to the battery family. However, there is still a long journey to bring their energy densities to the practical level. Encouragingly, continuous innovations burst out for separate components. The elevation of capacities and operation voltages of cathodes, the expansion of ESW of electrolytes conjugating to the upper voltage limit of advanced cathodes, the reduction of extra weight/volume of anodes/separator all contribute to the increasingly higher energy density. If these independent developments can be integrated synergistically, the record of energy density must be refreshed again. In this review, we summarized the previous representatives and introduced their mentality of design. We sincerely hope that this review offers some insights that will be helpful for the future development of high-energy-density AZIBs.

Acknowledgements

M.T. and Q.L. contributed equally to this work. The work described in this paper was supported by a grant from Research Institute for Advanced Manufacturing at The Hong Kong Polytechnic University (CD8Z), and a grant from Research Centre for Carbon-Strategic Catalysis (RC-CSC), The Hong Kong Polytechnic University (CE2X). This work was also supported by the Hong Kong Ph.D. Fellowship Scheme (No. PF21-65328).

Conflict of Interest

The authors declare no conflict of interest.

Keywords

aqueous zinc-ion battery, electrolyte engineering, energy storage, high-energy-density

Received: January 20, 2025
Revised: April 7, 2025
Published online:

[1] a) X. Zhang, J. Hu, N. Fu, W. Zhou, B. Liu, Q. Deng, X. Wu, *InfoMat* **2022**, *4*, 12306; b) M. Song, H. Tan, D. Chao, H. Fan, *Adv. Funct. Mater.* **2018**, *28*, 1802564.
[2] C. Zu, H. Li, *Energy Environ. Sci.* **2011**, *4*, 2614.
[3] H. Li, *Joule* **2019**, *3*, 911.
[4] Y. Lu, Y. Lu, Z. Niu, J. Chen, *Adv. Energy Mater.* **2018**, *8*, 1702469.
[5] B. Wu, Y. Mu, Z. Li, M. Li, L. Zeng, T. Zhao, *Chin. Chem. Lett.* **2023**, *34*, 107629.
[6] Q. Liu, Z. Yu, B. Zhang, *Small Methods* **2024**, *8*, 2300255.
[7] D. Deng, *Energy Sci. Eng.* **2015**, *3*, 385.
[8] a) G. Li, L. Sun, S. Zhang, C. Zhang, H. Jin, K. Davey, G. Liang, S. Liu, J. Mao, Z. Guo, *Adv. Funct. Mater.* **2024**, *34*, 2301291; b) C. Li, X. Zhang, W. He, G. Xu, R. Sun, *J. Power Sources* **2020**, *449*, 227596; c) C. Liu, X. Xie, B. Lu, J. Zhou, S. Liang, *ACS Energy Lett.* **2021**, *6*, 1015.
[9] a) G. Wang, M. Zhu, G. Chen, Z. Qu, B. Kohn, U. Scheler, X. Chu, Y. Fu, O. G. Schmidt, X. Feng, An A-F Zn-G Battery, *Adv. Mater.* **2022**, *34*, 2201957; b) J. Chen, M. Chen, H. Ma, W. Zhou, X. Xu, *Energy Rev.* **2022**, *1*, 100005.

[10] B. Zhang, P. Dong, S. Yuan, Y. Zhang, Y. Zhang, Y. Wang, *Chem. Bio. Eng.* **2024**, *1*, 113.
[11] L. Meng, Y. Zhu, Y. Lu, T. Liang, L. Zhou, J. Fan, Y. C. Kuo, P. Guan, T. Wan, L. Hu, D. Chu, *ChemElectroChem* **2024**, *11*, 202300495.
[12] A. Guo, Z. Wang, L. Chen, W. Liu, K. Zhang, L. Cao, B. Liang, D. Luo, *ACS Nano* **2024**, *18*, 27261.
[13] T. Zhou, G. Gao, *Nano Energy* **2024**, *127*, 109691.
[14] a) Y. Chen, S. Gu, S. Wu, X. Ma, I. Hussain, Z. Sun, Z. Lu, K. Zhang, *Chem. Eng. J.* **2022**, *450*, 137923; b) Y. Zhao, X. Xia, Q. Li, Y. Wang, Y. Fan, Y. Zhao, W. Liu, X. Sun, *Energy Storage Mater.* **2024**, *67*, 103268.
[15] X. Xia, Y. Zhao, Y. Zhao, M. Xu, W. Liu, X. Sun, *Nano Res.* **2023**, *16*, 2511.
[16] X. Gao, C. Shen, H. Dong, Y. Dai, P. Jiang, I. P. Parkin, H. Zhang, C. J. Carmalt, G. He, *Energy Environ. Sci.* **2024**, *17*, 2287.
[17] H. Luo, B. Wang, F. Wang, J. Yang, F. Wu, Y. Ning, Y. Zhou, D. Wang, H. Liu, S. Dou, *ACS Nano* **2020**, *14*, 7328.
[18] K. Zhu, T. Wu, K. Huang, *Energy Storage Mater.* **2021**, *38*, 473.
[19] Z. Tie, L. Liu, S. Deng, D. Zhao, Z. Niu, *Angew. Chem., Int. Ed.* **2020**, *59*, 4920.
[20] Z. Li, J. Tan, X. Zhu, S. Xie, H. Fang, M. Ye, J. Shen, *Energy Storage Mater.* **2022**, *51*, 294.
[21] Y. Gao, G. Li, F. Wang, J. Chu, P. Yu, B. Wang, H. Zhan, Z. Song, *Energy Storage Mater.* **2021**, *40*, 31.
[22] Y. Wang, X. Wang, J. Tang, W. Tang, *J. Mater. Chem. A* **2022**, *10*, 13868.
[23] Y. Chen, J. Li, Q. Zhu, K. Fan, Y. Cao, G. Zhang, C. Zhang, Y. Gao, J. Zou, T. Zhai, C. Wang, *Angew. Chem., Int. Ed.* **2022**, *61*, 202116289.
[24] H. Zhang, D. Xu, L. Wang, Z. Ye, B. Chen, L. Pei, Z. Wang, Z. Cao, J. Shen, M. Ye, *Small* **2021**, *17*, 2100902.
[25] S. Zheng, D. Shi, D. Yan, Q. Wang, T. Sun, T. Ma, L. Li, D. He, Z. Tao, J. Chen, *Angew. Chem., Int. Ed.* **2022**, *61*, 202117511.
[26] T. Xiong, Z. G. Yu, H. Wu, Y. Du, Q. Xie, J. Chen, Y. Zhang, S. J. Pennycook, W. S. V. Lee, J. Xue, *Adv. Energy Mater.* **2019**, *9*, 1803815.
[27] L. Wang, Z. Cao, P. Zhuang, J. Li, H. Chu, Z. Ye, D. Xu, H. Zhang, J. Shen, M. Ye, *ACS Appl. Mater. Interfaces* **2021**, *13*, 13338.
[28] T. Sun, Q. Nian, S. Zheng, X. Yuan, Z. Tao, *J. Power Sources* **2020**, *478*, 228758.
[29] M. Zhang, W. Wu, J. Luo, H. Zhang, J. Liu, X. Liu, Y. Yang, X. Lu, *J. Mater. Chem. A* **2020**, *8*, 11642.
[30] J. Ji, H. Wan, B. Zhang, C. Wang, Y. Gan, Q. Tan, N. Wang, J. Yao, Z. Zheng, P. Liang, J. Zhang, H. Wang, L. Tao, Y. Wang, D. Chao, H. Wang, *Adv. Energy Mater.* **2021**, *11*, 2003203.
[31] B. Wu, G. Zhang, M. Yan, T. Xiong, P. He, L. He, X. Xu, L. Mai, *Small* **2018**, *14*, 1703850.
[32] S. Deng, Z. Yuan, Z. Tie, C. Wang, L. Song, Z. Niu, *Angew. Chem., Int. Ed.* **2020**, *59*, 22002.
[33] Y. Yang, Y. Tang, S. Liang, Z. Wu, G. Fang, X. Cao, C. Wang, T. Lin, A. Pan, J. Zhou, *Nano Energy* **2019**, *61*, 617.
[34] G. Su, S. Chen, H. Dong, Y. Cheng, Q. Liu, H. Wei, E. H. Ang, H. Geng, C. C. Li, *Nanoscale* **2021**, *13*, 2399.
[35] T. Hu, Z. Feng, Y. Zhang, Y. Liu, J. Sun, J. Zheng, H. Jiang, P. Wang, X. Dong, C. Meng, *Inorg. Chem. Front.* **2021**, *8*, 79.
[36] M. Wang, J. Zhang, L. Zhang, J. Li, W. Wang, Z. Yang, L. Zhang, Y. Wang, J. Chen, Y. Huang, D. Mitlin, X. Li, *ACS Appl. Mater. Interfaces* **2020**, *12*, 31564.
[37] D. Bin, W. Huo, Y. Yuan, J. Huang, Y. Liu, Y. Zhang, F. Dong, Y. Wang, Y. Xia, *Chem* **2020**, *6*, 968.
[38] P. He, J. Liu, X. Zhao, Z. Ding, P. Gao, L. Fan, *J. Mater. Chem. A* **2020**, *8*, 10370.
[39] T. Lv, Y. Liu, H. Wang, S. Yang, C. Liu, H. Pang, *Chem. Eng. J.* **2021**, *411*, 128533.
[40] W. Du, J. Xiao, H. Geng, Y. Yang, Y. Zhang, E. H. Ang, M. Ye, C. C. Li, *J. Power Sources* **2020**, *450*, 227716.
[41] Z. Xu, Y. Zhang, W. Gou, M. Liu, Y. Sun, X. Han, W. Sun, C. Li, *Chem. Commun.* **2022**, *58*, 8145.
[42] W. Li, K. Wang, K. Jiang, *Adv. Sci.* **2020**, *7*, 2000761.
[43] Y. Guo, R. Chua, Y. Chen, Y. Cai, E. J. J. Tang, J. J. N. Lim, T. H. Tran, V. Verma, M. W. Wong, M. Srinivasan, *Small* **2023**, *19*, 2207133.
[44] Y. Zhao, D. Wang, X. Li, Q. Yang, Y. Guo, F. Mo, Q. Li, C. Peng, H. Li, C. Zhi, *Adv. Mater.* **2020**, *32*, 2003070.
[45] H. Zhang, Z. Shang, G. Luo, S. Jiao, R. Cao, Q. Chen, K. Lu, *ACS Nano* **2022**, *16*, 7344.
[46] D. Liu, B. He, Y. Zhong, J. Chen, L. Yuan, Z. Li, Y. Huang, *Nano Energy* **2022**, *101*, 107474.
[47] C. Dai, X. Jin, H. Ma, L. Hu, G. Sun, H. Chen, Q. Yang, M. Xu, Q. Liu, Y. Xiao, X. Zhang, H. Yang, Q. Guo, Z. Zhang, L. Qu, *Adv. Energy Mater.* **2021**, *11*, 2003982.
[48] Z. Chen, Q. Yang, F. Mo, N. Li, G. Liang, X. Li, Z. Huang, D. Wang, W. Huang, J. Fan, C. Zhi, *Adv. Mater.* **2020**, *32*, 2001469.
[49] C. Guo, S. Yi, R. Si, Y. Wang, H. Liu, F. Yu, J. Li, *Chem. Eng. J.* **2023**, *469*, 143845.
[50] Z. Yan, J. Li, H. Liu, H. Zhang, S. Xi, Z. Zhu, *Angew. Chem., Int. Ed.* **2023**, *62*, 202312000.
[51] Z. Chen, F. Mo, T. Wang, Q. Yang, Z. Huang, D. Wang, G. Liang, A. Chen, Q. Li, Y. Guo, X. Li, J. Fan, C. Zhi, *Energy Environ. Sci.* **2021**, *14*, 2441.
[52] H. Xu, W. Yang, M. Li, H. Liu, S. Gong, F. Zhao, C. Li, J. Qi, H. Wang, W. Peng, J. Liu, *Small* **2024**, *20*, 2310972.
[53] W. Li, D. Wang, *Adv. Mater.* **2023**, 2304983.
[54] T. Zhou, L. Zhu, L. Xie, Q. Han, X. Yang, L. Chen, G. Wang, X. Cao, *J. Colloid Interface Sci.* **2022**, *605*, 828.
[55] G. Chang, J. Liu, Y. Hao, C. Huang, Y. Yang, Y. Qian, X. Chen, Q. Tang, A. Hu, *Chem. Eng. J.* **2023**, *457*, 141083.
[56] W. Wu, S. Wang, L. Lin, H. Shi, X. Sun, *Energy Environ. Sci.* **2023**, *16*, 4326.
[57] M. Cui, J. Fei, F. Mo, H. Lei, Y. Huang, *ACS Appl. Mater. Interfaces* **2021**, *13*, 54981.
[58] M. Yang, Z. Yan, J. Xiao, W. Xin, L. Zhang, H. Peng, Y. Geng, J. Li, Y. Wang, L. Liu, Z. Zhu, *Angew. Chem., Int. Ed.* **2022**, *61*, 202212666.
[59] T. Zhou, H. Wan, M. Liu, Q. Wu, Z. Fan, Y. Zhu, *Mater. Today Energy* **2022**, *27*, 101025.
[60] A. Amiri, R. Sellers, M. Naraghi, A. A. Polycarpou, *ACS Nano* **2023**, *17*, 1217.
[61] A. Zhang, R. Zhao, Y. Wang, J. Yang, C. Wu, Y. Bai, *Energy Environ. Sci.* **2023**, *16*, 3240.
[62] M. Yan, P. He, Y. Chen, S. Wang, Q. Wei, K. Zhao, X. Xu, Q. An, Y. Shuang, Y. Shao, K. T. Mueller, L. Mai, J. Liu, J. Yang, *Adv. Mater.* **2018**, *30*, 1703725.
[63] C. Wang, Y. Zeng, X. Xiao, S. Wu, G. Zhong, K. Xu, Z. Wei, W. Su, X. Lu, *J. Energy Chem.* **2020**, *43*, 182.
[64] S. Khamsanga, R. Pornprasertsuk, T. Yonezawa, A. A. Mohamad, S. Kheawhom, *Sci. Rep.* **2019**, *9*, 8441.
[65] X. Wang, L. Liu, Z. Hu, C. Peng, C. Han, W. Li, H. E. D. A. Zinc-Chalcogen, *Adv. Energy Mater.* **2023**, *13*, 2302927.
[66] Q. Yang, X. Li, Z. Chen, Z. Huang, C. Zhi, *Acc. Mater. Res.* **2022**, *3*, 78.
[67] a) Y. Zeng, X. Zhang, Y. Meng, M. Yu, J. Yi, Y. Wu, X. Lu, Y. Tong, *Adv. Mater.* **2017**, *29*, 1700274; b) S. Deng, B. Xu, J. Zhao, C. W. Kan, X. Liu, *Angew. Chem., Int. Ed.* **2024**, *63*, 202401996.
[68] G. Liu, H. Huang, R. Bi, X. Xiao, T. Ma, L. Zhang, *J. Mater. Chem. A* **2019**, *7*, 20806.
[69] V. Verma, S. Kumar, W. Manalastas, Jr., J. Zhao, R. Chua, S. Meng, P. Kidkhunthod, M. Srinivasan, *ACS Appl. Energy Mater.* **2019**, *2*, 8667.
[70] S. Islam, M. H. Alfaruqi, V. Mathew, J. Song, S. Kim, S. Kim, J. Jo, J. P. Baboo, D. T. Pham, D. Y. Putro, Y. K. Sun, J. Kim, *J. Mater. Chem. A* **2017**, *5*, 23299.

[71] Z. Cao, L. Wang, H. Zhang, X. Zhang, J. Liao, J. Dong, J. Shi, P. Zhuang, Y. Cao, M. Ye, J. Shen, P. M. Ajayan, *Adv. Funct. Mater.* **2020**, *30*, 2000472.
[72] a) Y. Liu, F. Zhao, Z. Zhang, C. Gu, Y. Zhang, H. Chang, *J. Mater. Sci.: Mater. Electron.* **2023**, *34*, 1321; b) S. Wu, Y. Ding, L. Hu, X. Zhang, Y. Huang, S. Chen, *Mater. Lett.* **2020**, *277*, 128268.
[73] a) Y. Li, R. Zhang, J. Qian, Y. Gong, H. Li, C. Wu, Y. Bai, F. Wu, *Energy Mater. Adv.* **2023**, *4*, 0044; b) J. Wang, T. Ghosh, Z. Ju, M. Ng, G. Wu, G. Yang, X. Zhang, L. Zhang, A. D. Handoko, S. Kumar, W. Busayaporn, D. Kaewsuwan, C. Jiang, M. Wei, G. Yu, Z. W. Seh, *Matter* **2024**, *7*, 1833.
[74] M. Chen, M. Zhou, Q. Wang, C. Xu, S. Wang, J. Ning, T. Wang, K. Wang, K. Jiang, *Adv. Funct. Mater.* **2025**, *35*, 2414032.
[75] L. Ma, S. Chen, C. Long, X. Li, Y. Zhao, Z. Liu, Z. Huang, B. Dong, J. A. Zapien, C. Zhi, *Adv. Energy Mater.* **2019**, *9*, 1902446.
[76] Z. Liu, Q. Yang, D. Wang, G. Liang, Y. Zhu, F. Mo, Z. Huang, X. Li, L. Ma, T. Tang, Z. Lu, C. Zhi, *Adv. Energy Mater.* **2019**, *9*, 1902473.
[77] L. Ma, S. Chen, H. Li, Z. Ruan, Z. Tang, Z. Liu, Z. Wang, Y. Huang, Z. Pei, J. A. Zapien, C. Zhi, *Energy Environ. Sci.* **2018**, *11*, 2521.
[78] Z. Hou, X. Zhang, X. Li, Y. Zhu, J. Liang, Y. Qian, *J. Mater. Chem. A* **2017**, *5*, 730.
[79] J. Yue, S. Li, S. Chen, J. Yang, X. Lu, Y. Li, R. Zhao, C. Wu, Y. Bai, *Energy Mater. Adv.* **2023**, *4*, 0050.
[80] F. Wan, Y. Zhang, L. Zhang, D. Liu, C. Wang, L. Song, Z. Niu, J. Chen, *Angew. Chem., Int. Ed.* **2019**, *58*, 7062.
[81] Z. Bai, G. Wang, H. Liu, Y. Lou, N. Wang, H. Liu, S. Dou, *Chem. Sci.* **2024**, *15*, 3071.
[82] S. Zhang, J. Hao, H. Wu, C. Kao, Q. Chen, C. Ye, S. Qiao, *ACS Nano* **2024**, *18*, 28557.
[83] W. Gao, S. Cheng, Y. Zhang, E. Xie, J. Fu, *Adv. Funct. Mater.* **2023**, *33*, 2211979.
[84] a) D. Yu, A. Kumar, T. A. Nguyen, M. T. Nazir, G. Yasin, *ACS Sustainable Chem. Eng.* **2020**, *8*, 13769; b) S. Chai, J. Yao, Y. Wang, J. Zhu, J. Jiang, *Chem. Eng. J.* **2022**, *439*, 135676.
[85] J. Yang, H. Liu, X. Zhao, X. Zhang, K. Zhang, M. Ma, Z. Gu, J. Cao, X. Wu, *J. Am. Chem. Soc.* **2024**, *146*, 6628.
[86] Q. Zhang, Y. Ma, Y. Lu, Y. Ni, L. Lin, Z. Hao, Z. Yan, Q. Zhao, J. Chen, *J. Am. Chem. Soc.* **2022**, *144*, 18435.
[87] F. Wang, J. Tseng, Z. Liu, P. Zhang, G. Wang, G. Chen, W. Wu, M. Yu, Y. Wu, X. Feng, *Adv. Mater.* **2020**, *32*, 2000287.
[88] X. Li, T. Li, P. Xu, C. Xie, Y. Zhang, X. Li, *Adv. Funct. Mater.* **2021**, *31*, 2100133.
[89] X. Jin, L. Song, C. Dai, Y. Xiao, Y. Han, X. Li, Y. Wang, J. Zhang, Y. Zhao, Z. Zhang, N. Chen, L. Jiang, L. Qu, *Adv. Mater.* **2022**, *34*, 2109450.
[90] a) J. Kang, C. Wang, Z. Liu, L. Wang, Y. Meng, Z. Zhai, J. Zhang, H. Lu, *Energy Storage Mater.* **2024**, *68*, 103367; b) X. Li, M. Li, Z. Huang, G. Liang, Z. Chen, Q. Yang, Q. Huang, C. Zhi, *Energy Environ. Sci.* **2021**, *14*, 407; c) T. Hu, Y. Zhao, Y. Yang, H. Lv, R. Zhong, F. Ding, F. Mo, H. Hu, C. Zhi, G. Liang, *Adv. Mater.* **2024**, *36*, 2312246.
[91] a) X. Yang, H. Fan, F. Hu, S. Chen, K. Yan, L. Ma, *Nano-Micro Lett.* **2023**, *15*, 126; b) T. Liu, C. Lei, H. Wang, C. Xu, W. Ma, X. He, X. Liang, *Sci. Bull.* **2024**, *69*, 1674.
[92] C. Xie, Y. Liu, W. Lu, H. Zhang, X. Li, *Energy Environ. Sci.* **2019**, *12*, 1834.
[93] W. Ma, T. Liu, C. Xu, C. Lei, P. Jiang, X. He, X. Liang, *Nat. Commun.* **2023**, *14*, 5508.
[94] C. Xie, C. Wang, Y. Xu, T. Li, Q. Fu, X. Li, *Nat. Energy* **2024**, *9*, 714.
[95] K. Lu, B. Song, Y. Zhang, H. Ma, J. Zhang, *J. Mater. Chem. A* **2017**, *5*, 23628.
[96] L. Zhang, L. Chen, X. Zhou, Z. Liu, *Adv. Energy Mater.* **2015**, *5*, 1400930.
[97] W. Pan, Y. Wang, X. Zhao, Y. Zhao, X. Liu, J. Xuan, H. Wang, D. Y. C. Leung, *Adv. Funct. Mater.* **2021**, *31*, 2008783.
[98] M. J. Park, A. Manthiram, *ACS Appl. Energy Mater.* **2020**, *3*, 5015.
[99] W. Li, K. Wang, S. Cheng, K. Jiang, *Energy Storage Mater.* **2018**, *15*, 14.
[100] F. Wang, E. Hu, W. Sun, T. Gao, X. Ji, X. Fan, F. Han, X. Yang, K. Xu, C. Wang, *Energy Environ. Sci.* **2018**, *11*, 3168.
[101] G. Li, Z. Yang, Y. Jiang, W. Zhang, Y. Huang, *J. Power Sources* **2016**, *308*, 52.
[102] H. Shi, Y. Song, Z. Qin, C. Li, D. Guo, X. Liu, X. Sun, *Angew. Chem., Int. Ed.* **2019**, *58*, 16057.
[103] L. Ma, N. Li, C. Long, B. Dong, D. Fang, Z. Liu, Y. Zhao, X. Li, J. Fan, S. Chen, S. Zhang, C. Zhi, *Adv. Funct. Mater.* **2019**, *29*, 1906142.
[104] V. Soundharrajan, B. Sambandam, S. Kim, V. Mathew, J. Jo, S. Kim, J. Lee, S. Islam, K. Kim, Y. Sun, J. Kim, *ACS Energy Lett.* **2018**, *3*, 1998.
[105] C. Wang, X. Ji, J. Liang, S. Zhao, X. Zhang, G. Qu, W. Shao, C. Li, G. Zhao, X. Xu, H. Li, *Angew. Chem., Int. Ed.* **2024**, *63*, 202403187.
[106] a) J. Hao, J. Long, B. Li, X. Li, S. Zhang, F. Yang, X. Zeng, Z. Yang, W. K. Pang, Z. Guo, *Adv. Funct. Mater.* **2019**, *29*, 1903605; b) Y. Wang, R. Zhao, M. Liu, J. Yang, A. Zhang, J. Yue, C. Wu, Y. Bai, *Adv. Energy Mater.* **2023**, *13*, 2302707.
[107] S. Zhang, Q. Gou, W. Chen, H. Luo, R. Yuan, K. Wang, K. Hu, Z. Wang, C. Wang, R. Liu, Z. Zhang, Y. Lei, Y. Zheng, L. Wang, F. Wan, B. Li, M. Li, *Adv. Sci.* **2024**, *11*, 2404968.
[108] a) P. Sun, L. Ma, W. Zhou, M. Qiu, Z. Wang, D. Chao, W. Mai, *Angew. Chem.* **2021**, *133*, 18395; b) H. Wang, W. Ye, B. Yin, K. Wang, M. S. Riaz, B. Xie, Y. Zhong, Y. Hu, *Angew. Chem., Int. Ed.* **2023**, *62*, 202218872.
[109] N. Wang, S. Zhai, Y. Ma, X. Tan, K. Jiang, W. Zhong, W. Zhang, N. Chen, W. Chen, S. Li, G. Han, Z. Li, *Energy Storage Mater.* **2021**, *43*, 585.
[110] Y. Wu, Z. Zhu, D. Shen, L. Chen, T. Song, T. Kang, Z. Tong, Y. Tang, H. Wang, C. S. Lee, *Energy Storage Mater.* **2022**, *45*, 1084.
[111] a) Y. Zhang, M. Zhu, K. Wu, F. Yu, G. Wang, G. Xu, M. Wu, H. Liu, S. Dou, C. Wu, *J. Mater. Chem. A* **2021**, *9*, 4253; b) J. Hao, L. Yuan, C. Ye, D. Chao, K. Davey, Z. Guo, S. Qiao, *Angew. Chem., Int. Ed.* **2021**, *60*, 7366.
[112] T. S. Groves, C. S. Perez-Martinez, R. Lhermerout, S. Perkin, *J. Phys. Chem. Lett.* **2021**, *12*, 1702.
[113] C. Zhang, J. Holoubek, X. Wu, A. Daniyar, L. Zhu, C. Chen, D. P. Leonard, I. A. Rodríguez-Pérez, J. Jiang, C. Fang, X. Ji, *Chem. Commun.* **2018**, *54*, 14097.
[114] X. Tang, P. Wang, M. Bai, Z. Wang, H. Wang, M. Zhang, Y. Ma, *Adv. Sci.* **2021**, *8*, 2102053.
[115] F. Wang, O. Borodin, T. Gao, X. Fan, W. Sun, F. Han, A. Faraone, J. A. Dura, K. Xu, C. Wang, *Nat. Mater.* **2018**, *17*, 543.
[116] a) J. Zhao, Y. Li, X. Peng, S. Dong, J. Ma, G. Cui, L. Chen, *Electrochem. Commun.* **2016**, *69*, 6; b) H. Zhang, X. Liu, B. Qin, S. Passerini, *J. Power Sources* **2020**, *449*, 227594.
[117] Y. Zhao, L. Ma, Y. Zhu, P. Qin, H. Li, F. Mo, D. Wang, G. Liang, Q. Yang, W. Liu, C. Zhi, *ACS Nano* **2019**, *13*, 7270.
[118] B. Zhang, L. Qin, Y. Fang, Y. Chai, X. Xie, B. Lu, S. Liang, J. Zhou, *Sci. Bull.* **2022**, *67*, 955.
[119] Q. Zhang, C. Li, Q. Li, Z. Pan, J. Sun, Z. Zhou, B. He, P. Man, L. Xie, L. Kang, X. Wang, J. Yang, T. Zhang, P. P. Shum, Q. Li, Y. Yao, L. Wei, *Nano Lett.* **2019**, *19*, 4035.
[120] S. Zhang, N. Yu, S. Zeng, S. Zhou, M. Chen, J. Di, Q. Li, *J. Mater. Chem. A* **2018**, *6*, 12237.
[121] Y. Shi, R. Wang, S. Bi, M. Yang, L. Liu, Z. Niu, *Adv. Funct. Mater.* **2023**, *33*, 2214546.
[122] a) Y. Wang, L. Mo, X. Zhang, Y. Ren, T. Wei, Y. He, Y. Huang, H. Zhang, P. Tan, Z. Li, J. Zhou, L. Hu, *Adv. Energy Mater.* **2024**, *14*, 2402041; b) J. Du, X. Zhan, Y. Xu, K. Diao, D. Zhang, S. Qin, *J. Mater. Sci. Technol.* **2025**, *212*, 251; c) F. Luo, S. Yang, Q. Wu, Y. Li, J. Zhang,

Y. Zhang, J. Huang, H. Xie, Y. Chen, *Energy Environ. Sci.* **2024**, *17*, 8570.
[123] W. Zeng, S. Zhang, J. Lan, Y. Lv, G. Zhu, H. Huang, W. Lv, Y. Zhu, *ACS Nano* **2024**, *18*, 26391.
[124] W. Ling, F. Mo, J. Wang, Q. Liu, Y. Liu, Q. Yang, Y. Qiu, Y. Huang, *Mater. Today Phys.* **2021**, *20*, 100458.
[125] H. Li, C. Han, Y. Huang, Y. Huang, M. Zhu, Z. Pei, Q. Xue, Z. Wang, Z. Liu, Z. Tang, Y. Wang, F. Kang, B. Li, C. Zhi, *Energy Environ. Sci.* **2018**, *11*, 941.
[126] Y. Liu, A. Gao, J. Hao, X. Li, J. Ling, F. Yi, Q. Li, D. Shu, *Chem. Eng. J.* **2023**, *452*, 139605.
[127] A. Bayaguud, X. Luo, Y. Fu, C. Zhu, *ACS Energy Lett.* **2020**, *5*, 3012.
[128] S. Zhang, J. Hao, D. Luo, P. Zhang, B. Zhang, K. Davey, Z. Lin, S. Qiao, *Adv. Energy Mater.* **2021**, *11*, 2102010.
[129] M. Tang, Q. Liu, Z. Yu, X. Zou, X. Huo, B. Zhang, L. An, *Small* **2024**, *20*, 2403457.
[130] L. You, S. Guo, Y. He, Y. Xie, S. Liang, G. Fang, *Adv. Funct. Mater.* **2025**, 2500780.
[131] T. Yan, M. Tao, J. Liang, G. Zheng, B. Wu, L. Du, Z. Cui, H. Song, *Energy Storage Mater.* **2024**, *65*, 103190.
[132] N. Hu, W. Lv, W. Chen, H. Tang, X. Zhang, H. Qin, D. Huang, J. Zhu, Z. Chen, J. Xu, H. He, *Adv. Funct. Mater.* **2024**, *34*, 2311773.
[133] Z. Wang, J. Diao, R. R. Vaidyula, G. Henkelman, C. B. Mullins, *Angew. Chem., Int. Ed.* **2025**, *64*, 202416619.
[134] L. Cao, D. Li, E. Hu, J. Xu, T. Deng, L. Ma, Y. Wang, X. Yang, C. Wang, *J. Am. Chem. Soc.* **2020**, *142*, 21404.
[135] N. Chang, T. Li, R. Li, S. Wang, Y. Yin, H. Zhang, X. Li, *Energy Environ. Sci.* **2020**, *13*, 3527.
[136] M. Li, X. Wang, J. Hu, J. Zhu, C. Niu, H. Zhang, C. Li, B. Wu, C. Han, L. Mai, *Angew. Chem., Int. Ed.* **2023**, *62*, 202215552.
[137] A. Naveed, H. Yang, J. Yang, Y. Nuli, J. Wang, *Angew. Chem., Int. Ed.* **2019**, *58*, 2760.
[138] J. Han, A. Mariani, A. Varzi, S. Passerini, *J. Power Sources* **2021**, *485*, 229329.
[139] Q. Liu, Z. Yu, Q. Zhuang, J. K. Kim, F. Kang, B. Zhang, *Adv. Mater.* **2023**, *35*, 2300498.
[140] Y. Xu, P. Cai, K. Chen, Y. Ding, L. Chen, W. Chen, Z. Wen, *Angew. Chem., Int. Ed.* **2020**, *59*, 23593.
[141] M. Yang, R. Chen, Y. Shen, X. Zhao, X. Shen, *Adv. Mater.* **2020**, *32*, 2001106.
[142] D. Chao, C. Ye, F. Xie, W. Zhou, Q. Zhang, Q. Gu, K. Davey, L. Gu, S. Qiao, *Adv. Mater.* **2020**, *32*, 2001894.
[143] J. R. Loh, J. Xue, W. S. V. Lee, *Small Methods* **2023**, *7*, 2300101.
[144] J. Xu, H. Li, Y. Jin, D. Zhou, B. Sun, M. Armand, G. Wang, *Adv. Mater.* **2024**, *36*, 2309726.
[145] J. Li, Z. Guo, J. Wu, Z. Zheng, Z. Yu, F. She, L. Lai, H. Li, Y. Chen, L. Wei, *Adv. Energy Mater.* **2023**, *13*, 2301743.
[146] J. Zheng, Y. Deng, J. Yin, T. Tang, R. Garcia-Mendez, Q. Zhao, L. A. Archer, *Adv. Mater.* **2022**, *34*, 2106867.
[147] Z. Chen, Q. Wu, X. Han, C. Wang, J. Chen, T. Hu, Q. He, X. Zhu, D. Yuan, J. Chen, Y. Zhang, L. Yang, Y. Ma, J. Zhao, *Angew. Chem., Int. Ed.* **2024**, *63*, 202401507.
[148] a) H. Yang, Z. Chang, Y. Qiao, H. Deng, X. Mu, P. He, H. Zhou, *Angew. Chem., Int. Ed.* **2020**, *59*, 9377; b) M. Cui, Y. Xiao, L. Kang, W. Du, Y. Gao, X. Sun, Y. Zhou, X. Li, H. Li, F. Jiang, C. Zhi, *ACS Appl. Energy Mater.* **2019**, *2*, 6490; c) Z. Zhao, J. Zhao, Z. Hu, J. Li, J. Li, Y. Zhang, C. Wang, G. Cui, *Energy Environ. Sci.* **2019**, *12*, 1938.
[149] D. Lv, H. Peng, C. Wang, H. Liu, D. Wang, J. Yang, Y. Qian, *J. Energy Chem.* **2023**, *84*, 81.
[150] D. Feng, Y. Jiao, P. Wu, *Angew. Chem., Int. Ed.* **2023**, *62*, 202314456.
[151] Z. Xu, H. Li, Y. Liu, K. Wang, H. Wang, M. Ge, J. Xie, J. Li, Z. Wen, H. Pan, S. Qu, J. Liu, Y. Zhang, Y. Tang, S. Chen, *Mater. Horiz.* **2023**, *10*, 3680.
[152] C. Huang, F. Huang, X. Zhao, Y. Hao, Y. Yang, Y. Qian, G. Chang, Y. Zhang, Q. Tang, A. Hu, X. Chen, *Adv. Funct. Mater.* **2023**, *33*, 2210197.
[153] Y. Li, W. Chen, S. Jia, M. Tang, Y. Zhai, L. Zhan, W. Chen, *J. Power Sources* **2024**, *614*, 235040.
[154] X. Song, L. Bai, C. Wang, D. Wang, K. Xu, J. Dong, Y. Li, Q. Shen, J. Yang, *ACS Nano* **2023**, *17*, 15113.
[155] a) M. Tang, Q. Liu, X. Zou, Z. Yu, K. Zhang, B. Zhang, L. An, *Energy Storage Mater.* **2025**, *74*, 103896; b) Z. Gong, Z. Li, P. Wang, K. Jiang, Z. Bai, K. Zhu, J. Yan, K. Ye, G. Wang, D. Cao, G. Chen, *Energy Mater. Adv.s* **2023**, *4*, 0035.
[156] a) H. Wang, Y. Chen, H. Yu, W. Liu, G. Kuang, L. Mei, Z. Wu, W. Wei, X. Ji, B. Qu, L. Chen, *Adv. Funct. Mater.* **2022**, *32*, 2205600; b) C. Wang, D. Wang, D. Lv, H. Peng, X. Song, J. Yang, Y. Qian, *Adv. Energy Mater.* **2023**, *13*, 2204388; c) B. Cui, Y. Gao, X. Han, W. Hu, *J. Mater. Sci. Technol.* **2022**, *117*, 72.
[157] Q. Li, H. Wang, H. Yu, M. Fu, W. Liu, Q. Zhao, S. Huang, L. Zhou, W. Wei, X. Ji, Y. Chen, L. Chen, *Adv. Funct. Mater.* **2023**, *33*, 2303466.
[158] Z. Yi, J. Liu, S. Tan, Z. Sang, J. Mao, L. Yin, X. Liu, L. Wang, F. Hou, S. X. Dou, H. Cheng, J. Liang, *Adv. Mater.* **2022**, *34*, 2203835.
[159] a) C. Tian, H. Wang, L. Xie, Y. Zhong, Y. Hu, *Adv. Energy Mater.* **2024**, *14*, 2400276; b) Y. Li, Z. Wang, W. Li, X. Zhang, C. Yin, K. Li, W. Guo, J. Zhang, X. Wu, *Energy Storage Mater.* **2023**, *61*, 102873.
[160] J. Li, Q. Lin, Z. Zheng, L. Cao, W. Lv, Y. Chen, *ACS Appl. Mater. Interfaces* **2022**, *14*, 12323.
[161] Y. Zeng, P. X. Sun, Z. Pei, Q. Jin, X. Zhang, L. Yu, X. W. Lou, *Adv. Mater.* **2022**, *34*, 2200342.
[162] Y. Zeng, Z. Pei, D. Luan, X. W. D. Lou, *J. Am. Chem. Soc.* **2023**, *145*, 12333.
[163] a) Z. Wang, K. Kang, J. Wu, Q. Hu, D. P. Harper, G. Du, S. Wang, K. Xu, *J. Mater. Res. Technol.* **2021**, *11*, 50; b) H. Yu, Y. Zeng, N. W. Li, D. Luan, L. Yu, X. W. Lou, *Sci. Adv.* **2022**, *8*, abm5766; c) Y. Zhang, S. Jiang, Y. Li, X. Ren, P. Zhang, L. Sun, H. Y. Yang, *Adv. Energy Mater.* **2023**, *13*, 2202826.
[164] X. Chen, Y. Chen, Y. Li, C. Guo, J. Pu, Y. Liu, X. Li, Y. Yao, W. Gong, P. Xue, J. Han, *Small Methods* **2024**, *8*, 2400408.
[165] B. Wu, B. Guo, Y. Chen, Y. Mu, H. Qu, M. Lin, J. Bai, T. Zhao, L. Zeng, *Energy Storage Mater.* **2023**, *54*, 75.
[166] Q. Li, Y. Wang, F. Mo, D. Wang, G. Liang, Y. Zhao, Q. Yang, Z. Huang, C. Zhi, *Adv. Energy Mater.* **2021**, *11*, 2003931.
[167] a) Y. Lin, M. Zhang, Y. Hu, S. Zhang, Z. Xu, T. Feng, H. Zhou, M. Wu, *Chem. Eng. J.* **2023**, *472*, 145136; b) Y. Lin, Y. Hu, S. Zhang, Z. Xu, T. Feng, H. Zhou, M. Wu, *ACS Appl. Energy Mater.* **2022**, *5*, 15222; c) X. Li, Q. Li, Y. Hou, Q. Yang, Z. Chen, Z. Huang, G. Liang, Y. Zhao, L. Ma, M. Li, Q. Huang, C. Zhi, *ACS Nano* **2021**, *15*, 14631.
[168] A. Li, M. Chen, Q. Tian, X. Han, J. Chen, *J. Alloys Compd.* **2023**, *965*, 171337.
[169] Q. Liu, Z. Yu, R. Zhou, B. Zhang, *Adv. Funct. Mater.* **2023**, *33*, 2210290.
[170] Z. Yang, Q. Zhang, W. Li, C. Xie, T. Wu, C. Hu, Y. Tang, H. Wang, *Angew. Chem., Int. Ed.* **2023**, *62*, 202215306.
[171] Y. Zhu, Y. Cui, H. N. Alshareef, *Nano Lett.* **2021**, *21*, 1446.
[172] X. Yang, Z. Zhang, M. Wu, Z. Guo, Z. Zheng, *Adv. Mater.* **2023**, *35*, 2303550.
[173] T. A. Nigatu, H. K. Bezabh, S. Jiang, B. W. Taklu, Y. Nikodimos, S. Yang, S. Wu, W. Su, C. Yang, B. J. Hwang, *Electrochim. Acta* **2023**, *443*, 141883.
[174] X. Zheng, Z. Liu, J. Sun, R. Luo, K. Xu, M. Si, J. Kang, Y. Yuan, S. Liu, T. Ahmad, T. Jiang, N. Chen, M. Wang, Y. Xu, M. Chuai, Z. Zhu, Q. Peng, Y. Meng, K. Zhang, W. Wang, W. Chen, *Nat. Commun.* **2023**, *14*, 76.

[175] K. Xu, X. Zheng, R. Luo, J. Sun, Y. Ma, N. Chen, M. Wang, L. Song, Q. Zhao, W. Chen, *Mater. Today Energy* **2023**, *34*, 101284.
[176] a) Y. Zhang, L. Wang, Q. Li, B. Hu, J. Kang, Y. Meng, Z. Zhao, H. Lu, *Nano-Micro Lett.* **2022**, *14*, 208; b) W. Ling, Q. Yang, F. Mo, H. Lei, J. Wang, Y. Jiao, Y. Qiu, T. Chen, Y. Huang, *Energy Storage Mater.* **2022**, *51*, 453; c) S. Xie, Y. Li, L. Dong, *J. Energy Chem.* **2023**, *76*, 32.
[177] a) X. Guo, H. Hong, Q. Li, J. Zhu, Z. Wu, Y. Wang, S. Yang, Z. Huang, Y. Huang, N. Li, C. Zhi, *Matter* **2024**, *7*, 4014; b) Y. An, Y. Tian, K. Zhang, Y. Liu, C. Liu, S. Xiong, J. Feng, Y. Qian, *Adv. Funct. Mater.* **2021**, *31*, 2101886.
[178] L. Cao, D. Li, T. Pollard, T. Deng, B. Zhang, C. Yang, L. Chen, J. Vatamanu, E. Hu, M. J. Hourwitz, L. Ma, M. Ding, Q. Li, S. Hou, K. Gaskell, J. T. Fourkas, X. Yang, K. Xu, O. Borodin, C. Wang, *Nat. Nanotechnol.* **2021**, *16*, 902.
[179] Y. Xu, X. Zheng, J. Sun, W. Wang, M. Wang, Y. Yuan, M. Chuai, N. Chen, H. Hu, W. Chen, *Nano Lett.* **2022**, *22*, 3298.
[180] Q. Zhang, Y. Ma, Y. Lu, X. Zhou, L. Lin, L. Li, Z. Yan, Q. Zhao, K. Zhang, J. Chen, *Angew. Chem., Int. Ed.* **2021**, *60*, 23357.
[181] H. Gan, J. Wu, R. Li, B. Huang, H. Liu, *Energy Storage Mater.* **2022**, *47*, 602.
[182] X. Yang, J. Lv, C. Cheng, Z. Shi, J. Peng, Z. Chen, X. Lian, W. Li, Y. Zou, Y. Zhao, M. H. Rümmeli, S. Dou, J. Sun, *Adv. Sci.* **2023**, *10*, 2206077.
[183] B. Wang, J. Yan, Y. Zhang, M. Ye, Y. Yang, C. C. Li, *Adv. Funct. Mater.* **2021**, *31*, 2102827.
[184] T. Xiong, Y. Zhang, Y. Wang, W. S. V. Lee, J. Xue, *J. Mater. Chem. A* **2020**, *8*, 9006.
[185] B. Yang, T. Qin, Y. Du, Y. Zhang, J. Wang, T. Chen, M. Ge, D. Bin, C. Ge, H. Lu, *Chem. Commun.* **2022**, *58*, 1550.
[186] Q. Zhang, T. Duan, M. Xiao, Y. Pei, X. Wang, C. Zhi, X. Wu, B. Long, Y. Wu, *ACS Appl. Mater. Interfaces* **2022**, *14*, 25516.
[187] X. Chen, R. Huang, M. Ding, H. He, F. Wang, S. Yin, *ACS Appl. Mater. Interfaces* **2022**, *14*, 3961.
[188] J. Cao, D. Zhang, Y. Yue, X. Wang, A. Srikhaow, C. Sriprachuabwong, A. Tuantranont, X. Zhang, Z. Wu, J. Qin, *Chem. Eng. J.* **2021**, *426*, 131893.
[189] W. Li, K. Wang, S. Cheng, K. Jiang, *Adv. Energy Mater.* **2019**, *9*, 1900993.
[190] B. Zhao, S. Wang, Q. Yu, Q. Wang, M. Wang, T. Ni, L. Ruan, W. Zeng, A. Flexible, *J. Power Sources* **2021**, *504*, 230076.
[191] Z. Lv, B. Wang, M. Ye, Y. Zhang, Y. Yang, C. C. Li, *ACS Appl. Mater. Interfaces* **2022**, *14*, 1126.
[192] J. Zhang, Q. Lei, Z. Ren, X. Zhu, J. Li, Z. Li, S. Liu, Y. Ding, Z. Jiang, J. Li, Y. Huang, X. Li, X. Zhou, Y. Wang, D. Zhu, M. Zeng, L. Fu, *ACS Nano* **2021**, *15*, 17748.
[193] Y. Yang, J. Xiao, J. Cai, G. Wang, W. Du, Y. Zhang, X. Lu, C. C. Li, *Adv. Funct. Mater.* **2021**, *31*, 2005092.
[194] L. Wen, Y. Wu, S. Wang, J. Shi, Q. Zhang, B. Zhao, Q. Wang, C. Zhu, Z. Liu, Y. Zheng, J. Su, Y. Gao, *Nano Energy* **2022**, *93*, 106896.
[195] Y. Du, B. Zhang, W. Zhou, R. Kang, W. Zhang, H. Jin, J. Wan, J. Qin, J. Zhang, G. Chen, *Energy Storage Mater.* **2022**, *51*, 29.
[196] W. Li, Y. Ma, P. Li, X. Jing, K. Jiang, D. Wang, *Adv. Energy Mater.* **2021**, *11*, 2102607.
[197] Y. Du, B. Zhang, R. Kang, W. Zhou, J. Qin, J. Wan, J. Zhang, G. Chen, *J. Mater. Chem. A* **2022**, *10*, 16976.
[198] L. Yan, X. Zeng, Z. Li, X. Meng, D. Wei, T. Liu, M. Ling, Z. Lin, C. Liang, *Mater. Today Energy* **2019**, *13*, 323.
[199] Y. Liu, M. Huang, F. Xiong, J. Zhu, Q. An, *Chem. Eng. J.* **2022**, *428*, 131092.
[200] N. Liu, X. Wu, Y. Zhang, Y. Yin, C. Sun, Y. Mao, L. Fan, N. Zhang, *Adv. Sci.* **2020**, *7*, 2000146.
[201] Z. Xu, M. Li, W. Sun, T. Tang, J. Lu, X. Wang, *Adv. Mater.* **2022**, *34*, 2200077.
[202] Y. Yao, Z. Chen, R. Yu, Q. Chen, J. Zhu, X. Hong, L. Zhou, J. Wu, L. Mai, *ACS Appl. Mater. Interfaces* **2020**, *12*, 40648.
[203] Y. Zhu, X. Ji, S. Cheng, Z. Chern, J. Jia, L. Yang, H. Luo, J. Yu, X. Peng, J. Wang, W. Zhou, M. Liu, *ACS Nano* **2019**, *13*, 9091.
[204] W. Kaveevivitchai, A. Manthiram, *J. Mater. Chem. A* **2016**, *4*, 18737.
[205] M. S. Chae, J. W. Heo, S. C. Lim, S. T. Hong, *Inorg. Chem.* **2016**, *55*, 3294.
[206] L. Hamenu, A. Madzvamuse, L. Mohammed, M. Hu, J. Park, M.-H. Ryou, Y. M. Lee, J. M. Ko, *Synth. Met.* **2017**, *231*, 25.
[207] W. Zhang, T. Sun, W. Hao, M. Cheng, Z. Zha, M. Shi, Z. Tao, *Energy Storage Mater.* **2024**, *70*, 103561.
[208] M. Karlsmo, R. Bouchal, P. Johansson, *Angew. Chem., Int. Ed.* **2021**, *60*, 24709.
[209] a) Y. Yuan, J. Yang, Z. Liu, R. Tan, M. Chuai, J. Sun, Y. Xu, X. Zheng, M. Wang, T. Ahmad, N. Chen, Z. Zhu, K. Li, W. Chen, *Adv. Energy Mater.* **2022**, *12*, 2103705; b) K. Yu, Y. Wen, M. Yan, X. Teng, W. Yang, S. Lian, J. Zhang, F. Zhang, X. Jiang, Y. Luo, L. Mai, *Mater. Today Energy* **2024**, *40*, 101488; c) L. Yang, Y. Zhu, H. Yu, Z. Wang, L. Cheng, D. Li, J. Tao, G. He, H. Li, *Adv. Energy Mater.* **2024**, *14*, 2401858.
[210] a) P. Cao, H. Zhou, X. Zhou, Q. Du, J. Tang, J. Yang, *ACS Sustainable Chem. Eng.* **2022**, *10*, 8350; b) J. Fu, H. Wang, P. Xiao, C. Zeng, Q. Sun, H. Li, *Energy Storage Mater.* **2022**, *48*, 191.
[211] a) W. Zhou, M. Chen, Q. Tian, J. Chen, X. Xu, C.-P. Wong, *Energy Storage Mater.* **2022**, *44*, 57; b) X. Zhang, S. Yang, Z. Huang, Z. Zeng, Y. Zhang, Z. Wang, *Electrochim. Acta* **2022**, *430*, 141081; c) W. Zhang, W. Jian, J. Yin, X. Zhang, C. Wang, X. Lin, Y. Qin, K. Lu, H. Lin, T. Wang, X. Qiu, *J. Cleaner Prod.* **2021**, *327*, 129522.
[212] L. Li, J. Peng, X. Jia, X. Zhu, B. Meng, K. Yang, D. Chu, N. Yang, J. Yu, *Electrochim. Acta* **2022**, *430*, 141129.
[213] Z. Zheng, S. Guo, M. Yan, Y. Luo, F. Cao, *Adv. Mater.* **2023**, *35*, 2304667.
[214] J. Cao, D. Zhang, C. Gu, X. Zhang, M. Okhawilai, S. Wang, J. Han, J. Qin, Y. Huang, *Nano Energy* **2021**, *89*, 106322.
[215] a) G. Guo, X. Tan, K. Wang, L. Zheng, H. Zhang, *J. Power Sources* **2023**, *553*, 232321; b) Z. Hou, Y. Gao, H. Tan, B. Zhang, *Nat. Commun.* **2021**, *12*, 3083; c) Y. Yang, T. Chen, B. Yu, M. Zhu, F. Meng, W. Shi, M. Zhang, Z. Qi, K. Zeng, J. Xue, *Chem. Eng. J.* **2022**, *433*, 134077.
[216] Y. Fang, X. Xie, B. Zhang, Y. Chai, B. Lu, M. Liu, J. Zhou, S. Liang, *Adv. Funct. Mater.* **2022**, *32*, 2109671.
[217] Z. Shao, S. Cheng, Y. Zhang, H. Guo, X. Cui, Z. Sun, Y. Liu, Y. Wu, P. Cui, J. Fu, Q. Su, E. Xie, *ACS Appl. Mater. Interfaces* **2021**, *13*, 34349.
[218] B. Lee, S. Cui, X. Xing, H. Liu, X. Yue, V. Petrova, H. Lim, R. Chen, P. Liu, *ACS Appl. Mater. Interfaces* **2018**, *10*, 38928.
[219] H. Cheng, J. Wang, C. Wu, Z. Liu, *Energy Mater. Adv.* **2023**, *4*, 0067.
[220] B. Wu, Y. Wu, Z. Lu, J. Zhang, N. Han, Y. Wang, X. Li, M. Lin, L. Zeng, *J. Mater. Chem. A* **2021**, *9*, 4734.
[221] D. Yuan, W. Manalastas Jr, L. Zhang, J. J. Chan, S. Meng, Y. Chen, M. Srinivasan, *ChemSusChem* **2019**, *12*, 4889.
[222] R. Xue, Z. Wang, N. Yao, Y. Liu, H. Wang, M. Zhang, A. Shao, X. Tang, J. Liu, J. Tang, Z. Wang, Y. Ma, *Adv. Funct. Mater.* **2024**, *34*, 2400959.
[223] J. Zhu, Z. Bie, X. Cai, Z. Jiao, Z. Wang, J. Tao, W. Song, H. J. Fan, *Adv. Mater.* **2022**, *34*, 2207209.
[224] Z. Xu, Z. Zhang, X. Li, Q. Dong, Y. Qian, Z. Hou, *ACS Appl. Mater. Interfaces* **2023**, *15*, 15574.
[225] Z. Sun, F. Bu, Y. Zhang, W. Zhou, X. Li, X. Liu, H. Jin, S. Ding, T. Zhang, L. Wang, H. Li, W. Li, C. Zhang, D. Zhao, Y. Wang, D. Chao, *Angew. Chem., Int. Ed.* **2024**, *63*, 202402987.

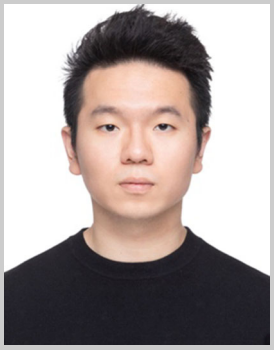

Mingcong Tang received his B.S. degree (2020) from University of California, San Diego, and M.S. degree (2022) from University of Michigan, Ann Arbor. He is currently pursuing his Ph.D. degree at the Hong Kong Polytechnic University under the supervision of Dr. Liang An. His current research is focusing on aqueous Zinc metal-based batteries.

Qun Liu is currently a researcher at the Inner Mongolia University. He received his Bachelor's, Master's and Ph.D. degrees from Dalian University of Technology, Xiamen University and the Hong Kong Polytechnic University, in 2016, 2019, and 2024, respectively. His current research focuses on the investigation of multifunctional polymers for Zn-ion batteries.

Xiaohong Zou received her Ph.D. at Nanjing Tech University in 2022. Now she is a post-doctoral in the Hong Kong Polytechnic University (PolyU). Her main research interests are energy storage and conversion device, especially for Li-O_2 batteries, Zn-air batteries, and solid-state batteries.

Biao Zhang joined the Hong Kong Polytechnic University in 2017. He is now an associate professor in the Department of Applied Physics. His recent work centers on building and probing robust electrode/electrolyte interfaces for rechargeable metal-ion batteries.

Liang An received his B.S. degree from Harbin Institute of Technology in 2008 and Ph.D. degree from The Hong Kong University of Science and Technology in 2012. He is currently an associate professor of Mechanical Engineering at The Hong Kong Polytechnic University. His research interests include advanced energy conversion and storage technologies, such as fuel cells and batteries.